Title
Quantitative Neurologic and Oncologic Positron Emission Tomography: Overcoming Practical and Structural Barriers

Author
Wilks, Moses Quinn

Publication Date
2014

UNIVERSITY OF CALIFORNIA

Los Angeles

Quantitative Neurologic and Oncologic Positron Emission Tomography: Overcoming Practical and Structural Barriers

A dissertation submitted in partial satisfaction of the
requirements for the degree of Doctor of Philosophy
in Biomathematics

by

Moses Quinn Wilks

2014

ABSTRACT OF THE DISSERTATION

Quantitative Neurologic and Oncologic Positron Emission Tomography: Overcoming Practical and Structural Barriers

by

Moses Quinn Wilks
Doctor of Philosophy in Biomathematics
University of California, Los Angeles, 2014
Professor Henry Huang, Chair

Positron Emission Tomography (PET) is an inherently quantitative tool for measuring *in vivo* biological phenomena. However, there are still many barriers, both practical and structural, to robust quantification of data in clinical and pre-clinical settings.

First, I present methods for improving quantification of neurologic PET in Alzheimer's disease imaging. Due to the variability in patient anatomy and disease state, it is difficult to accurately compare homologous anatomy between subjects. Here we examine methods of image normalization and automatic image analysis that allow for greatly reduced variance in data measurement. We show that through these methods, both the diagnostic and prognostic utility of the data can be greatly improved.

Additionally, we address the structural barriers to quantification in oncologic PET in radio-labeled custom antibodies. These large, high-affinity tracers have been shown, both *in silico* and *in vivo*, to display high degrees of heterogeneous binding in target tissues. Due to this phenomenon, classical ODE models of tracer kinetics are no longer valid. We develop and test a new set of non-linear PDE models to accurately represent tracer activity *in vivo*. We show that the use of classical ODE models will result in high levels of parameter estimate bias, and the new PDE models can accurately fit both *in silico* and *in vivo* data with the inclusion of Bayesian priors.

The dissertation of Moses Quinn Wilks is approved.

Jorge R. Barrio

Elliot M. Landaw

Kenneth Lange

Anna M. Wu

Henry Huang, Committee Chair

University of California, Los Angeles

2014

To my friends and family,
whose love and support was vital to my studies,
and to Wendy, without whom none of this would have been possible.

Table of Contents

List of Figures

List of Tables

Acknowledgments

Chapter 2 is reproduced from the article "Automated VOI Analysis in FDDNP PET Using Structural Warping: Validation Through Classification of Alzheimer's Disease Patients," co-authored with Hillary Protas, Mirwais Wardak, Vladimir Kepe, Gary W. Small, Jorge R. Barrio, and Sung-Cheng Huang. This work was published in the *International Journal of Alzheimer's Disease* (http://dx.doi.org/10.1155/2012/512069), and is reprinted through the Creative Commons Attribution License.

Chapter 3 is reproduced from a manuscript prepared for submission, co-authored with Mirwais Wardak, Vladimir Kepe, Jorge R. Barrio, Prabha Siddarth, and Sung-Cheng Huang.

Chapter 4 is reproduced from the article "Improved modeling of in vivo kinetics of slowly diffusing radiotracers for tumor imaging," co-authored with Scott M. Knowles, Anna M. Wu, and Sung-Cheng Huang. At the time of filing of this dissertation, the article is in press in the *Journal of Nuclear Medicine*, and is reprinted under the copyright agreement signed with the *Journal of Nuclear Medicine.*

Figure 1.2 is adapted with the permission of Springer from:

> Braak H, Braak E. Neuropathological stageing of Alzheimer-related changes. *Acta Neuropathologica.* 1991;82(4):239-259.

Figure 1.3 is reproduced with the permission of Wolters Kluwer Health from:

> Thompson PM, MacDonald D, Mega MS, Holmes CJ, Evans AC, Toga AW. Detection and mapping of abnormal brain structure with a probabilistic atlas of cortical surfaces. *Journal of Computer Assisted Tomography.* 1997;21(4):567-581

Figure 1.4 is adapted with the permission of the American Society of Clinical Oncology from:

> Knowles SM, Wu AM. Advances in Immuno–Positron Emission Tomography: Antibodies for Molecular Imaging in Oncology. *Journal of Clinical Oncology.* 2012;30(31):3884-3892.

Figure 1.5 is adapted with the permission of Springer from:

> Jones PL, Gallagher BM, Sands H. Autoradiographic analysis of monoclonal antibody distribution in human colon and breast tumor xenografts. *Cancer Immunology, Immunotherapy.* 1986;22(2):139-143.

Figure 1.6 is reproduced with the permission of Elsevier from:

> Thurber GM, Schmidt MM, Wittrup KD. Factors determining antibody distribution in tumors. *Trends in pharmacological sciences.* 2008;29(2):57-61.

Figures 2.3 and 3.1, are adapted with permission of Elsevier from:

> Protas HD, Huang S-C, Kepe V, *et al*. FDDNP binding using MR derived cortical surface maps. NeuroImage 2010;49:240-8.

The work in this dissertation was supported by the following sources: T32-GM008185, P01-AG025831, M01-RR00865, CA092131, CA016042, CA086306, and EB001943 from the National Institutes of Health; DE-FC03-87-ER60615 From the Department of Energy; The General Clinical Research Centers Program; the Elizabeth and Thomas Plott Endowment in Gerontology; and GM008042 from the UCLA Caltech Medical Scientist Training Program.

I would also like to acknowledge my doctoral committee (Dr. Henry (Sung-Cheng) Huang, Dr. Jorge R. Barrio, Dr. Elliot M. Landaw, Dr. Kenneth Lange, and Dr. Anna M. Wu), with their assistance and guidance, with special thanks to my advisor and committee chair Dr. Henry Huang. I also acknowledge all the members of Huang lab, especially Dr. K.P. Wong, Dr. Hillary

Protas, and Dr. Mirwais Wardak for their assistance in the work presented here. I also want to thank Dr. Scott M. Knowles for assistance in small animal imaging, Dr. Nagichettiar Satyamurthy and the UCLA Cyclotron Facility for synthesis of FDDNP, and Dr. David Stout at the Crump Small Animal Imaging Facility.

VITA

2004	Undergraduate Researcher, Owens Lab, Department of Plant Biology, Cornell University.
2005-2007	Undergraduate Intern, Gene Network Sciences, Ithaca, NY.
2006-2007	Undergraduate Researcher, Gilmour Lab, College of Veterinary Medicine, Cornell University.
2007	B.A. (Mathematics), and B.A. (Biology), Cornell University
2007-2009	NIH Systems & Integrative Biology Training Grant, UCLA.
2009	M.S. (Biomathematics), UCLA
2009-2014	Graduate Student Researcher, Huang Lab, Department of Biomathematics, UCLA.
2013	Society of Nuclear Medicine Computer and Instrumentation Young Investigator Award.

PUBLICATIONS AND PRESENTATIONS

Hirata K, Wong KP, Sha W, Ye H, Iwamoto H, **Wilks MQ**, Stout D, McBride W, Tamaki N, and Huang S-C. "A new partial volume correction method for dynamic FDG images of heterogeneous tumor using factor analysis and stepwise procedure." *J Nucl Med Meeting Abstracts.* May 1, 2014; 55 (1: Meeting Abstracts):2068.

Nathanson DA, Armijo AL, Tim M, Li Z, Dimitrova E, Austin WR, Nomme J, Campbell DO, Ta L, Le TM, Lee JT, Darvish R, Gordin A, Wei L, Liao H-I, **Wilks MQ**, Martin C, Sadeghi S, Murphy JM, Boulos N, Phelps ME, Faull KF, Herschman HR, Jung ME, Czernin J, Lavie A, and Radu CG. "Co-targeting of convergent nucleotide biosynthetic pathways for leukemia eradication." *Journal of Experimental Medicine*, 211:3 (2014), 473-486.

Sha W, Ye H, Iwamoto KS, Wong KP, **Wilks MQ**, Stout D, McBride W, and Huang S-C. “Factors affecting tumor ^{18}F-FDG uptake in longitudinal mouse PET studies." *EJNMMI research* 3:51 (2013): 1-11.

Wilks MQ, Knowles SM, Wu AM, and Huang S-C. " Improved modeling of in vivo kinetics of slowly diffusing radiotracers for tumor imaging " *Journal of Nuclear Medicine*, 2014 in press.

Wilks MQ, Knowles SM, Wu AM, and Huang S-C. "Quantitative in vivo imaging of slowly diffusing radiotracers". *J Nucl Med Meeting Abstracts.* May 1,2013;54(2: Meeting Abstracts):48.

Wilks MQ, Gary W. Small, Jorge R. Barrio, and Sung-Cheng Huang. "Evaluation of the use of voxel-value distribution in target regions in longitudinal FDDNP PET studies." *J Nucl Med Meeting Abstracts.* May 1, 2013;54(2: Meeting Abstracts):2066

Wilks MQ, Protas H, Wardak M, Kepe V, Small GW, Barrio JR, and Huang S-C. “Automated VOI analysis in FDDNP PET using structural warping: validation through classification of Alzheimer's disease patients,” *International Journal of Alzheimer's Disease*, vol. 2012, Article ID 512069, 8 pages, 2012. doi:10.1155/2012/512069

Wilks MQ, Knowles SM, Wu AM, and Huang S-C. “Accurate quantitative imaging of slowly diffusing radiotracers." *J Nucl Med Meeting Abstracts.*May 1,2012;53(1:Meeting Abstracts):549.

Wilks MQ, Siddarth P, Ercoli L, Kepe V, Small GW, Barrio JR, and Huang S-C. "Longitudinal study of changes in FDDNP-PET and neuropsychological scores." *J Nucl Med Meeting Abstracts.* May 1, 2011; 52(1: Meeting Abstracts):1266.

Wilks MQ, Protas H, Wardak M, Small GW, Barrio JR, and Huang S-C. "Automated VOI analysis in 18 F-FDDNP PET using structural warping: Validation through classification of Alzheimer's disease patients." Paper presented at: Nuclear Science Symposium Conference Record (NSS/MIC), 2010 IEEE, 2010.

Williams KJ, Argus JP, Zhu Y, **Wilks MQ**, Marbois BN, York AG, Kidani Y, Pourzia AL, Akhavan D, Lisiero DN, Komisopoulou E, Henkin AH, Soto H, Chamberlain BT, Vergnes L, Jung ME, Torres JZ, Liau LM, Christofk HR, Prins RM, Mischel PS, Reue K, Graeber TG, and Bensinger SJ. “An essential requirement for the SCAP/SREBP signaling axis to protect cancer cells from lipotoxicity.” *Cancer research*, 73:9 (2013), 2850-2862.

CHAPTER 1 - Introduction and Motivations

Abstract

Positron Emission Tomography (PET) is an inherently quantitative tool for measuring *in vivo* biological phenomena. The physics behind positron annihilation and coincidence detection lead to mathematical and statistical image reconstruction methods that allow for very accurate *in vivo* measurements of tracer concentration. These measurements allow investigators to quantitatively assay a myriad of biological parameters and phenomena, such as antigen concentrations, cell division rates, or glucose utilization rates. However, there are still many barriers to robust quantification of data in clinical and pre-clinical settings. These barriers can largely be divided into two main categories: practical and structural. Practical barriers are largely functions of inter- or intra-investigator variability in data extraction or analysis, or an investigator's inability to robustly analyze data in a feasible amount of time. Structural barriers are those that are inherent to the PET imaging modality, such as photon scatter or partial volume effects. In this work, solutions are presented and tested to overcome some of the practical barriers to quantification in neurologic applications, and to overcome structural barriers in oncologic applications.

1.1.0 Practical Barriers to Quantification

In quantitative imaging, the creation of accurate volumes of interest (VOIs) is often of utmost importance. In most scenarios, VOIs are drawn manually by expertly trained investigators, which can be a very time-consuming and tedious process. Additionally, hand-drawing VOIs is known to introduce measurement variance on both inter- and intra-investigator levels. A further problem with manually defined VOIs, is that to extract data from a subject population in a timely fashion, investigators are usually limited to defining relatively small VOIs on only a single slice of an image. This opens many possibilities for the introduction of noise in data measurement, either through the small sampling size, or through sampling bias where the investigator is looking for regions with either high or low levels of activity. These problems are further inflated in large-population studies, and even more so in multi-center studies.

In addition to increasing noise in data measurement, manual definition of VOIs can introduce noise in data analysis as well. In many quantitative imaging applications, some form of graphical image analysis will be employed to estimate biologically important parameters, such as Logan analysis to determine distribution volume ratios (DVR) or Patlak analysis to determine the influx rate constant K_i of the tracer [1,2]. In both these scenarios, the activity within both the target region and a reference region is necessary. However, manual definition of a reference region is subjected to the same constraints discussed above.

Manually defining VOIs can introduce small amounts of noise to oncologic applications, where small differences in VOI boundaries can lead to measurement differences caused either by partial volume effects or by tissue heterogeneity due to necrosis. However, the noise introduced from manually defined VOIs is much greater in neurologic applications. This is due to the increased difficulty in defining structural boundaries, and to matching homologous structures between multiple subjects. This problem is further complicated by the fact that in many applications of neurological imaging, the disease or disorder being investigated presents with structural pathologies, such as cortical degeneration, making the comparison of homologous structure more difficult, or even impossible, through manual measurements.

These limitations to PET quantification are exemplified by Alzheimer's disease (AD) imaging, where DVR images are often employed to examine pathology densities in specific anatomical locations, with differing levels of neuro-degeneration seen across subject populations. As can be seen in Figure 1.1, manual definitions of homologous structures between multiple AD subjects will be extremely difficult. In Chapters 2&3 of this work, we examine methods for overcoming these barriers to quantification in AD.

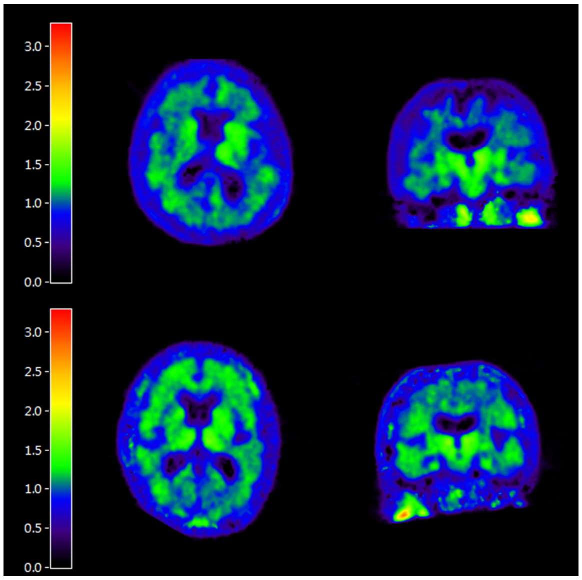

FIGURE 1.1: FDDNP-DVR PET images from two AD subjects.

1.1.1 Alzheimer's Disease

Alzheimer's disease is the most common form of dementia, and is characterized by gradual progression of clinical symptoms and neurological pathologies, including misfolded protein aggregates and cortical degeneration [3,4]. Although AD is clinically recognizable at late stages due to characteristic dementia and decline in cognitive abilities, current clinical diagnosis standards do not yet produce definitive differentiation between AD and non-Alzheimer’s dementias (*e.g.*, frontotemporal dementia) [5,6]. Additionally, previous work has shown that there can be large numbers of false-negatives in AD diagnosis, with cognitive decline being attributed to normal senescence [7,8]. Further complications in diagnosis stem from the occurrence of intermediate conditions, such as mild cognitive impairment (MCI). Patients classified as MCI display greater cognitive decline, especially in measures of memory, than would be expected through healthy aging alone, but do not show any clinical signs of dementia [9]. While MCI patients do not always progress to a demented state, they do show a greatly increased risk for developing dementias (including AD), over the non-MCI population [10]. As a result of these complications, the current gold-standard for AD diagnosis remains *post-mortem* inspection of cortical tissue, with histopathological staining for the hallmark pathologies of AD: β-amyloid plaques and neurofibrillary tangles (NFTs). It has long been known that in AD, the progression of these misfolded protein aggregates follows a well defined spatial pattern, originally described by Braak and Braak [11].

Braak and Braak proposed three stages (A-C) for the deposition of β-amyloid, and six stages (I-VI) for the pattern of deposition of NFTs. The β-amyloid plaques begin to accumulate in the basal temporal isocortex (stage A) and as the disease progresses, plaques spread to the frontal lobe and the cortical association regions of the occipital and parietal lobes (stage B). In the final stages, plaque is present throughout all isocortical regions (stage C). The accumulation of NFTs follows its own pattern: first accumulating in the entorhinal cortex (stages I/II) and then over spreading through the limbic areas (stages III/IV), to finally cover almost all of isocortex (stages V/VI), leaving only the primary motor strip relatively unscathed (Fig 1.2).

While there are no robust mappings between the pathological stages described by Braak and Braak and specific clinical symptoms, current evidence does show that the accumulation of these neuropathological markers begins long before the onset of clinically recognizable symptoms, occurring in both healthy controls and MCI subjects [12]. *Post-mortem* examinations have revealed that cognitively normal controls can have similar distributions of β-amyloid plaques and NFTs in mildly demented patients, with NFT progression spanning Braak stages 0-V [13,14]. Although this shows that AD pathology can predate clinical symptoms, these studies also show that once clinical symptoms are present, they do correlate with Braak defined NFT stages. A majority of MCI patients examined (80%) displayed NFT density and distribution consistent with Braak stages II-IV, and almost all AD patients examined (91%) displayed pathologies consistent with stages IV-VI [14].

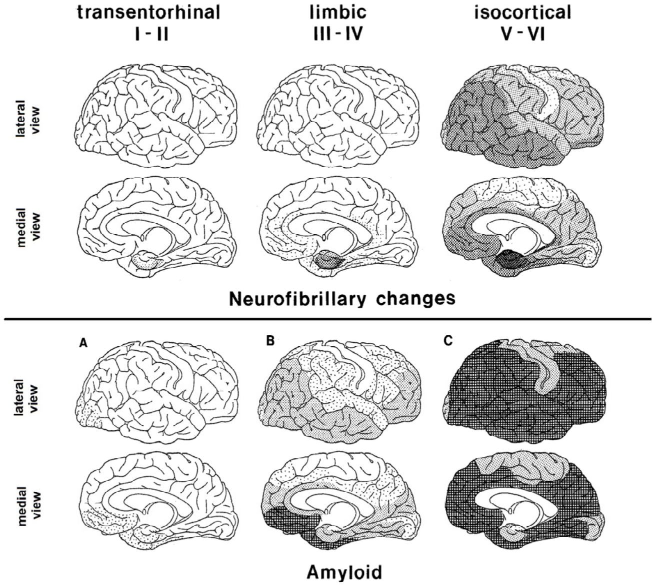

FIGURE 1.2. Proposed pathological progression of amyloid plaques and NFTs in AD. Adapted from Braak and Braak [11].

1.1.2 Molecular Imaging of Alzheimer's Disease

As discussed above, AD and its precursor conditions, such as MCI, are difficult to diagnose through clinical examination alone. Because AD is well defined by spatial progression of pathology, which appears to correlate to clinical disease state, AD is an ideal candidate for diagnosis and staging through non-invasive molecular imaging. If Alzheimer's pathologies can be accurately measured through molecular imaging, not only would it be possible to supplant the current gold standard of *post-mortem* examination for diagnosis, it would also be possible to non-invasively stage disease state, possibly detecting it before clinical symptoms present.

Several families of positron-emitting tracers are currently at various stages of development, for imaging either or both of the AD pathologies. The first attempt at amyloid imaging employed ^{99}Tc-labeled Fab fragments specific to β-amyloid proteins for SPECT imaging, however these antibodies were unable to penetrate the blood-brain barrier, leading to the development of smaller tracer compounds [12]. One of the first such compounds was the thioflavin T derivative ^{11}C-6-OH-BTA-1 (^{11}C-PIB), which was shown to have *in vitro* affinity to β-amyloid complexes. In initial investigations, and in subsequent independent studies, investigators found strong delineations between mean cortical binding rates of controls and AD. However, there were often significant outliers, showing some AD subjects with extremely low levels of ^{11}C-PIB activity, and some controls with AD levels of activity [15-17]. Also, ^{11}C has a half-life of only 20 minutes, too short to be used by centers without on-site cyclotrons. This led to the development of similar ^{18}F-labeled amyloid imaging agents such as Florbetapir (AV-45) and Florbetaben (BAY 94-9172) [18,19]. These compounds showed similar results to ^{11}C-PIB, with some group discrimination, but with many group outliers [20].

These compounds also exhibit several shortcomings in quantitative AD imaging. First, although control subjects do usually exhibit lower cortical binding rates with these compounds, they also exhibit strong white-matter activity uncharacteristic of amyloid deposition *in vivo* [12]. Furthermore, these compounds usually exhibit a binary response in subjects, with "controls" showing little to no cortical activity and high white-matter activity, and "AD" subjects showing high global cortical uptake of tracer. This leads many investigators to use global averages of tracer activity to classify subjects with their imaging protocols [21,22]. While this "on/off" phenomena makes visual classification of images relatively simple (though not very accurate), it is complicated by the fact that it is not in line with the known gradual progression of amyloid pathology seen in *post-mortem* examinations, and as described by Braak and Braak. This disagreement between imaging and *in vivo* pathology could explain the difficulty seen in measuring longitudinal changes in binding of these amyloid-binding tracers [23]. Lastly, these compounds do not show binding to the NFTs that are characteristic of Alzheimer's disease, limiting their ability to stage the progression of disease *in vivo*. Recently, new radio-labeled tracers have been developed for imaging of only the NFTs associated with AD [24]. While these compounds have shown initial promise *in vitro*, much future work is required to verify their utility for *in vivo* clinical imaging.

Some of the limitations of these single-target tracers can be overcome through the use another imaging agent, 2-(1-6-[(2-[^{18}F]fluoroethyl)(methyl)amino]-2-naphthylethylidene)malononitrile (FDDNP), which was the first PET imaging agent developed for visualization of both amyloid plaques and NFTs [25-27]. In addition to binding to both AD pathologies, FDDNP has shown *in vivo* distributions in line with the Braak and Braak progression, without white matter uptake in controls [12]. Initial studies showed that AD subjects displayed significantly higher residence times of FDDNP in the medial temporal lobe, an area closely associated with early disease progression, and that these residence times closely correlated with mini-mental state examination (MMSE) scores [27]. Recent work has also shown that regional FDDNP DVR values can be used to accurately discriminate between controls, MCIs, and ADs, with binding patterns resembling Braak pathologies [28]. While there have been some longitudinal studies showing limited results in predictive capacity of FDDNP in AD, it is possible that the limitation is because global, instead of regional, activity was used as a predictor [23]. In Chapters 2&3, we use ^{18}F-FDDNP as an imaging agent for quantitative AD PET to show the enhanced value of using the improved quantitative methodologies developed in this dissertation.

1.1.3 Image Normalization

As discussed above, a major barrier to accurate quantification of PET imaging across multiple subjects is the creation of accurate VOIs. Consequently, there have been many previous efforts to minimize investigator induced variance through automatic generation of VOIs. These methods often work by normalizing each of the functional images (e.g. PET) to a common structural image (e.g. MRI), where a single set of anatomically based VOIs can be created and used for different subject's scans.

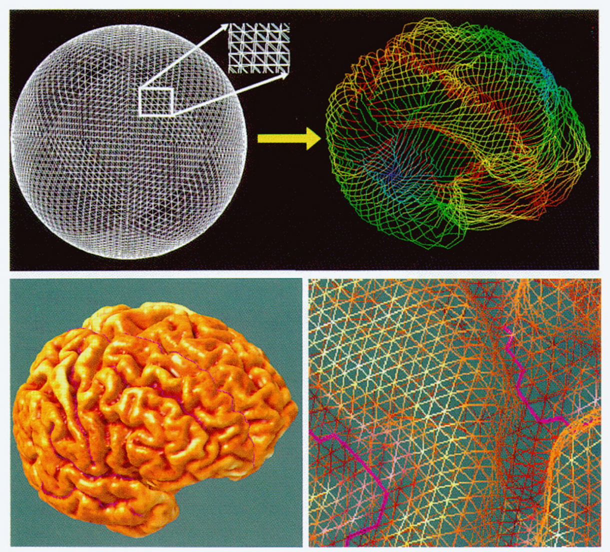

Figure 1.3: First Steps of Cortical Surface Mapping. A spherical mesh grid is progressively deformed to match a target boundry intensity in the 3D-MRI (Top). The resulting 3D cortical surface (Bottom Left) is high-resolution mesh of triangular elements (Bottom Right). Adapted from Thompson *et al.* [29].

One such method that has previously been shown to be effective in normalizing PET images is the process of hemispheric cortical surface mapping (CSM) [28,29]. In this process, a high resolution 3D map of a subject's cortex is extracted from a T1-wieghted MRI, by "shrink-wrapping" a fine mesh grid over the surface of MRI (Fig 1.3). The 3D surface is then "unfolded" to create a 2D cortical surface map of sulci and gyri. Investigators then manually define 36 specific major sulci and fissures (central, lateral, intraparietal, etc.), as a definition of each subject's topography. These sulcal maps are then fluidly deformed to match a common space image for which CSM has already been completed, in this case the International Consortium for Brain Mapping common space (ICBM53) [30]. In this method, regions of interest can be drawn directly on the 2D cortical surface map, defining specific cortical regions bounded by sulci, and then projected to the desired depth into tissue to create VOIs. Although this method has been successful in matching homologous structure, the process is complex and labor intensive, limiting its utility in large-scale studies.

Another probabilistic mapping method is the DARTEL algorithm as implemented in SPM8, which performs two simultaneous 3D deformations (one for a subject's gray matter and one for white matter) to a common-space average brain under maximum likelihood constraints [31]. Although this method significantly simplifies the image normalization process, it requires high accuracy T1-weighted MRI scans to be completed, so that accurate segmentation of white and gray matter can be accomplished. One other significant drawback of using CSM or DARTEL, is that they match images to an average brain atlas, in which it can be difficult to define anatomically specific VOIs. Additionally, in such atlases, significant anatomical structures can be blurred due to population variance, causing errors in image matching algorithms.

As an alternative to the probabilistic methods discussed above, one can instead use deformation algorithms that compute a single 3D mapping between two individual images, one of which can be a common-space atlas. The most computationally simple of these image matching use a set of smooth basis functions to define image deformations, such as the SPM2 algorithm which uses the discrete cosine transform (DCT) to parameterize the deformation [32]. To allow for reasonable computational time, the basis functions are limited to only low-frequency DCT, limiting matching accuracy when higher-frequency deformations are needed. A more versatile approach is through the use of constrained fluid deformation models, using various forms of image matching metrics and penalties, some of which include "landmark" conditions which force two anatomical features to map to one another [33-35].

Recently, a large-scale comparison of such methods was performed by Klein *et al.,* where fourteen image normalization algorithms were compared in their ability to normalize 80 manually segmented MRI brain images [36]. This comparison did not include any landmark based algorithms, however they do have the significant drawback of requiring manually defined homologous points across wide populations, limiting their utility in large-scale quantitative investigations. A top performer across all normalization metrics tested by Klein *et al*. was the symmetric image normalization (SyN) algorithm, as developed by Avants *et al*., which differs from most algorithms in several important ways [33,37]. In the SyN algorithm, image deformation is reformulated as an attempt to find a diffeomorphic mapping between two spaces. This mapping is also reformulated to compute two sub-deformations, which by constraint are both diffeomorphic, to a theoretical "average" of the two input images. Additional constraints are imposed to ensure that the magnitudes of these sub-deformations are identical. These formulations lead to several desirable properties of the resulting 3D mapping. Firstly, these constraints ensure that SyN will report identical results regardless of which image is designated as the "target" space, and that the deformation is guaranteed to be invertible with sub-voxel accuracy everywhere. This differs from other fluid deformation methods in which inverses are estimated, and therefore mappings are not guaranteed to be truly invertible [37]. Because the

SyN algorithm returns a mapping that is guaranteed to be diffeomorphic, deformations never result in shearing or tearing, preserving the topology of each individual's brain.

For the reasons state above, we use the SyN algorithm to compute image matching between subjects and a common space in Chapters 2&3 of this work. To further eliminate investigator-induced variability, we use the CSM technique to robustly define cortical VOIs on the common space image. In Chapter 2, we test the reliability of these automated measurement techniques through diagnostic accuracy of disease state (AD, MCI, or healthy control). In Chapter 3, we apply this method to improving prognostic accuracy of disease progression over a two-year follow-up study of MCI patients and age-matched healthy controls.

1.2.0 Structural Barriers to Quantification

A common structural barrier to quantification in PET is the noise introduced through partial volume effects. Due to the image resolution inherent to PET scanners, there will be slight 3D blurring of measured data, resulting in spillover between adjacent regions. When tissue heterogeneity on the supra-voxel level occurs at high enough spatial frequency, this will lead to under-, or over-estimates of tissue activity along the borders of a region with otherwise homogeneous activity. A similar, but much less investigated, phenomena is errors induced by tracer heterogeneity on the *sub*-voxel level.

Most quantitative analysis of PET imaging is done through the use of kinetic, or quasi-kinetic, modeling of tracer activity, and is performed with ODE pharmacokinetic models or with a graphical technique such as Logan or Patlak analysis [1,2]. Inherent to these models, however, is the assumption that tracers are well-mixed, such that within any given voxel all molecules of the tracers within a single compartment (e.g. extracellular or intracellular space) are kinetically identical. This assumption leads to a system of ODEs that describe the biological kinetics, and are relatively simple to solve. However, these models cease to be valid as soon as there is sub-voxel heterogeneity. This problem arises with the use of new large-molecule tracers that display slow diffusion through tissue, resulting in spatial heterogeneity in the micrometer scale [38]. In Chapter 4 of this work, we examine the effects of ignoring this spatial heterogeneity in kinetic modeling, and methods to accurately compensate for it.

1.2.1 Large Molecule Tracers

Custom antibodies are a new and promising class of molecules that can be used for imaging or therapeutics [39-43]. These compounds allow for high-specificity binding to target tissues, with very little background activity, effectively allowing for *in vivo* immunohistochemical staining. A significant difference between custom antibodies and standard small-molecule tracers such as FDG are their much longer biological half-lives, which are on the order of days, instead of hours. Additionally, these large-molecule compounds show much slower capillary permeability, resulting in slower uptake into target tissues. As a result, these compounds must be labeled with slower decaying isotopes such as ^{89}Zr (half-life = 78.4 hours), or ^{124}I (half-life 100.2 hours) in order to fully capture the time course activity of the tracer within the subject.

The extreme half-lives of these compounds is a double-edged sword for quantitative imaging, as the long residence times allows for high levels of tracer to build up in target tissues. However, because clearance from the blood compartment is also slow, a long waiting period between tracer injection and scanning is required to achieve good signal to background ratios [39]. Recent work has been performed to compensate for these shortcomings by reducing the size of these tracers through the deletion of constant, non-binding domains of these antibodies. These engineered compounds can be a third of the weight (50kDa) of intact antibodies (150kDa), and show markedly different *in vivo* kinetics [39].

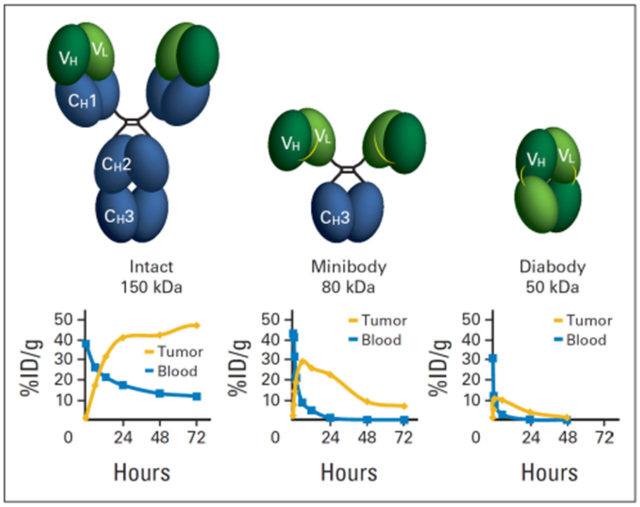

FIGURE 1.4. Effects of deletion of constant domains on clearance rates of custom antibodies. Adapted from Knowles and Wu [39].

As can be seen in Figure 1.4, the removal of constant domains leads to much faster clearance of tracer from the blood pool, which also results in lower levels of target-tissue labeling. While the diabody molecule shows extremely fast clearance, labeling of target-tissues is limited, likely due to the low capillary permeability. The minibody tracer however, shows strong labeling (30% ID/g), with a time course activity that can be completely examined over a reasonable time scale of a few days.

It has long been established that although antibody tracers show high target specificity, there is a divergence between their spatial localization *in vitro* and *in vivo.* As early as the 1980's, autoradiographic studies showed markedly different distributions of these molecules between *in vitro* incubation and *in vivo* injection, as can be seen in Figure 1.5 [38].

Early *in silico* studies explained this divergence, by showing that the slow diffusivity of these compounds *in vivo* would lead to steep concentration gradients of tracer on the sub-voxel level

[44]. This slower diffusivity is likely a result of their size (~150 kDa), as opposed to traditional small-molecule tracers (usually <1 kDa), which also explains their lower levels of capillary permeability [45].

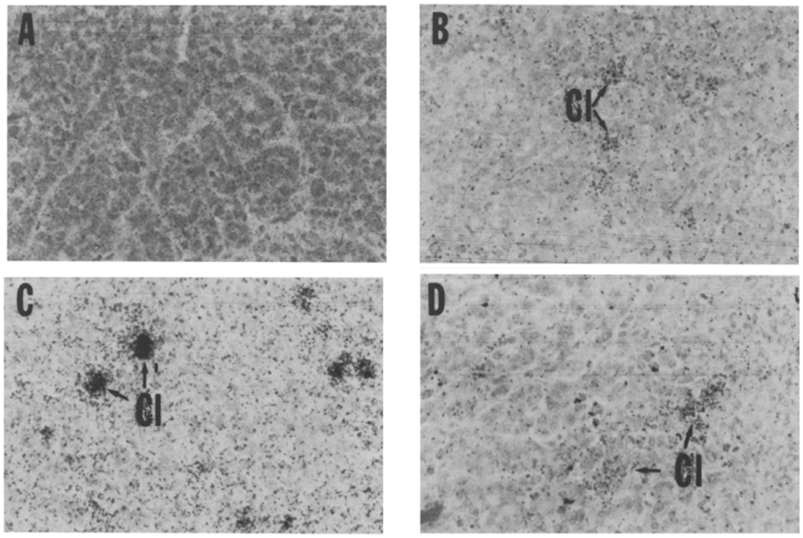

FIGURE 1.5. Divergence of *in vitro* and *in vivo* antibody localization. Images show autoradiography of ^{125}I-labeled antibody after *in vitro* incubation (A), and 4 (B), 24(C), or 120 (D) hours post-injection *in vivo* at 250x magnification. Adapted from Jones, Gallager, and Sands [38].

Compounding the effect of their size, is the high affinity to target tissue displayed by custom antibodies, which can range from low nanomolar to even picomolar values. This leads to further tissue heterogeneity, with tracers binding to target antigens very quickly, and leading to almost all of injected tracer localizing around the capillary wall [46-49]. This effect of binding affinity is so strong that heterogeneous localization is seen with even relatively small (25 kDa) single-chain variable fragments (scFvs), and the smaller doxorubicin (.5 kDa) [50,51]. More recent studies have shown the extent of this localization *in vivo* through imaging of *ex vivo* slices of xenograft tissue, as can be seen in Figure 1.6.

Despite these complications, custom antibodies show great promise for use in quantitative imaging. With few exceptions (like anti-HER2 probes), there will be little to no uptake in myocardial tissue, allowing for accurate measurements of image derived input functions from the left ventricle, and the high target specificity allows for high signal to noise ratios. Additionally, quantitative imaging of these compounds allows investigators to assay *in vivo* levels of protein expression, which can be an important biomarker. In the case of prostate stem cell antigen (PSCA), which is expressed in most local and metastasized prostate cancers, expression levels correlate to Gleason score, allowing for non-invasive imaging-based disease staging [54-56]. In order to extract this type of information, however, robust mathematical models that account for tissue heterogeneity are required.

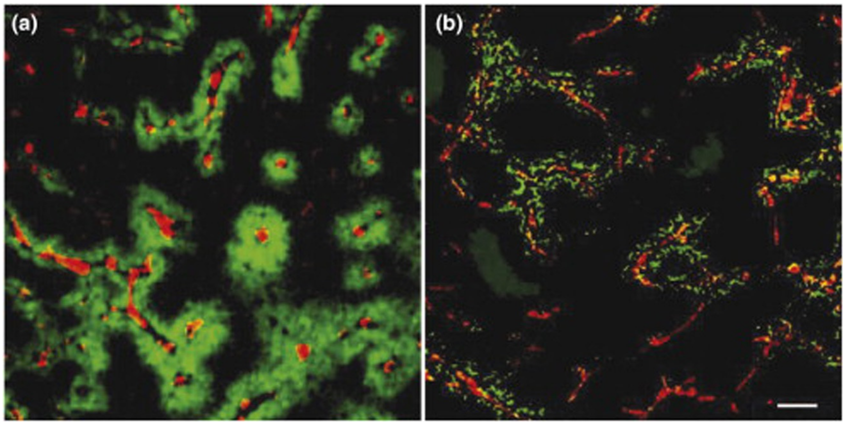

FIGURE 1.6. Heterogeneous localization of trastuzumab (a) and doxorubicin (b) in xenograft tissue. Capillaries are labeled red, drugs are labeled green (Scale bar =100um). Reproduced from Thurber et. al [52].

Previous work has been performed to investigate the effect that the tissue heterogeneity displayed by these large-molecule tracers will have on whole-tumor activity over time, although there has yet to be work published on the extraction of whole kinetic information from imaging such systems [48, 57]. To fully and accurately extract biologically important information from *in vivo* imaging of these systems, a physically accurate mathematical model must be developed to account for sub-voxel tissue heterogeneity. Furthermore, in therapeutic uses of these large molecule tracers, such as trastuzumab or doxorubicin, the doses given to tumors will be depth-dependant, with large volumes of the tumor far away from capillary walls receiving little or no treatment [52]. Therefore, in order to develop effective treatment protocols that allow for needed drug dosages across all depths of target tissue, the kinetics and diffusion of these drugs must be accurately understood. In Chapter 4 of this work, we examine the effects of slow diffusion on measured time activity curves of *in vivo* imaging with radio-labeled custom antibodies. Further, we show the effects of ignoring diffusion on estimating important biological parameters, and develop and test a method of extracting those parameters by taking spatial heterogeneity into account.

References

[1] Logan J, Fowler JS, Volkow ND, Wang G-J, Ding Y-S, Alexoff DL. Distribution volume ratios without blood sampling from graphical analysis of PET data. *Journal of Cerebral Blood Flow & Metabolism.* 1996;16(5):834-840.

[2] Patlak CS, Blasberg RG, Fenstermacher JD. Graphical evaluation of blood-to-brain transfer constants from multiple-time uptake data. *J Cereb Blood Flow Metab.* 1983;3(1):1-7.

[3] Ercoli LM, Small GW. Clinical Evaluation of Dementia and When to Perform PET. In: Silverman D, ed. *PET in the Evaluation of Alzheimer's Disease and Related Disorders*. New York: Springer; 2009.

[4] Double K, Halliday G, Krill J, *et al*. Topography of brain atrophy during normal aging and Alzheimer's disease. *Neurobiology of aging.* 1996;17(4):513-521.

[5] Varma AR, Snowden JS, Lloyd JJ, Talbot PR, Mann DMA, Neary D. Evaluation of the NINCDS-ADRDA criteria in the differentiation of Alzheimer's disease and frontotemporal dementia. *Journal of Neurology, Neurosurgery & Psychiatry.* 1999;66(2):184-188.

[6] Dubois B, Feldman HH, Jacova C, *et al*. Research criteria for the diagnosis of Alzheimer's disease: revising the NINCDS– ADRDA criteria. *The Lancet Neurology.* 2007;6(8):734-746.

[7] Hoffman RS. Diagnostic errors in the evaluation of behavioral disorders. *JAMA.* 1982;248(8):964-967.

[8] Ryan D. Misdiagnosis in dementia: comparisons of diagnostic error rate and range of hospital investigation according to medical speciality. *International journal of geriatric psychiatry.* 1994;9(2):141-147.

[9] Petersen RC. Mild cognitive impairment as a diagnostic entity. *Journal of Internal Medicine.* 2004;256(3):183-194.

[10] Gauthier S, Reisberg B, Zaudig M, *et al*. Mild cognitive impairment. *The Lancet.* 2006;367(9518):1262-1270.

[11] Braak H, Braak E. Neuropathological stageing of Alzheimer-related changes. *Acta Neuropathologica.* 1991;82(4):239-259.

[12] Kepe V, Huang S-C, Small GW, Satyamurthy N, Barrio JR. Microstructural Imaging of Neurodegenerative Changes. In: Silverman D, ed. *PET in the Evaluation of Alzheimer's Disease and Related Disorders*. New York: Springer; 2009.

[13] Price JL, Morris JC. Tangles and plaques in nondemented aging and "preclinical" Alzheimer's disease. *Annals of Neurology.* 1999;45(3):358-368.

[14] Petersen RC, Parisi JE, Dickson DW, *et al*. Neuropathologic features of amnestic mild c ognitive impairment. *Archives of Neurology.* 2006;63(5):665-672.

[15] Klunk WE, Engler H, Nordberg A, *et al*. Imaging brain amyloid in Alzheimer's disease with Pittsburgh Compound-B. *Annals of Neurology.* 2004;55(3):306-319.

[16] Mintun M, Larossa G, Sheline Y, *et al*. [11C] PIB in a nondemented population Potential antecedent marker of Alzheimer disease. *Neurology.* 2006;67(3):446-452.

[17] Jack Jr CR, Lowe VJ, Senjem ML, *et al*. 11C PiB and structural MRI provide complementary information in imaging of Alzheimer's disease and amnestic mild cognitive impairment. *Brain.* 2008;131(3):665-680.

[18] Rowe CC, Ackerman U, Browne W, *et al*. Imaging of amyloid β in Alzheimer's disease with ^{18}F-BAY94-9172, a novel PET tracer: proof of mechanism. *The Lancet Neurology.* 2008;7(2):129-135.

[19] Choi SR, Golding G, Zhuang Z, *et al*. Preclinical properties of 18F-AV-45: a PET agent for Aβ plaques in the brain. *Journal of Nuclear Medicine.* 2009;50(11):1887-1894.

[20] Villemagne VL, Ong K, Mulligan RS, *et al*. Amyloid imaging with 18F-florbetaben in Alzheimer disease and other dementias. *Journal of Nuclear Medicine.* 2011;52(8):1210-1217.

[21] Villain N, Chételat G, Grassiot B, *et al*. Regional dynamics of amyloid-β deposition in healthy elderly, mild cognitive impairment and Alzheimer's disease: a voxelwise PiB–PET longitudinal study. *Brain.* 2012;135(7):2126-2139.

[22] Landau SM, Mintun MA, Joshi AD, *et al*. Amyloid deposition, hypometabolism, and longitudinal cognitive decline. *Annals of Neurology.* 2012.

[23] Jack CR, Lowe VJ, Weigand SD, *et al*. Serial PIB and MRI in normal, mild cognitive impairment and Alzheimer's disease: implications for sequence of pathological events in Alzheimer's disease. *Brain.* 2009;132(5):1355-1365.

[24] Okamura N, Furumoto S, Harada R, *et al*. Novel 18F-labeled arylquinoline derivatives for noninvasive imaging of tau pathology in Alzheimer disease. *Journal of Nuclear Medicine.* 2013;54(8):1420-1427.

[25] Barrio J, Huang S, Cole G, *et al*. PET imaging of tangles and plaques in Alzheimer disease with a highly hydrophobic probe. *Journal of Labelled Compounds and Radiopharmaceuticals.* 1999;42:S194-S195.

[26] Agdeppa E, Kepe V, Shoghi-Jadid K, *et al*. In vivo and in vitro labeling of plaques and tangles in the brain of an Alzheimer's disease patient: A case study. Paper presented at: Journal of Nuclear Medicine, 2001.

[27] Shoghi-Jadid K, Small GW, Agdeppa ED, *et al*. Localization of neurofibrillary tangles and beta-amyloid plaques in the brains of living patients with Alzheimer disease. *The American journal of geriatric psychiatry.* 2002;10(1):24-35.

[28] Protas HD, Huang S-C, Kepe V, *et al*. FDDNP binding using MR derived cortical surface maps *NeuroImage.* 2010;49(1):240-248.

[29] Thompson PM, MacDonald D, Mega MS, Holmes CJ, Evans AC, Toga AW. Detection and mapping of abnormal brain structure with a probabilistic atlas of cortical surfaces. *Journal of Computer Assisted Tomography.* 1997;21(4):567-581.

[30] Mazziotta J, Toga A, Evans A, *et al*. A probabilistic atlas and reference system for the human brain: International Consortium for Brain Mapping (ICBM). *Philosophical Transactions of the Royal Society of London B Biological Sciences.* 2001;356(1412):1293-1322.

[31] Ashburner J. A fast diffeomorphic image registration algorithm. *Neuroimage.* 2007;38(1):95-113.

[32] J. Ashburner and K. J. Friston, "Nonlinear spatial normalization using basis functions," *Human Brain Mapping*, vol. 7, no. 4, pp. 254–266, 1999.

[33] Avants BB, Epstein CL, Grossman M, Gee JC. Symmetric diffeomorphic image registration with cross-correlation: Evaluating automated labeling of elderly and neurodegenerative brain. *Medical Image Analysis.* 2008;12(1):26-41.

[34] Vercauteren T, Pennec X, Perchant A, Ayache N. Diffeomorphic demons: Efficient non-parametric image registration. *Neuroimage.* 2009;45(1):S61-S72.

[35] Ardekani BA, Guckemus S, Bachman A, Hoptman MJ, Wojtaszek M, Nierenberg J. Quantitative comparison of algorithms for inter-subject registration of 3D volumetric brain MRI scans. *Journal of Neuroscience Methods.* March 15 2005;142(1):67-76.

[36] Klein A, Andersson J, Ardekani BA, *et al*. Evaluation of 14 nonlinear deformation algorithms applied to human brain MRI registration. *Neuroimage.* 2009;46(3):786-802.

[37] Christensen GE, Johnson HJ. Consistent image registration. *Medical Imaging, IEEE Transactions on.* 2001;20(7):568-582.

[38] Jones PL, Gallagher BM, Sands H. Autoradiographic analysis of monoclonal antibody distribution in human colon and breast tumor xenografts. *Cancer Immunology, Immunotherapy.* 1986;22(2):139-143.

[39] Knowles SM, Wu AM. Advances in Immuno–Positron Emission Tomography: Antibodies for Molecular Imaging in Oncology. *Journal of Clinical Oncology.* 2012;30(31):3884-3892.

[40] Larson SM, Pentlow KS, Volkow ND, *et al*. PET scanning of iodine-124-3F9 as an approach to tumor dosimetry during treatment planning for radioimmunotherapy in a child with neuroblastoma. *Journal of nuclear medicine: official publication, Society of Nuclear Medicine.* 1992;33(11):2020-2023.

[41] Mumprecht V, Honer M, Vigl B, *et al*. In vivo Imaging of Inflammation-and Tumor-Induced Lymph Node Lymphangiogenesis by Immuno–Positron Emission Tomography. *Cancer research.* 2010;70(21):8842-885

[42] Ambrosini V, Fani M, Fanti S, Forrer F, Maecke HR. Radiopeptide imaging and therapy in Europe. *Journal of Nuclear Medicine.* 2011;52(Supplement 2):42S-55S.

[43] Graham MM, Menda Y. Radiopeptide imaging and therapy in the United States. *Journal of Nuclear Medicine.* 2011;52(Supplement 2):56S-63S.

[44] Fujimori K, Covell DG, Fletcher JE, Weinstein JN. Modeling analysis of the global and microscopic distribution of immunoglobulin G, F (ab′) 2, and Fab in tumors. *Cancer research.* 1989;49(20):5656-5663.

[45] Dreher MR, Liu W, Michelich CR, Dewhirst MW, Yuan F, Chilkoti A. Tumor vascular permeability, accumulation, and penetration of macromolecular drug carriers. *Journal of the National Cancer Institute.* 2006;98(5):335-344.

[46] Weinstein J, Eger R, Covell D, *et al*. The Pharmacology of Monoclonal Antibodies. *Annals of the New York Academy of Sciences.* 1987;507(1):199-210.

[47] Langmuir VK, Mendonca HL, Woo DV. Comparisons between two monoclonal antibodies that bind to the same antigen but have differing affinities: uptake kinetics and 125I-antibody therapy efficacy in multicell spheroids. *Cancer research.* 1992;52(17):4728-4734.

[48] Thurber GM, Zajic SC, Wittrup KD. Theoretic criteria for antibody penetration into solid tumors and micrometastases. *Journal of Nuclear Medicine.* 2007;48(6):995-999.

[49] Dennis MS, Jin H, Dugger D, *et al*. Imaging tumors with an albumin-binding Fab, a novel tumor-targeting agent. *Cancer research.* 2007;67(1):254-261.

[50] Adams GP, Schier R, McCall AM, *et al*. High affinity restricts the localization and tumor penetration of single-chain fv antibody molecules. *Cancer research.* 2001;61(12):4750-4755.

[51] Minchinton AI, Tannock IF. Drug penetration in solid tumours. *Nature Reviews Cancer.* 2006;6(8):583-592.

[52] Thurber GM, Schmidt MM, Wittrup KD. Factors determining antibody distribution in tumors. *Trends in pharmacological sciences.* 2008;29(2):57-61.

[53] Reiter RE, Gu Z, Watabe T, *et al*. Prostate stem cell antigen: a cell surface marker overexpressed in prostate cancer. *Proceedings of the National Academy of Sciences.* 1998;95(4):1735-1740.

[54] Zhigang Z, Wenlv S. Prostate stem cell antigen (PSCA) expression in human prostate cancer tissues and its potential role in prostate carcinogenesis and progression of prostate cancer. *World Journal of Surgical Oncology.* 2004;2(1):13.

[55] Han K-R, Seligson DB, Liu X, *et al*. Prostate stem cell antigen expression is associated with gleason score, seminal vesicle invasion and capsular invasion in prostate cancer. *The Journal of urology.* 2004;171(3):1117-1121.

[56] Knowles SM, Zettlitz KA, Tavaré R, *et al*. Quantitative immunoPET of prostate cancer xenografts with 89Zr-and 124I-labeled anti-PSCA A11 minibody. *Journal of Nuclear Medicine.* 2014;55:452-459.

[57] Graff CP, Wittrup KD. Theoretical Analysis of Antibody Targeting of Tumor Spheroids Importance of Dosage for Penetration, and Affinity for Retention. *Cancer research.* 2003;63(6):1288-1296.

CHAPTER 2 - Automated VOI Analysis in FDDNP PET Using Structural Warping: Validation Through Classification of Alzheimer's Disease Patients.

Abstract

In this paper we evaluate an automated approach to the cortical surface mapping (CSM) method of VOI analysis in PET. Although CSM has been previously shown to be successful, the process can be long and tedious. Here we present an approach that removes these difficulties through the use of 3D image warping to a common space. We test this automated method using studies of FDDNP PET in Alzheimer's disease and mild cognitive impairment. For each subject, VOIs were created, through CSM, to extract regional PET data. After warping to the common space, a single set of CSM-generated VOIs was used to extract PET data from all subjects. The data extracted using a single set of VOIs outperformed the manual approach in classifying AD patients from MCIs and controls. This suggests that this automated method can remove variance in measurements of PET data, and can facilitate accurate, high-throughput image analysis.

2.1. Introduction

In the field of quantitative imaging, the creation of accurate volumes of interest (VOIs) is often of central importance. This process, however, can be time-consuming and is known to have variance introduced on inter- and intra-investigator levels. Various approaches have been employed to reduce the time and labor involved and the noise variance in the definition of VOIs [1, 2] . Most of these approaches try to map the images of individuals to a reference image in a common space. They vary on the mapping methods and on the selection of the common space and the reference image. A discussion of various methods and approaches is provided later in this section [2-4]. The choice of approach depends on the type of images (i.e., MRI or PET) and the desired VOIs one is considering. An approach that has been previously shown to be effective in accomplishing the spatial normalization of PET images is the use of hemispheric cortical surface mapping [2, 5]. However, the process involved is complex and labor intensive. An improved procedure suited for automated and streamlined operation is thus warranted. In this paper, we introduce a modified method that can reduce the variance in VOI analysis by warping structural and functional images to a common space in which valid VOIs already exist. This method is also easily adaptable to an automated approach to VOI analysis.

There have been previous attempts at similar methods, by creating maximum likelihood estimates (MLEs) of VOIs in a stereotaxic space [1]. In these methods, VOIs are manually drawn on several brains, which are normalized to a stereotaxic brain space such as the International Consortium for Brain Mapping (ICBM53) average space [6]. After a subject's brain image has been normalized to this space, MLEs can be used to create an individualized VOI based on the population of manually drawn VOIs. One drawback to using these methods is that when normalizing a subject's brain to the common stereotaxic space, it is difficult to balance how closely to match the target and template images. If the images are not matched closely enough, the MLEs for creating individualized VOIs lose their validity. However, if images are matched too closely to an average image of multiple brains, the structure of the subject's brain image can be lost when the normalization algorithm mistakes noise in the common space population as actual structural information. To reduce as much of the investigator-based variance as possible, it would seem ideal to use a library of previously created VOIs in a high-resolution single brain common space. There have been efforts to create such libraries [7], however the problem then becomes finding a way to closely normalize a subject's image to this single common space while maintaining its structural integrity.

Currently, there are many non-linear methods available for spatial normalization that use a wide array of image matching methods. Some of these methods use a set of smooth basis functions [3], while another large algorithm family contains the non-parametric methods such as Diffeomorphic Demons [8], ART [9], or SyN [4]. Additionally, there are methods such as the DARTEL algorithm in SPM8 [10] that use a fluid deformation model that simultaneously matches gray matter to gray matter, and white matter to white matter. Recently, fourteen such algorithms were tested against one another in MRI brain registration by Klein *et al.* [11]. The evaluation was done using 80 manually labeled MRI brain images, and eight separate measures of performance, in which the SyN algorithm was ranked the overall best. The rankings of each algorithm were relatively consistent across image sets, labeling protocols, and image matching metrics. Klein *et al*. believe this is strong evidence that these rankings can be generalized to other sets of subjects and labels. The SyN algorithm has the benefit of creating diffeomorphic deformations, so that there is no shearing or tearing of the image being deformed. Additionally, the SyN algorithm is not limited to imaging modalities that can be accurately segmented into gray and white matter, so it can be used in studies using non-T1-weighted MRIs. Therefore, we opted to use the SyN algorithm in our investigation of automated VOI analysis.

We apply this method to a set of MRI images that have corresponding PET images of the tracer, 2-(1-6-[(2-[^{18}F]fluoroethyl)(methyl)amino]-2-naphthylethylidene)malononitrile (FDDNP), which can bind to the cerebral β-amyloid plaques and neurofibrillary tangles (NFTs) characteristic of Alzheimer's disease (AD). The FDDNP PET images were obtained from a study in AD and mild cognitive impairment (MCI) patients. Patients classified as MCI do typically have a larger decline in cognitive function than normal aging, especially in memory, but do not show clinical signs of dementia [12]. Moreover, MCI patients do have a greatly increased chance of developing dementias such as AD over the non-MCI population [13]. The primary neuropathological characteristic of AD is accumulation of β-amyloid plaques and NFTs across numerous cortical regions. This accumulation of these misfolded protein aggregates follows a pattern of deposition described by Braak and Braak [14] , in which different cortical regions are affected at varying severity throughout the progression of the disease. Braak and Braak proposed three stages (A-C) for the deposition of β-amyloid, and six stages (I-VI) for the pattern of deposition of NFTs.

Although AD is clinically recognizable at late stages due to characteristic dementia and decline in cognitive abilities, current clinical diagnosis standards do not yet produce definitive differentiation between AD and non-Alzheimer's dementias (*e.g.*, frontotemporal dementia) [15-16]. However, current evidence shows that the accumulation of the neuropathological markers begins long before the onset of clinically recognizable symptoms [17]. In *post-mortem* studies, cognitively normal controls (clinical dementia rating (CDR) 0) have been shown to display density and distribution of β-amyloid and NFTs similar to mildly demented (CDR 0.5) patients [18]. In another *post-mortem* study, Peterson *et al.* reported clinically healthy controls whose NFT distribution spanned stages 0-V in the Braak and Braak progression, with 25% of these controls presenting NFTs consistent with at least stage III [19]. In the same study, Peterson *et al.* showed that once clinical symptoms are present, the Braak pathology stages do show correlation with the severity of symptoms. Of the MCI patients studied, 80% presented with Braak NFT stages II-IV and 91% of the AD patients presented with stages IV-VI [19].

In both living patients, as well as in *post-mortem* determinations, FDDNP signal has been shown to reside in areas with high β-amyloid plaque and NFT loads [2]. Along with the known spatial and temporal pattern of deposition, this suggests that molecular imaging using FDDNP PET may be a powerful tool in early detection and diagnosis of AD. For these same reasons, this compound is a good candidate for the evaluation of automated regional VOI analysis. In this work we validated the method of structural warping by examining the spatial overlap between the common space image and the warped MRIs in specific structures and regions. Furthermore, we validate the automated approach by comparing the efficacy of VOI data extracted from warped and unwarped functional images to create discriminant models classifying subjects as normal controls, MCI, or AD.

2.2 Methods

2.2.1 Subjects

The study group was comprised of 7 AD (76±10 years, 4:3 female/male), 6 MCI (73±13 years, 4:2 female/male) and 10 control (71±10 years, 7:3 female/male) subjects. Subjects were classified into groups using the diagnostic criteria for AD and amnestic MCI [2]. Subjects who had some memory symptoms but did not meet the diagnostic criteria for either disease group were classified as controls. No subject included in this study had a history of stroke, head injury, or non-Alzheimer's disease which would affect cognitive function. All subjects (n=23) were given mini-mental state examinations (MMSE) to assess cognitive abilities. AD patients had an average MMSE score of 23±2, MCIs had an average score of 27±1, and controls had an average score of 29±1. This subject population has been previously described by Protas *et al*. [2].

2.2.2 Imaging

A T1-weighted gradient echo (MP-RAGE) image was taken for each subject with a 3T Siemens Allegra MRI scanner (sagittal plane; repetition time (TR) 2300 ms; echo time (TE) 2.93 ms; 160 slices; slice thickness 1 mm; in-plane voxel size 1.3×1.3 mm; field of view 256×256; flip angle

8°) [2]. FDDNP was produced as described elsewhere [20], and each subject was given a bolus injection of FDDNP (320-550 MBq). A dynamic PET scan was taken for up to 125 min. (six 30s frames; four 180s frames; five 600s frames; and three 1200s frames). Imaging was performed using an ECAT EXACT HR+ scanner (Siemens Corp.). The images were reconstructed using filtered back-projection with attenuation correction. After the initial reconstruction, a movement correction algorithm was applied [21, 22]. This algorithm corrects for motion artifacts introduced during the 125 minute scan. Each emission frame is aligned with the transmission frame, and then reconstructed using the proper attenuation coefficients.

2.2.3 Creation of VOIs

All MRIs were normalized using the cortical surface mapping method. By this method, a 9-parameter linear registration is applied to bring all subjects into rough alignment with a common space, in this case the International Consortium for Brain Mapping (ICBM53) common space [6]. A 3D model of each subject's cortical surface (in the ICBM space) was extracted from their respective MRIs through the use of a method previously described by Thompson *et al.* [5]. On this model, 36 sulci major sulci and fissures were manually identified on each cortical surface, after which the surface was flattened to a 2D cortical surface map. The previously identified sulci and fissures were then redrawn on the flat map. These sulci were matched to an average 2D sulcal map through a nonlinear deformation. Inverting the flattening procedure and applying this deformation brought the 3D cortical surfaces of all subjects into close alignment. On the average cortical surface, nine ROIs were drawn bilaterally over the following regions: upper parietal lobe, posterior frontal lobe, prefrontal lobe, occipital-parietal lobes, posterior temporal lobe, upper temporal lobe, lower temporal lobe, medial temporal lobe, and the posterior-cingulate gyrus. These ROIs were projected into 3D VOIs by including each voxel within 9mm of the originally drawn voxels on the cortical surface. The inverse of the cortical surface mapping method for each subject was applied to these VOIs, such that each subject's MRI aligned to the ICBM space had an individualized set of these VOIs [2]. In addition, MRIs in the ICBM space were segmented into white and gray matter using the automated segmentation algorithm in SPM8 [23].

2.2.4 Creation of FDDNP-DVR Images

Logan analysis was performed on the movement corrected PET images to create FDDNP distribution volume ratio (DVR) images [21]. Following the procedure described previously by Kepe *et al.* [24] and Small *et al.* [25] , the cerebellar cortex was used as a reference region to approximate an input function. The first six minutes of the FDDNP scan – representing a perfusion image - were summed (frames 1-7), and a ROI was drawn over cerebellar cortex in that summed image. This ROI was then used to extract data from each individual frame, creating a time activity curve (TAC). Using this TAC as the input function for Logan analysis [26], the DVR value for each voxel was set to the slope of the respective Logan plot over the frames from 15 minutes to the end of the scan [2]. A rigid, linear transformation was calculated using SPM2 [23], to align the early summed FDDNP frames (0-6 minutes), to the MP-RAGE image. This transformation was then applied to DVR images, to bring it into alignment with the MRI [2].

2.2.5 Image Warping

Central to the method of automated VOI analysis is the ability to bring the imaging data of all subjects in close alignment with a common space. To accomplish this goal, we used the symmetric image normalization method (SyN) described by Avants *et al.* [4], as implemented in the software package ANTs [27]. The SyN algorithm creates a diffeomorphic mapping (that is, one that is both invertible and differentiable) along a geodesic path between a target image I and a template image J. SyN takes advantage of the fact that such diffeomorphisms can be decomposed into two parts, φ_1 and φ_2, such that the mapping $\varphi(I)=\varphi_2^{-1}(\varphi_1(I))= J$. This allows for the symmetry of the algorithm so that regardless of whether the image is the "target" or "template," the same deformation is computed. The sub-functions are defined such that the magnitudes of the deformations they define are equal, and that I and J contributed equally to the deformation. The SyN algorithm can create such a mapping with several different optimization metrics, but for our purposes, images were matched using localized cross-correlation (CC). This metric is a measure of local image mean and variance. It is computed over 3D windows, on the order of 5^3 voxels. Briefly, the algorithm sets up a global maximization of CC, which is translated into a series of Euler-Langrage equations which are then solved subject to several constraints. As stated above, the two sub-deformations must contribute equally and be both invertible and differentiable. The solutions are solved iteratively. These iterations are carried out at multiple levels of resolution. At each level, computation continues until convergence or a maximum number of iterations is reached.

2.2.6. Analysis

One control subject was designated as the common space (Fig. 1a bottom), to which all other subjects would be warped. For each remaining subject's MRI scan, a three-dimensional diffeomorphic warp was calculated to normalize it to the common space. This warp was computed to maximize cross-correlation in windows of size 4^3 voxels, between the common space and subject images. The software ANTs employs a multi-scale resolution approach to image warping. We chose to use four levels of resolution with scaling factors [8, 4, 2, 1], with the maximum iteration number set for each level as [100, 100, 50, 20]. This warp was applied to all previously drawn VOIs, segmentation images, and co-registered FDDNP-DVR images for that subject. For each subject, the average FDDNP-DVR values in each of the nine VOIs were measured. This measurement was first performed using a subject's VOI to extract data from the respective unwarped PET image (unwarped data). Next, average DVR values were extracted from warped PET images using VOIs created for the common space MRI (warped data). The warping algorithm was evaluated using the Dice overlap statistic, κ, calculated between the regions of the common space image and the regions of subjects warped into the common space.

$$k = 2 * \#(A \cap B)/[\#(A) + \#(B)] \qquad \text{Eq.1}$$

This measure has a range of [0,1], and captures the overlap between two regions, A and B. The #(X) operator returns the number of voxels contained in region X. Although there is no way to determine statistical significance of this measure in this context, some investigators consider good results to be $\kappa > 0.6$ for smaller structures and $\kappa > 0.8$ for larger structures [4].

Using the statistical software SPSS (SPSS 15.0 for Windows), discriminant analysis was performed to classify subjects into three groups (control, MCI, or AD). In addition to classifying subjects solely on MMSE scores, an exhaustive search of two classes of models was performed. In the first class, models were built using unwarped FDDNP-DVR data extracted from all possible combinations of VOIs; the second was built similarly, except using warped FDDNP-DVR data extracted using the common space VOIs. In both classes, models were built with and without the use of MMSE as a predictor variable. Models in all categories were ranked by classification ability and leave-one-out cross validation. It is possible that the exhaustive search for best discriminant models led to some survivorship bias. To correct for this possible artifact, we performed a permutation test on the best models found. In this test, the null hypothesis is that there is no underlying structure to the data and permuting the data labels (control, AD, or MCI) would have no effect on the ability to classify subjects into their respective groups. The group labels were randomized, keeping the distribution of groups the same (10 control, 7 AD, 6 MCI). For each randomization, linear discriminant analysis was performed on the permuted data, and the correct classification percentage was calculated. This was repeated 100,000 times for each of the best models initially discovered. The significance level is then determined as the percentage of randomized models that performed as well or better than the correctly labeled data [28].

2.3 Results

Figure 1a shows results of the SyN warping algorithm. The average of 22 subject MRIs registered to common space with nine parameter linear registration alone (top), and with the SyN algorithm (middle) are shown alongside the common space (23rd subject's) MRI (bottom). Images warped to the common space showed a 54% reduction in average absolute voxel-to-voxel variance within the brain (excluding skull and scalp) as compared to variance measured after a nine parameter linear registration alone (Fig. 1b). The average (±SD) overlap ratio, κ, measured between structures in the common space, and those of the 22 remaining subjects warped into the common space are shown in Fig. 2. In addition to those for the nine VOIs, overlap between subjects and the common space was also measured for white matter, gray matter, and whole brain structures. In this case, the whole brain is defined as all voxels contained within the cortical surface, as calculated by Protas *et al*. [2].

Table 1 shows the best results of the discriminant analysis carried out in SPSS. The models shown are those that had the highest leave-one-out cross validation scores of all the possible discriminant models in their respective classes. The table shows the classification performance using the original sample (n=23), and with leave-one-out cross validation. The numbered regions indicated in Table 1 and Fig. 2 correspond to those represented in Fig. 3. All models shown use FDDNP-DVR data from the occipital-parietal region, the posterior temporal lobe, and the posterior cingulate gyrus. FDDNP-DVR data from the medial temporal lobe is also used in all but one of the models shown. Histograms of the classification percentage of models yielded by the permutation test are shown in Fig. 4. Each histogram in Fig. 4 also shows the classification percentage of the true, non-permuted data.

2.4 Discussion

As can be seen in Fig. 1, the SyN algorithm is a powerful tool in normalizing a set of structural images. The set of brains, including some with severe cortical degeneration, were mapped almost exactly to a common space, with the borders between sulci and gyri very clearly maintained. The strength of this method is reinforced by the overlap data shown in Fig. 2. Although there is no way of describing statistical significance of the overlap statistic in this particular situation, we do see average κ>0.7 for each of the VOIs, which are relatively small structures, and only project 9mm deep into cortex. It is also conceivable that some of the variation is due to the original creation of the VOIs. Although the VOIs were created from a single set drawn on the average cortical surface map, the registration of MRIs to that space was still dependent on manual steps where inter- or intra-investigator variation could have been introduced. Therefore, it is possible that some of the missed overlap in these VOIs is due to the imperfect nature of the original cortical surface mapping. In addition, the fact that we see κ> 0.9 for white and gray matter is especially noteworthy, as we are warping the MRIs of some AD patients with severe cortical degeneration. It is non-trivial that a mapping that preserved sulcus/gyrus boundaries would also maintain cortical gray/white matter boundaries. It is likely that the preservation of these boundaries is due to the use of CC metric. Since the metric is based on matching local variances, as long as tissue types are distinguished by the imaging modalities used, the boundaries between these tissues are likely to be very strictly maintained. Thus, not only does SyN successfully match images visually, but micro- and macro-structures are preserved and matched as well. These results show that the SyN algorithm is an excellent tool for this specific task of image matching. It requires minimal user input, which allows for high-throughput automation, as well as minimizes variance introduced by the investigator. Also, in investigations where one needs to measure the exact spatial distribution of a tracer, an algorithm such as SyN performs quite well because images are matched while maintaining structural boundaries without shearing or tearing.

Table 1 shows that data extracted from FDDNP-DVR images using a single set of VOIs in a common space outperforms data extracted using individual VOIs for each subject in classifying subjects as control, MCI, or AD. Table 1 also shows that the use of FDDNP-DVR can improve classification over using MMSE alone. In addition, the models using warped data use fewer predictor variables than those using unwarped data. Table 1 and Fig. 4 show that discrimination between subject classes is likely not a result of survivorship bias, as the p-value for all models is very low, and for the model using warped data and MMSE, not one of the 100,000 permutations of data labels resulted in a model performing as well as the true data. It is possible that this is a result of decreased noise in measurement of PET data due to standardization of VOI analysis, as with fewer predictor variables we are fitting less noise. There is a reduction in the performance of models when looking at cross-validation scores compared to simple classification, although this could likely be a result of the sample size of this study. Here we had a sample of 23 subjects, so for cross-validation the models are built with 22 subjects classified into three sub-populations. In this situation a small amount of misclassification can lead to a large percentage drop in accuracy. It should also be noted that all the discriminant models shown in Table 1 use FDDNP-DVR information from similar regions and from those closely associated with the classical pathological progression of AD, as described by Braak and Braak [14]. All models use data from the occipital-parietal region, the posterior temporal lobe and the posterior cingulate gyrus. The occipital-parietal VOI includes regions of the basal isocortex where initial deposits of amyloid plaques are found, with increasing deposition in stages B and C. This region also shows large amounts of NFTs in late stages of the disease. The posterior temporal lobe and posterior cingulate gyrus both see initial amyloid deposition in stage B with increasing deposition in stage C. Like the occipital-parietal region, these areas also show large amounts of NFT deposition in late stages of the disease. Many of the models also use data from the medial temporal lobe, which is the major site of accumulation for NFTs [14]. Although this is a region canonically associated with the pathological markers of AD, it is possible that it was replaced by MMSE as a predictor variable because FDDNP binding and MMSE share predictive strength for disease state. Giannakopoulos *et al.* [29] have described that NFT density in the entorhinal cortex is a strong predictor of MMSE in elderly subjects. Thus it is possible that for this VOI, MMSE and DVR values supply redundant information. As discussed previously, deposition of plaques and NFTs in the medial temporal lobe occurs quite early in the progression of the disease, even before the appearance of clinical symptoms. Therefore, it is also possible that this region might be a weaker predictor of discrimination between non-control states (AD and MCI), as elevated FDDNP-DVR values in the medial temporal lobe are present in control subjects and plateau for these non-control subjects. It should also be noted that no special weighting was put on any regions in the search for the best discriminant models.

Central to the utility of this method for further study is the ability to create meaningful and accurate VOIs in a common space for use across data sets. In this paper we have only used VOIs created via cortical surface mapping, and projection into cortex. This procedure has the benefit of creating VOIs that adhere strictly to well-defined cortical regions, and can also be tailored to different studies by projecting different depths into cortex depending on the desired application. This method also gains strength when combined with a tool such as the SyN algorithm which, as shown above, strongly matches tissue morphology between subjects. An obvious drawback to this method is its inability to define VOIs over non-cortical regions, such as the amygdala or thalamus. However, for well-defined neurological structures such as those, manual creation of such VOIs can be carried out with relative ease, and added to a library of VOIs covering a high-resolution common space MRI.

Given the success of this warping method with respect to the classification of subjects with neurological disease, we believe that this can be expanded to a wide variety of applications. First and foremost, it can be used to facilitate accurate high-throughput PET image analysis, by greatly reducing the time needed to extract regional information, while removing several sources of experimental variance. In these applications, almost the entire process of data collection can be streamlined into an automated procedure for clinical applications. Given predefined reference region VOIs, methods such as Patlak or Logan analysis can by automated and normalized, reducing the manual work load required for such methods, and removing variance caused by *ad hoc* definitions of reference regions. In a similar fashion, such a method could be applied to facilitate the use of image-derived input functions for kinetic PET imaging. Once experimentally appropriate analysis has been performed on the raw PET data, the process of regional data extraction can be automated entirely, as shown above. Moreover, this method can be used to facilitate multi-center trials, by using identical image analysis and data extraction across many subjects, investigators and locations.

2.5 Conclusions

We have shown that the use of the SyN algorithm is a powerful tool for automated image normalization that maintains good alignment of biologically important structures of the warped images. We have also shown that by normalizing data to a common space and using a set of VOIs pre-drawn in that space, one can actually improve the predictive quality of data extracted from functional images. In addition to being able to better classify subjects into their diagnostic groups, we can do so using fewer predictor variables. This is perhaps due to an elimination of intra-investigator, and inter-subject variability by using a single set of VOIs. These results seem to suggest that with a larger sample of subjects with AD and non-Alzheimer's dementias, a protocol could be developed to greatly increase the ability to clinically diagnose patients into their proper groups based on differences in the binding patterns. These results also suggest that automation of VOI analysis through spatial normalization to a single common space brain image can be used to streamline accurate, high-throughput PET image analysis for use in clinical settings. This method is expected to be applicable to longitudinal studies of cognitive impairment as well as to other PET tracers (e.g., other probes for AD imaging), but further study is warranted.

Acknowledgements

We would like to thank Dr. Paul Thompson for his assistance with the cortical surface mapping technique, Dr. Avants of the University of Pennsylvania for the production of the ANTs package, Mr. David Truong and his group for the computational assistance, and Dr. Satyamurthy and the cyclotron facility for the production of FDDNP.

Funding

Supported by NIH grants P01-AG025831, M01-RR00865, the Department of Energy (DOE contract DE-FC03-87-ER60615); General Clinical Research Centers Program; and the Elizabeth and Thomas Plott Endowment in Gerontology. No company provided support of any kind for this study.

Financial Disclosure

The University of California, Los Angeles, owns a U.S. patent (6,274,119) entitled "Methods for Labeling β-Amyloid Plaques and Neurofibrillary Tangles," that uses the approach outlined in this article. Drs. Small, Huang, and Barrio are among the inventors, have received royalties, and may receive royalties on future sales. Dr. Small reports having served as a consultant and/or having received lecture fees from Eisai, Forest, Medivation, Novartis, and Pfizer.

References

[1] Hammers A, Allom R, Koepp MJ, *et al*. Three-dimensional maximum probability atlas of the human brain, with particular reference to the temporal lobe. *Human Brain Mapping.* 2003;19(4):224-247.

[2] Protas HD, Huang S-C, Kepe V, *et al*. FDDNP binding using MR derived cortical surface maps *NeuroImage.* 2010;49(1):240-248.

[3] Friston KJ, Ashburner J. Nonlinear spatial normalization using basis functions. *Human Brain Mapping.* 1999;7(4):254-266.

[4] Avants BB, Epstein CL, Grossman M, Gee JC. Symmetric diffeomorphic image registration with cross-correlation: Evaluating automated labeling of elderly and neurodegenerative brain. *Medical Image Analysis.* 2008;12(1):26-41.

[5] Thompson PM, MacDonald D, Mega MS, Holmes CJ, Evans AC, Toga AW. Detection and mapping of abnormal brain structure with a probabilistic atlas of cortical surfaces. *Journal of Computer Assisted Tomography.* 1997;21(4):567-581.

[6] Mazziotta J, Toga A, Evans A, *et al*. A probabilistic atlas and reference system for the human brain: International Consortium for Brain Mapping (ICBM). *Philosophical Transactions of the Royal Society of London B Biological Sciences.* 2001;356(1412):1293-1322.

[7] Tzourio-Mazoyer N, Landeau B, Papathanassiou D, *et al*. Automated anatomical labeling of activations in SPM using a macroscopic anatomical parcellation of the MNI MRI single-subject brain. *Neuroimage.* 2002;15(1):273-289.

[8] Vercauteren T, Pennec X, Perchant A, Ayache N. Diffeomorphic demons: Efficient non-parametric image registration. *Neuroimage.* 2009;45(1):S61-S72.

[9] Ardekani BA, Guckemus S, Bachman A, Hoptman MJ, Wojtaszek M, Nierenberg J. Quantitative comparison of algorithms for inter-subject registration of 3D volumetric brain MRI scans. *Journal of Neuroscience Methods.* March 15 2005;142(1):67-76.

[10] Ashburner J. A fast diffeomorphic image registration algorithm. *Neuroimage.* 2007;38(1):95-113.

[11] Klein A, Andersson J, Ardekani BA, *et al*. Evaluation of 14 nonlinear deformation algorithms applied to human brain MRI registration. *Neuroimage.* 2009;46(3):786-802.

[12] Petersen RC. Mild cognitive impairment as a diagnostic entity. *Journal of Internal Medicine.* 2004;256(3):183-194.

[13] Gauthier S, Reisberg B, Zaudig M, *et al*. Mild cognitive impairment. *The Lancet.* 2006;367(9518):1262-1270.

[14] Braak H, Braak E. Neuropathological stageing of Alzheimer-related changes. *Acta Neuropathologica.* 1991;82(4):239-259.

[15] Dubois B, Feldman HH, Jacova C, *et al*. Research criteria for the diagnosis of Alzheimer's disease: revising the NINCDS– ADRDA criteria. *The Lancet Neurology.* 2007;6(8):734-746.

[16] Varma AR, Snowden JS, Lloyd JJ, Talbot PR, Mann DMA, Neary D. Evaluation of the NINCDS-ADRDA criteria in the differentiation of Alzheimer's disease and frontotemporal dementia. *Journal of Neurology, Neurosurgery & Psychiatry.* 1999;66(2):184-188.

[17] Kepe V, Huang S-C, Small GW, Satyamurthy N, Barrio JR. Microstructural Imaging of Neurodegenerative Changes. In: Silverman D, ed. *PET in the Evaluation of Alzheimer's Disease and Related Disorders*. New York: Springer; 2009.

[18] Price JL, Morris JC. Tangles and plaques in nondemented aging and "preclinical" Alzheimer's disease. *Annals of Neurology.* 1999;45(3):358-368.

[19] Petersen RC, Parisi JE, Dickson DW, *et al*. Neuropathologic features of amnestic mild cognitive impairment. *Archives of Neurology.* 2006;63(5):665-672.

[20] Liu J, Kepe V, Zabjek A, *et al*. High-yield, automated radiosynthesis of 2-(1-{6-[(2-[18F]Fluoroethyl)(methyl)amino]-2-naphthyl}ethylidene)malononitrile ([18F]FDDNP) ready for animal or human administration *Molecular Imaging and Biology.* 2007;9(1):6-16.

[21] Wardak M, Wong K-P, Shao W, *et al*. Movement correction method for human brain PET Images: application to quantitative analysis of dynamic F18-FDDNP scans. *The Journal of Nuclear Medicine.* 2010;51(2):210-218.

[22] Wong KP, Wardak M, Shao W, *et al*. Movement correction of [18F]FDDNP PET studies for brain amyloid imaging. Paper presented at: Nuclear Science Symposium Conference Record, 2007.

[23] Friston KJ, Ashburner J, Kiebel S, Nichols T, Penny W, eds. *Statistical Parametric Mapping: The Analysis of Functional Brain Images.* 1 ed. Boston: Academic Press; 2007.

[24] Kepe V, Huang S-C, Small GW, Satyamurthy N, Barrio JR. Visualizing pathology deposits in the living brain of patients with Alzheimer's disease. *Methods in Enzymology.* 2006;412:144-160.

[25] Small GW, Kepe V, Ercoli LM, *et al*. PET of brain amyloid and tau in mild cognitive impairment. *New England Journal of Medicine.* 2006;355(25):2652-2663.

[26] Logan J, Fowler JS, Volkow ND, Wang G-J, Ding Y-S, Alexoff DL. Distribution volume ratios without blood sampling from graphical analysis of PET data. *Journal of Cerebral Blood Flow & Metabolism.* 1996;16(5):834-840.

[27] Avants BB. Advanced Normalization Tools. Electronic Distribution. Available at: http://picsl.upenn.edu/ANTS/.

.

[28] Nichols TE, Holmes AP. Nonparametric permutation tests for functional neuroimaging: a primer with examples. *Human Brain Mapping.* 2001;15(1):1-25.

[29] Giannakopoulos P, Herrmann FR, Bussiere T, *et al*. Tangle and neuron numbers, but not amyloid load, predict cognitive status in Alzheimer's disease. *Neurology.* 2003;60(9):1495-1500.

Figures and Tables

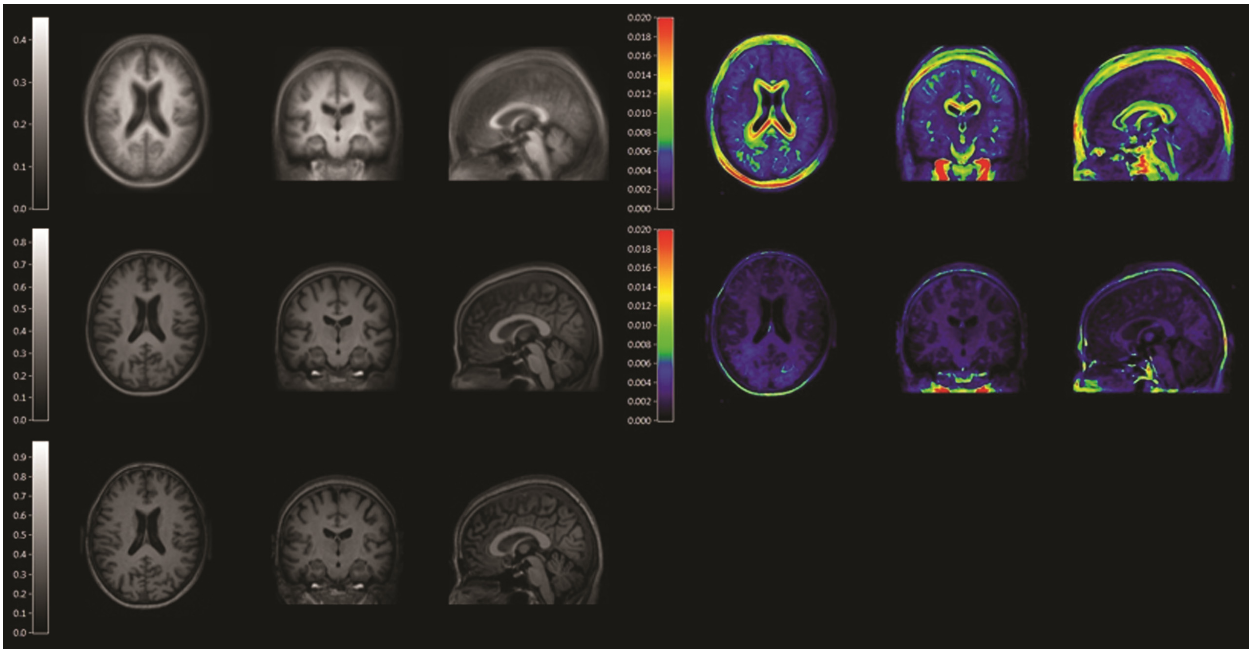

FIGURE 1. (a) (Left) Warping Results: Average of 22 subjects MRIs after linear registration only (Top); Average of 22 subjects after warping to common space. (Middle); MRI of common space subject (Bottom). (b) (Right) Absolute voxel-to-voxel variance of unwarped (Top) and warped (Bottom) MRIs. Warping reduces average in-brain variance by 54% from linear registration alone.

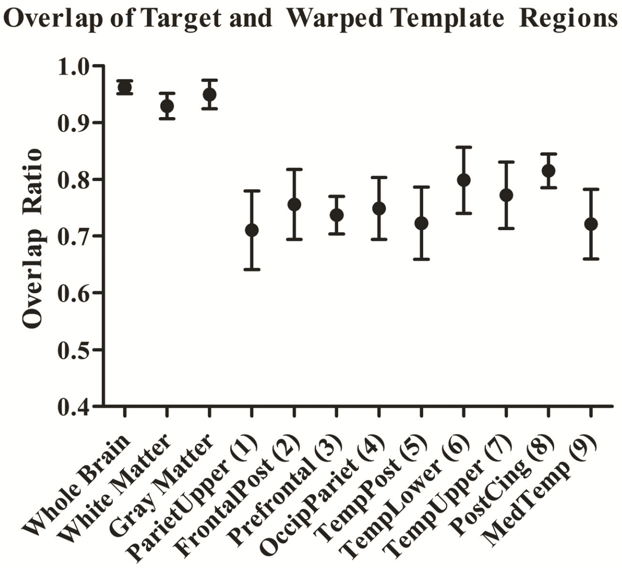

FIGURE 2. Overlap Statistic by Region. Data shown is average overlap, ± SD, between common space regions and warped regions of remaining 22 subjects

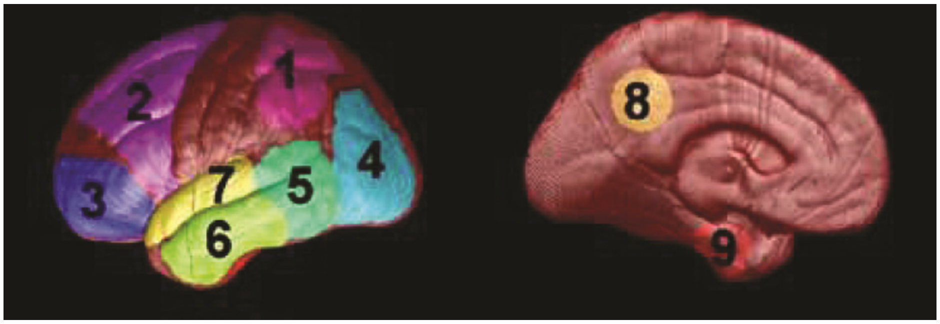

FIGURE 3. Generalized image of the VOIs used to extract FDDNP data *Reprinted from Protas *et al.*2010 [2]

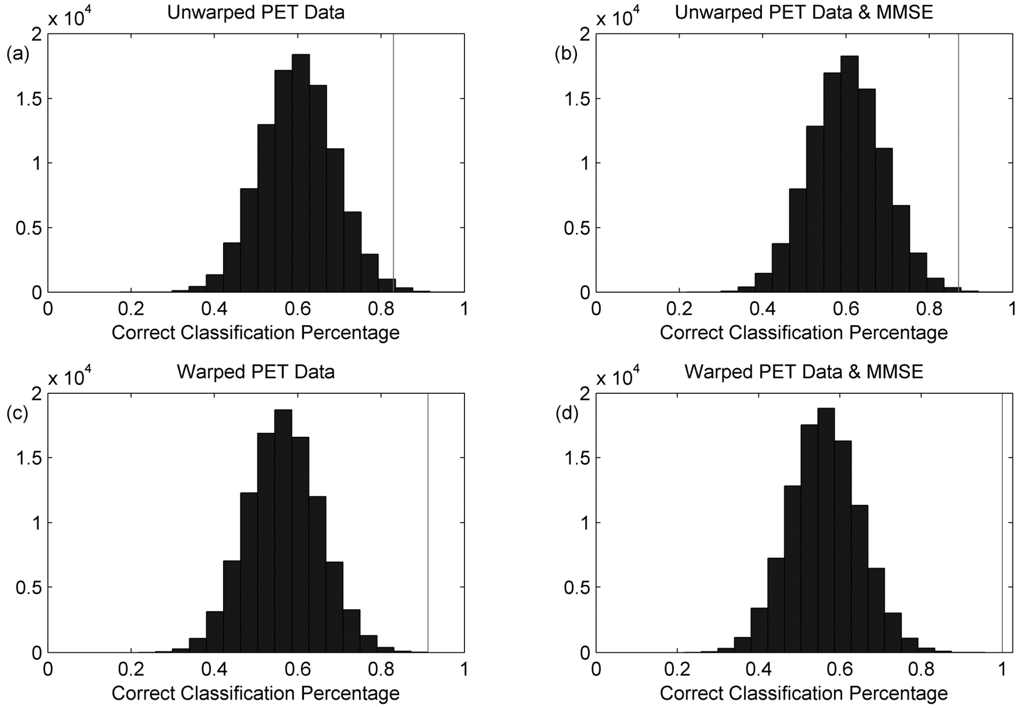

FIGURE 4. Classification Percentages of Permutation Test. Data shown are for the models using (a) unwarped data only, (b) unwarped data and MMSE, (c) warped data only, and (d) warped data and MMSE. The vertical line represents the score of the true data.

TABLE I: Best Discriminant Models

Model	Classification (%)	Cross-Validation (%)	Regions Used	Permutation Significance
MMSE Only	77.3	77.3	N/A	N/A
Unwarped PET Data Only	82.6	73.9	2,4,5,8,9	$p = 3.42*10^{-3}$
Warped PET Data Only	87	73.9	4,5,8,9	$p = 1.3*10^{-4}$
Unwarped PET Data & MMSE	91.3	87	4,5,8,9	$p = 8.6*10^{-4}$
Warped PET Data & MMSE	100	95.7	4,5,8	$P<10^{-5}$ †

† (None of the 100,000 permutations resulted in a model that performed as well as the true data)

CHAPTER 3 - Evaluation of the use of Voxel-Value Distribution in Target Regions for Prediction of Changes in Longitudinal FDDNP-PET Studies

Abstract

When using mean values of target regions, heterogeneous tracer localization leads to decreased signal-to-noise ratios, as true signal is masked by background values. This study proposes a method for modeling the statistical distribution of voxel values within a given volume of interest (VOI).We examined longitudinal imaging of the tracer FDDNP in control and mild cognitive impairment (MCI) subjects, as heterogeneously localized amyloid plaques and tau protein are involved in MCI. Subjects (16 Control and 18 MCI) underwent an initial dynamic FDDNP scan and a follow-up scan after 2 years. Subjects also underwent a battery of psychological tests at baseline and follow-up examinations.

Logan and relative equilibrium analysis was performed on all scans to create distribution volume ratio (DVR) images. The distributions of voxel DVRs in 9 VOIs canonically associated with the pathological progression of Alzheimer's disease were obtained. Each distribution was modeled as a sampling from a statistical admixture of "healthy" and "diseased" tissue. Means, variances, and admixture proportions for these distributions were fit using an EM optimization algorithm. Regression models were built to predict the rate of change in the admixture parameters between baseline and follow-up scans, using admixture parameters from the baseline scan as the independent variables. Regression models were also used to predict the rate of change in psychological scores between examinations using admixture parameters from the baseline PET scan as a predictors. Separate models were built for controls and MCI subjects

Models built using statistical parameters greatly outperformed those based on mean VOI values in predicting the rate of amyloid accumulation and cognitive decline. In models predicting rates of pathological progression, mean adjusted-R^2 was 0.42 ± 0.17 when using mean-VOI measures as predictors, and improved to 0.79 ± 0.09 when using statistical parameters. Similarly, in models predicting rates of cognitive decline, using mean-VOI measures at predictors resulted in mean adjusted-R^2 of 0.38 ± 0.16, which improved to 0.75 ± 0.10 when using statistical parameters from the initial scan instead. Accounting for non-Gaussian distributions of tracer in target VOIs can greatly increase the predictive quality of data, with trivial increases in data processing time. Although the method was used on FDDNP, it is highly applicable to other amyloid-binding tracers such as ^{11}C-PIB, as well as to other dementias and diseases.

3.1 Introduction

The creation of accurate volumes of interest (VOIs) can be a major barrier in quantitative brain imaging, especially in large scale studies involving subjects with a wide range of pathological conditions, including cortical degeneration. We have previously shown that through a combination of cortical surface mapping and structural warping, VOIs can be robustly and automatically generated, improving the diagnostic utility of PET data in classifying between healthy controls, mild cognitive impairment (MCI), and Alzheimer's disease (AD) patients [1, 2]. In addition to removing variance introduced through inter- or intra-investigator variability, the number and size of VOIs generated by this method can be much larger than what would be generated by through manual definitions, giving a more complete representation of the biological phenomena being assayed.

In most VOI analyses in PET, only the mean activity (or some biologically relevant parametric value) is measured, even when large VOIs are created from a previously existing atlas, which assumes normality of tracer distribution in tissue [3]. However, there are many cases in which this will likely not be the case, such as the distribution of β-amyloid plaques and neurofibrillary tangles of tau protein (NFTs), characteristic of Alzheimer's disease (AD). In AD, the accumulation of these misfolded protein aggregates follows a well established pattern described by Braak and Braak, with three stages (A-C) of amyloid deposition, and six stages (I-VI) of NFT deposition [4]. However, this deposition begins long before clinical symptoms are recognizable, with *post-mortem* studies of cognitively normal controls showing β-amyloid and NFT distribution similar to mildly demented subjects, and having NFT distributions spanning Braak and Braak stages 0-V [5-7]. Furthermore, previous work has shown that within a single subject, the density of amyloid plaques and NFTs may not be uniformly distributed, meaning simple mean-value measures in PET may be insufficient to accurately describe pathology [7]. Work by Petersen *et al.* has shown that increases in Braak pathology stages correlate with increases in severity of clinical symptoms, meaning that accurate *in vivo* measurement of pathology through PET can be central in staging and predicting progression of disease [6].

In this work, we examine longitudinal changes in pathology and clinical symptoms in healthy controls and MCIs, using both mean-value measures and voxel-distribution measures, as made possible by the automated creation of large, structurally consistent VOIs. Subjects who have been diagnosed with MCI have a larger decline in cognitive function than expected by healthy aging, and although they do not show signs of dementia, they do have a greatly increased risk for developing AD and other dementias over the normal population [8-9]. In *post-mortem* studies, it has been shown that 80% of amnestic-MCI patients present brain pathologies similar with Braak

NFT stages II-IV, implying that this study population should show substantial binding of AD tracers with sensitivity for tau aggregates[6].

There are currently many PET tracers that bind to either amyloid plaques or NFTs, but in this study we use the tracer, 2-(1-6-[(2-[^{18}F]fluoroethyl)(methyl)amino]-2-naphthylethylidene) malononitrile (FDDNP) which has been shown to bind to both pathological proteins [2, 10-12]. To measure amyloid and NFT intensity in images, we created distribution volume ratio (DVR) images using both Logan graphical analysis and relative equilibrium (RE) analysis, as previous work has demonstrated that RE has shown some improvement over Logan in FDDNP [13-15]. Additionally, we created SUVr parametric images for all subjects, as it has been previously shown that SUVr can provide similar information to DVR images without a full dynamic scan, and which is also commonly used for other AD tracers [16-18]. In this work, we validate the use of voxel-value distribution data over mean-value measures in predicting longitudinal changes in both pathological progression of protein deposition and cognitive decline, based on initial FDDNP-PET imaging.

3.2 Methods

3.2.1 Subjects

The final study group was comprised of 18 MCI (64±9 years, 11:7 female/male) and 16 control (63±12 years, 10:6 female/male) subjects. Originally 22 MCI and 22 control subjects were retrospectively enrolled for this study, however 10 subjects had to be removed due to missing or corrupted imaging data. All subjects were given a battery of psychological exams including mini–mental state examination (MMSE) and the Hamilton Rating Scale for Depression. Exams were also given to test language (Animal Naming Test), executive functioning (Stroop

Interference and Trail making B), visuo-spatial (Block Design), information processing (WAIS-III Digit Symbol), and memory (Rey-Osterrieth Complex Figure Recall) abilities. The time (μ±SD) between examinations was 2.1±0.6 years for MCI subjects and 2.3±1.5 years for control subjects. For all subjects, psychological Z-scores were created for performance in specific areas of brain function [19].

3.2.2 Imaging

MRI - A T1-weighted gradient echo (MP-RAGE) image was taken for each subject with a 3T Siemens Allegra MRI scanner (sagittal plane; repetition time (TR) 2300 ms; echo time (TE) 2.93 ms; 160 slices; slice thickness 1 mm; in-plane voxel size 1.3×1.3 mm; field of view 256×256; flip angle 8°). Each MRI was segmented into grey matter, white matter, and cerebrospinal fluid using SPM8. All MRIs were non-linearly normalized to a high resolution control MRI, through a method described below. A library of VOIs was previously defined on this control brain through cortical surface mapping [20].

PET - At both the initial and follow-up visit each subject underwent a dynamic FDDNP PET scan. FDDNP was produced as described elsewhere [21], and each subject was given a bolus injection of FDDNP (210-440 MBq). A dynamic PET scan was taken for up to 125 min. (six 30s frames; four 180s frames; five 600s frames; and three 1200s frames). All imaging was performed using an ECAT EXACT HR+ or ECAT EXACT HR scanner (Siemens Corp.). The images were reconstructed using filtered back-projection with attenuation correction. After the initial reconstruction, movement correction was applied [22, 23]. This corrected the motion artifacts introduced during the 125 minute scan. Each emission frame was aligned with the transmission frame, and then reconstructed using the proper attenuation coefficients.

3.2.3 Image Normalization

For each MRI, a non-linear diffeomorphic mapping was computed to normalize the image to a common space atlas. This mapping was computed, as described before [1], using the software package Advanced Normalization Tools (ANTS), as described by Avants *et al*. [24, 25]. This mapping was applied to the previously defined library of VOIs (including 9 cortical regions, subcortical white matter, and cerebellum), to bring them into each patient's MRI space. MRIs, along with the segmentation images and normalized VOIs, were rigidly co-registered to their respective PET images, and down-resolved into PET resolution.

3.2.4 Creation of Parametric FDDNP Images

For each subject and time point, several different parametric images were generated from the dynamic FDDNP scan. Distribution volume ratio (DVR) images were generated using both Logan graphical analysis, and relative equilibrium (RE) analysis [13, 14]. Additionally, SUVr was calculated using the frames from 35-45 minutes, as described by Wong *et al.* [16]. For all of these parametric images, cerebellar grey matter was originally used as a reference region, but there was evidence of increased signal in cerebellum between initial and follow-up scans in some subjects, which is in alignment with existing literature showing deposition of both β-amyloid and tau protein in the cerebellum [26,27]. Therefore, we instead used subcortical white matter, as described by Wong *et al.*, as a reference region [28]. All parametric images were computed using reference region VOIs that were generated automatically from the image normalization algorithm.

3.2.5 Data Measurement and Analysis

For each parametric image (SUVr, Logan-DVR, and RE-DVR), grey matter activity was measured bilaterally across nine cortical regions (Fig. 3.1) using the VOIs that were automatically generated from the common space atlas, combined with the MR-derived gray matter mask of each individual subject. The extracted data was recorded either as a mean of the whole-VOI (mean-value data), or as a vector of all voxel-values within that VOI (distribution-value data). Voxel-value data was modeled statistically as an admixture of two normal distributions, representing healthy and diseased tissue (Eq. 1). This model was fit using an iterative EM algorithm [29] to maximize likelihood for values of mean (μ_1, μ_2), variance (σ^2_1, σ^2_2), and admixture percentage (p) for both tissue types. Without loss of generality, the model was constrained ($\mu_1 \leq \mu_2$) so that distribution 1 represented healthy tissue. The EM algorithm used to fit these parameters, and a discussion of its accuracy can be found in the supplemental data section of this chapter.

$$MeasuredActivity = (1-p)N(\mu_1, \sigma_1) + pN(\mu_2, \sigma_2) \qquad \text{Eq.1}$$

For each VOI measured, linear regression models were built to predict the rate of change (units/day) in the measured (whole-VOI mean), and estimated (μ_1, μ_2,etc.) parameters, from the initial to follow-up scan. In models predicting changes in VOI means, the measured mean activity in all VOIs in the baseline scan were included as possible predictors. In models predicting changes in estimated admixture parameters, all estimated parameters from all VOIs in the baseline scan were included as possible predictors. In both cases, models were limited to a maximum of 3 predictor variables, as sample sizes were relatively small. Models were built using both zero and non-zero intercepts for regression. Optimal models in all cases were chosen on the basis of adjusted-R^2 under the requirement that all regression parameters were significantly different from zero. Similarly, regression model selection for the rates of change in psychological Z-scores were built using either VOI means or admixture parameters from all nine VOIs in the initial scan as possible predictors. A more complete description of the regression models can be found in the supplemental data section of this chapter.

Because of the large number of possible predictors in distribution-value models and the complex nature of β-amyloid and tau progression in the brain, partial least squares regression (PLS) [30] was also used in the case of admixture parameter regression. The method of PLS regression involves projecting the matrix of observations, X , into a smaller dimensional set of factors X', that is used as the regressor for the response variable Y. PLS regression thus works well in cases where there are more variables than observations, and when there is multicollinearity or error in the original observations. These improvements make PLS an ideal tool for modeling a cortically global and interconnected disease such as AD. The number of factors used in PLS modeling was chosen using Wold's R criterion through leave-one-out cross-validation [30]. Weak predictors (those with low PLS-weightings and small regression coefficients) were iteratively trimmed from the model, as suggested previously [30,31], to reduce the total number of predictors used. All PLS processing was performed using SAS 9.4. In all cases, separate models were built for MCI and control subjects.

3.3 Results

All subjects were successfully aligned with the common space atlas through structural warping. Representative images from warping the common space atlas to a single subject are shown in Figure 3.2. In all regions, there was a negative correlation between mean DVR values at baseline and the rate of change in mean DVRs over time (p = -0.64±0.12 (μ±SD) for MCIs and p = -0.44±0.07 (μ±SD) for controls).

For both Logan and RE-generated DVR images, distribution-data was fit well by admixture modeling, showing non-normal distributions of voxel-values within VOIs throughout the cortex in both controls and MCIs. Voxel-value distributions of SUVr, while non-normal, showed reduction in mean activity in both whole-VOI and admixture distributions in approximately 40% of the VOIs measured, thus disallowing reasonable models of disease progression. A representative graph of Logan-DVR distribution-value data and the admixture fit for a single subject and single VOI is shown in Fig. 3.3. Distributions of RE-DVR show similar admixture fits to those of Logan-based graphical analysis.

Regression results predicting rates of change in pathological progression of the disease are shown in Tables 3.1 and 3.2. Data shown is the adjusted-R^2 values from the best regression model found for each VOI and data measurement technique. For models using distribution-value measures, data shown is mean ± SD of adjusted-R^2 values of regression models for distribution parameters in that region. Similar results for predicting the rate of change in psychological scores based on initial Logan and RE DVR data is presented in Tables 3.3 and 3.4. Full regression model details can be found in the Supplemental Data section. Representative scatter plots of regression results can be seen in Figures 3.4 and 3.5.

3.4 Discussion

As can be seen in Figure 3.2, and as shown previously [1], the warping algorithm results in highly accurate structural matching between subjects of varying degrees of cortical degeneration. Therefore, this matching facilitates accurate automated data extraction from a wide range of subjects without the introduction of inter- or intra-investigator variance. Because two brain images are never going to be perfectly matched to one-another on a voxel-by-voxel basis, it is possible that automatically generated VOIs will not perfectly match homologous structures between patients, due to either warping or interpolation artifacts. However, when combined with a grey-matter segmentation of the subject's MR, these small errors can be substantially minimized. Additionally, with automated VOI generation, it is possible to measure regions covered by thousands of voxels, much larger than would normally be feasible with manually defined regions. This allows for accurate modeling of the distribution of activity in VOIs, as opposed to simple mean-value measurements.

As shown in Figure 3.3, DVR values across regions were non-normal, and were fit well by an admixture of two normal distributions. It should be noted that as the VOIs used for measurement in this case were combined with gray-matter masks of each individual subject, this admixture distribution is likely not a result of heterogeneity in binding between white and grey matter. Instead, this is representative of the known heterogeneous nature of amyloid and tau protein deposition within cortical regions in AD and other dementias: some regions mostly devoid of protein aggregates (modeled by $N(\mu_1, \sigma_1)$), and regions infiltrated by the disease (modeled by $N(\mu_2, \sigma_2)$). Additionally, as can be seen in Figure 3.3, much information about the pathological progression of the disease can be lost when using only mean-value measurements.

We found that although distributions of FDDNP-SUVr values were also non-normal and could be fit by a bi-normal admixture, there was actually a decrease in measured activity in a large proportion of subjects. Previous studies have also shown longitudinal reductions in SUVr measures in PiB, possibly indicating that SUVr measures are insufficient to fully capture longitudinal changes in amyloid burden [32].

Also in alignment with previous studies is our finding of negative correlation of the rate of disease progression with baseline amyloid burden, providing evidence of a plateauing effect of tau and amyloid deposition.

As shown in Tables 3.1and 3.2, models predicting the progression of AD pathology show large improvements when switching from mean-value measures to distribution-value measures. This is particularly noticeable in the case of Logan-DVR, where mean adjusted-R^2 of the best OLS models is only 0.30. The inability of mean-value DVR measures to predict longitudinal changes in amyloid load may explain the under-performance of FDDNP in previous longitudinal studies [3]. Tables 3.1 and 3.2 also show a marked improvement of predictive ability in using RE-based DVR values in place of Logan graphical analysis. This improvement is further shown in that PLS models using Logan based measures used an average of 10.1 ± 4.1 predictors across 3 latent variables, while PLS models using RE-based measures used only 7.1 ± 1.6 predictors across 3 latent variables. Furthermore, paired-difference tests show a significant improvement of RE over Logan in OLS model strength for controls ($p = 0.0014$), and significant improvement in PLS models for MCIs ($p=0.005$). There was a strong, but not significant ($p=0.053$) improvement in OLS models for MCIs, and PLS models in controls ($p=0.051$) when using RE instead of Logan-based DVR. This improvement is consistent with previous findings indicating improvements of RE-DVR over Logan-DVR in FDDNP [15]

A similar improvement is found in predicting longitudinal changes in psychological scores based on the initial scan, as shown in Tables 3.3 and 3.4. In the case of both Logan and RE-based DVR measures, models were greatly improved with the introduction of distribution data. Although RE-based models did not show a significant improvement over Logan-DVR models in control subjects, there was a significant improvement in both OLS ($p=0.003$) and PLS ($p=0.02$)

models for MCIs. The significant improvement in using distribution-value data, and in using RE-based DVR measures, may explain previous difficulties in using amyloid imaging agents to predict longitudinal changes in pathology and symptoms [3].

As shown above, use of voxel-value distribution can be a powerful tool in improving the quantitative utility of PET in evaluating diffuse bio-markers. In combination with automatic generation of large anatomically specific VOIs, this methodology allows for increased signal-to-noise measurement of tracer activity across multiple subjects. This increase could be due to reductions in noise introduced through inter- or intra-investigator variability, small voxel-sample size, and non-normality of tracer activity. Given the known heterogeneous localization of amyloid and tau pathology in dementias, and the improvement shown in this work, it is likely that the predictive capability of imaging data in AD and other dementias could be greatly improved through the use of this method as well.

While subjects in this study were limited to healthy controls and MCI subjects, future studies of the methodology are warranted for studying changes over a longer time scale, as well as changes in FDDNP binding in subjects with more severe disease states such as amnestic-MCI and AD. Although this work has centered on the use of FDDNP in the context of dementia, its methods are easily adaptable to other tracers for AD, as well as to other disorders and diseases that show diffuse localization of target in tissue such as progressive supranuclear palsy [33], Down syndrome [34], or chronic traumatic encephalopathy [35]. In addition to improving the predictive capability of the imaging data, this method allows for more accurate measurement of disease pathology, and facilitates robust high-throughput image analysis, reducing many sources of noise.

3.5 Conclusions

We have shown that the use of voxel value distribution data is a powerful tool in increasing the quantitative strength of PET data in amyloid and tau imaging, by accounting for non-normal distributions of parametric values due to heterogeneous density of pathological bio-markers in tissue. Additionally, RE-DVR appears to be a more robust measure of amyloid binding than Logan-based graphical analysis for FDDNP. These results suggest that with a sample of subjects across a more diverse range of disease states, a more complete imaging-based model for disease staging and progression could be built. This method is applicable to studies involving other AD tracers that bind amyloid or tau, as well as other imaging studies with heterogeneous localization of tracer in tissue. Future studies are planned to compare the effect of this method in data already collected from subjects serially scanned with PiB and FDDNP.

Acknowledgments

We would like to thank Dr. Paul Thompson for his assistance with the cortical surface mapping technique, Dr. Avants of the University of Pennsylvania for the production of the ANTs package, Mr. David Truong and his group for the computational assistance, and Dr. Satyamurthy and the cyclotron facility for the production of FDDNP.

Financial Disclosure

The University of California, Los Angeles, owns a U.S. patent (6,274,119) entitled “Methods for Labeling β-Amyloid Plaques and Neurofibrillary Tangles,” that uses the approach outlined in this article. Drs. Small, Huang, and Barrio are among the inventors, have received royalties, and may receive royalties on future sales. Dr. Small reports having served as a consultant and/or having received lecture fees from Eisai, Forest, Medivation, Novartis, and Pfizer.

References

[1] Wilks MQ, Protas H, Wardak M, *et al*. Automated VOI Analysis in FDDNP PET Using Structural Warping: Validation through Classification of Alzheimer's Disease Patients. International Journal of Alzheimer's Disease 2012;2012.

[2] Protas HD, Huang S-C, Kepe V, *et al*. FDDNP binding using MR derived cortical surface maps. NeuroImage 2010;49:240-8.

[3] Ossenkoppele R, Tolboom N, Foster-Dingley JC, *et al*. Longitudinal imaging of Alzheimer pathology using [11C] PIB,[18F] FDDNP and [18F] FDG PET. European journal of nuclear medicine and molecular imaging 2012;39:990-1000.

[4] Braak H, Braak E. Neuropathological stageing of Alzheimer-related changes. Acta Neuropathologica 1991;82:239-59.

[5] Kepe V, Huang S-C, Small GW, Satyamurthy N, Barrio JR. Microstructural Imaging of Neurodegenerative Changes. In: Silverman D, ed. PET in the Evaluation of Alzheimer's Disease and Related Disorders. New York: Springer; 2009.

[6] Peterson RC, Parisi JE, Dickson DW, *et al*. Neuropathologic features of amnestic mild cognitive impairment. Archives of Neurology 2006;63:665-72.

[7] Price JL, Morris JC. Tangles and plaques in nondemented aging and "preclinical" Alzheimer's disease. Annals of Neurology 1999;45:358-68.

[8] Peterson RC. Mild cognitive impairment as a diagnostic entity. Journal of Internal Medicine 2004;256:183-94.

[9] Gauthier S, Reisberg B, Zaudig M, *et al*. Mild cognitive impairment. The Lancet 2006;367:1262-70.

[10] Mintun M, Larossa G, Sheline Y, *et al*. [11C] PIB in a nondemented population Potential antecedent marker of Alzheimer disease. Neurology 2006;67:446-52.

[11] Villemagne VL, Ong K, Mulligan RS, *et al*. Amyloid imaging with 18F-florbetaben in Alzheimer disease and other dementias. Journal of Nuclear Medicine 2011;52:1210-7.

[12] Maruyama M, Shimada H, Suhara T, *et al*. Imaging of tau pathology in a tauopathy mouse model and in Alzheimer patients compared to normal controls. Neuron 2013;79:1094-108.

[13] Logan J, Fowler JS, Volkow ND, Wang G-J, Ding Y-S, Alexoff DL. Distribution volume ratios without blood sampling from graphical analysis of PET data. Journal of Cerebral Blood Flow & Metabolism 1996;16:834-40.

[14] Zhou Y, Ye W, Brašić JR, Crabb AH, Hilton J, Wong DF. A consistent and efficient graphical analysis method to improve the quantification of reversible tracer binding in radioligand receptor dynamic PET studies. NeuroImage 2009;44:661-70.

[15] Wong K-P, Kepe V, Dahlbom M, *et al*. Comparative evaluation of Logan and relative-equilibrium graphical methods for parametric imaging of dynamic [^{18}F] FDDNP PET determinations. NeuroImage 2012;60:241-51.

[16] Wong, KP, Shin, J, Kepe, V, Bahlbom, M, Satyamurthy, N, Small, G, Barrio, J, Huang, SC, Simplified quantification of FDDNP PET studies, 58th Annual Meeting of the Society of Nucl. Medicine, San Antonio, Texas, June 4-8, 2011, J. Nucl. Med. 52(suppl), 2011 (abstract).

[17] Villain N, Chételat G, Grassiot B, *et al*. Regional dynamics of amyloid-β deposition in healthy elderly, mild cognitive impairment and Alzheimer's disease: a voxelwise PiB–PET longitudinal study. Brain 2012;135:2126-39.

[18] Landau SM, Mintun MA, Joshi AD, *et al*. Amyloid deposition, hypometabolism, and longitudinal cognitive decline. Annals of Neurology 2012;72:578-86.

[19] Small GW, Siddarth P, Burggren AC, *et al*. Influence of cognitive status, age, and APOE-4 genetic risk on brain FDDNP positron-emission tomography imaging in persons without dementia. Archives of general psychiatry 2009;66:81.

[20] Thompson PM, MacDonald D, Mega MS, Holmes CJ, Evans AC, Toga AW. Detection and mapping of abnormal brain structure with a probabilistic atlas of cortical surfaces. Journal of Computer Assisted Tomography 1997;21:567-81.

[21] Liu J, Kepe V, Zabjek A, *et al*. High-yield, automated radiosynthesis of 2-(1-{6-[(2-[18F]Fluoroethyl)(methyl)amino]-2-naphthyl}ethylidene)malononitrile ([18F]FDDNP) ready for animal or human administration Molecular Imaging and Biology 2007;9:6-16.

[22] M. Wardak, *et al*., "Movement correction method for human brain PET Images: application to quantitative analysis of dynamic F18-FDDNP scans," The Journal of Nuclear Medicine, vol. 51, pp. 210-218, 2010.

[23] K. P. Wong, *et al*., "Movement correction of [18F]FDDNP PET studies for brain amyloid imaging," in Nuclear Science Symposium Conference Record, 2007, pp. 3927-3977.

[24] Advanced Normalization Tools. 2011(Accessed at http://picsl.upenn.edu/ANTS).

[25] Avants BB, Epstein CL, Grossman M, Gee JC. Symmetric diffeomorphic image registration with cross-correlation: Evaluating automated labeling of elderly and neurodegenerative brain. Medical Image Analysis 2008;12:26-4.

[26] Joachim C, Morris J, Selkoe D. Diffuse senile plaques occur commonly in the cerebellum in Alzheimer's disease. The American journal of pathology 1989;135:309.

[27] Yamaguchi H, Hirai S, Morimatsu M, Shoji M, Nakazato Y. Diffuse type of senile plaques in the cerebellum of Alzheimer-type dementia demonstrated byβ protein immunostain. Acta Neuropathologica 1989;77:314-9.

[28] Wong K-P, Wardak M, Shao W, *et al*. Quantitative analysis of [18F]FDDNP PET using subcortical white matter as reference region. European journal of nuclear medicine and molecular imaging 2010;37:575-88.

[29] Dempster AP, Laird NM, Rubin DB. Maximum likelihood from incomplete data via the EM algorithm. *Journal of the Royal statistical Society.* 1977;39(1):1-38.

[30] Wold S. PLS for multivariate linear modeling. *Chemometric methods in molecular design.* 1995;2:195-218.

[31] The PLS Procedure: SAS/STAT 9.2 user's guide. Cary, NC: SAS Institute, 2008.

[32] Jack CR, Lowe VJ, Weigand SD, *et al*. Serial PIB and MRI in normal, mild cognitive impairment and Alzheimer's disease: implications for sequence of pathological events in Alzheimer's disease. Brain 2009;132:1355-65.

[33] Kepe V, Bordelon Y, Boxer A, *et al*. PET Imaging of Neuropathology in Tauopathies: Progressive Supranuclear Palsy. Journal of Alzheimer's Disease 2013;36:145-53.

[34] Nelson LD, Siddarth P, Kepe V, *et al*. Positron Emission Tomography of Brain {beta}-Amyloid and Tau Levels in Adults With Down Syndrome. Archives of Neurology 2011;68:768.

[35] McKee AC, Cantu RC, Nowinski CJ, *et al*. Chronic traumatic encephalopathy in athletes: progressive tauopathy following repetitive head injury. Journal of neuropathology and experimental neurology 2009;68:709.

Figures and Tables

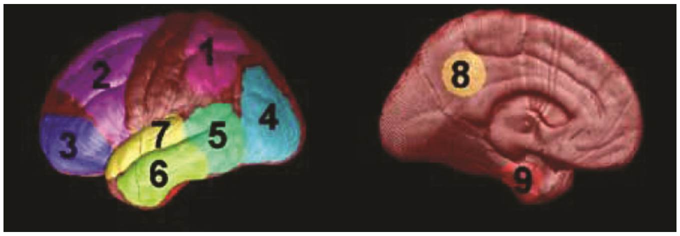

FIGURE 3.1. Illustration of cortical VOIs used in data extraction. Reprinted from Protas *et al.*2010 [2]

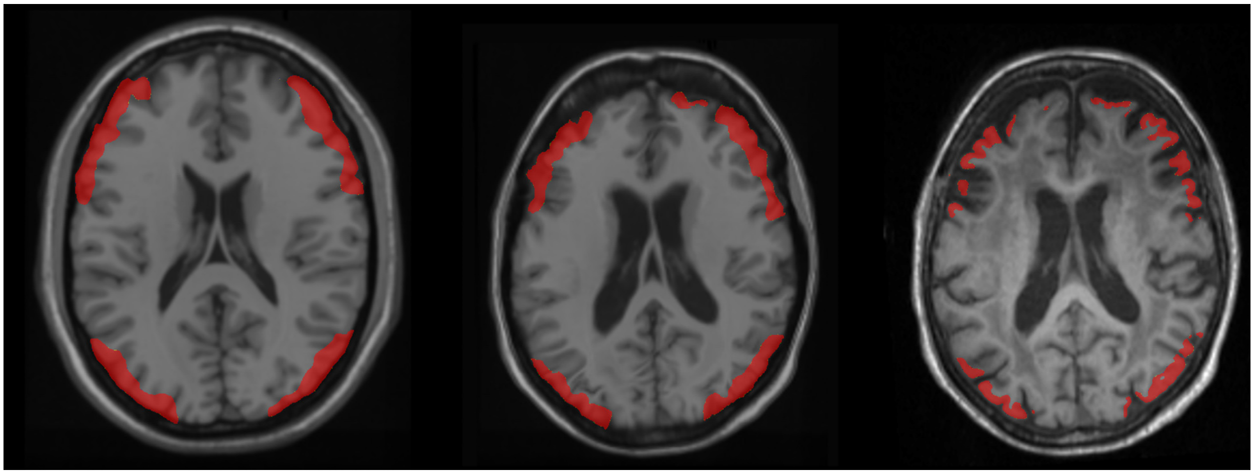

FIGURE 3.2. Example of automated registration of common space atlas and automated VOI generation in subject Space. (Left) Common space MRI with VOIs for posterior frontal lobe and occipital-parietal regions. (Center) Common space MRI and VOIs warped to subject space. (Right) Subject MRI with automatically generated VOIs composed with grey-matter segmentation.

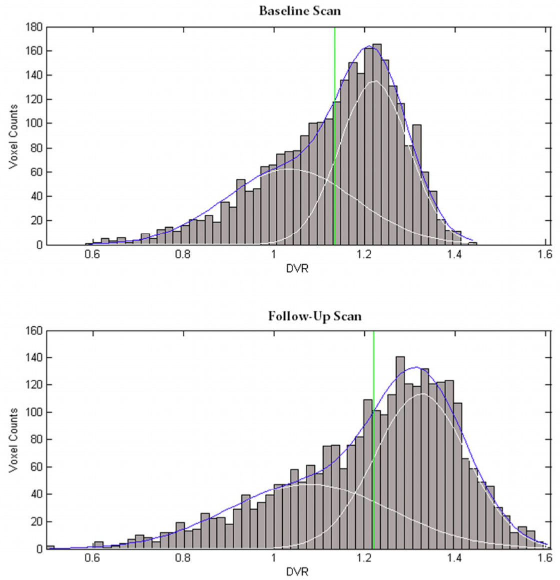

FIGURE 3.3. Distribution of voxel Logan-DVR values in frontal lobe for a single MCI subject at baseline and two-year follow-up. Grey bars show measured data. White shows fitted distributions for healthy and diseased tissue, and blue shows admixture distribution of whole VOI. The vertical green line shows the mean value of the VOI.

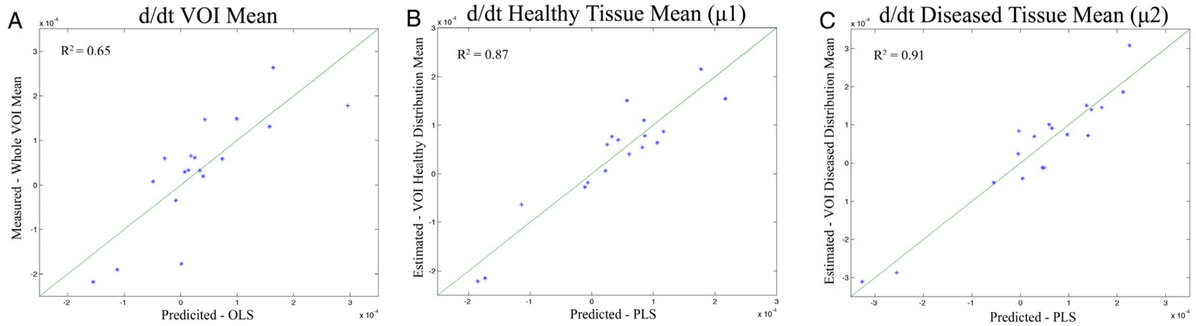

FIGURE 3.4. Scatter plots of measured (whole VOI Mean) or estimated (Admixture parameters) vs. predicted (From OLS or PLS) rates of change (units/day) in the occipital-parietal area of MCI subjects. (A) Rate of change in VOI mean using baseline VOI means as predictors. (B) Rate of change in healthy tissue mean (μ_1) using admixture parameters at baseline as predictors. (C) Rate of change in diseased tissue mean (μ_2) using admixture parameters at baseline as predictors. Specific predictors and regression coefficients can be found in Supplemental Data 1. The y=x line is shown in green.

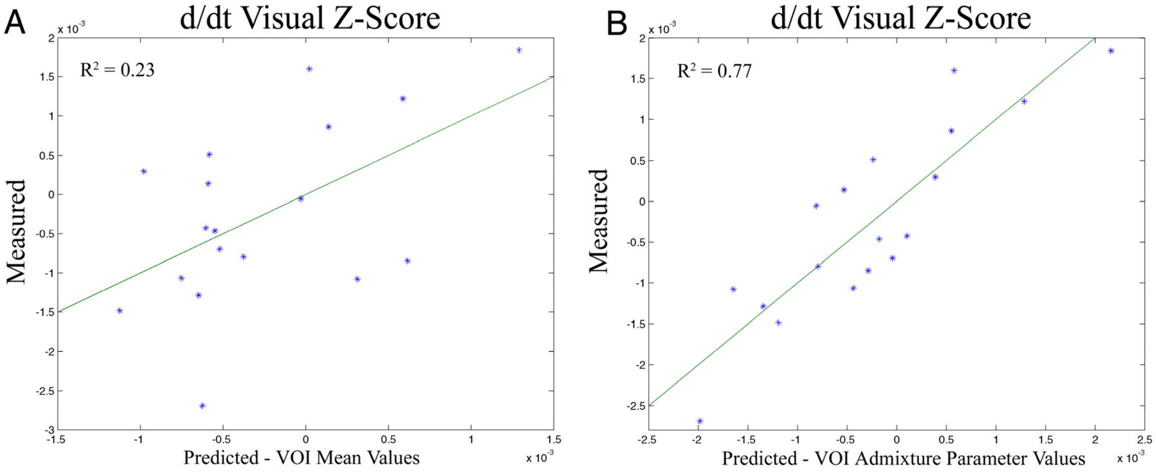

FIGURE 3.5. Scatter plots of measured vs. predicted rates of change (units/day) in the visual processing Z-score for MCI subjects. (A) Using mean RE-DVR measures from VOIs at the baseline scan as predictors. (B) Using admixture parameters from RE-DVR images at the baseline scan as predictors. Specific predictors and regression coefficients can be found in Supplemental Data 1. The y=x line is shown in green.

Table 3.1: Regression Results of Predicting Rate of Change in Logan-DVR by Initial Logan-DVR Values. Data shown are adjusted-R^2 (mean ± SD) of optimal models of parameters measured in each region.

Region	Control (adjusted-R^2)			MCI (adjusted-R^2)		
	Mean	Distribution (OLS)	Distribution (PLS*)	Mean	Distribution (OLS)	Distribution (PLS*)
Upper Parietal	0.32	0.65 ±.06	0.77 ± .06	0.34	0.64 ± .03	0.79 ± .05
Posterior Frontal	0.29	0.57±.11	0.74 ±.09	0.34	0.58 ±.13	0.69 ± .11
Prefrontal	0.23	0.68±.09	0.77 ±.08	0.32	0.65±.06	0.82 ± .06
Occipital-Parietal	0.20	0.51±.05	0.76 ± .08	0.35	0.66 ± .07	0.72 ±.04
Posterior Temporal	0.25	0.51±.02	0.77 ±.11	0.25	0.66 ± .08	0.79 ±.05
Lower Temporal	**	0.67±.08	0.75 ± .05	0.21	0.62 ± .20	0.72 ± .14
Upper Temporal	**	0.64 ±.13	0.83±.06	0.22	0.60 ±.22	0.75 ±.11
Posterior Cingulate	0.20	0.67±.10	0.80 ±.06	0.41	0.55 ±.11	0.68 ±.15
Medial Temporal	**	0.72±.09	0.80 ±.04	0.55	0.69 ± .10	0.81 ± .10

* For PLS models, data shown is percent-variance of dependant variables explained by the model.

** No significant model with adjusted-R^2 >0 was found.

Table 3.2: Regression Results of Predicting Rate of Change in RE-DVR by Initial RE-DVR Values. Data shown are adjusted-R^2 (mean ± SD) of optimal models of parameters measured in each region.

Region	Control (adjusted-R^2)			MCI (adjusted-R^2)		
	Mean	Distribution (OLS)	Distribution (PLS*)	Mean	Distribution (OLS)	Distribution (PLS*)
Upper Parietal	0.50	0.80 ± .04	0.87 ±.03	0.69	0.69 ± .08	0.88 ± .02
Posterior Frontal	0.71	0.72 ±.13	0.76 ±.08	0.64	0.74 ± .13	0.84 ± .09
Prefrontal	0.58	0.76 ±.06	0.85 ±.10	**	0.73 ± .05	0.89 ± .05
Occipital-Parietal	0.40	0.69 ± .12	0.74 ± .09	0.58	0.81 ± .01	0.88 ± .02
Posterior Temporal	0.72	0.64 ±.30	0.70 ±.25	0.68	0.58 ±.18	0.68 ±.14
Lower Temporal	0.41	0.72 ±.24	0.86 ±.05	0.55	0.65 ±.05	0.79 ± .05
Upper Temporal	0.58	0.85 ±.08	0.89 ±.03	0.59	0.68 ± .10	0.79 ± .11
Posterior Cingulate	0.43	0.70 ±.08	0.76 ±.05	0.52	0.59 ± .19	0.76±.07
Medial Temporal	0.31	0.85 ±.05	0.90 ±.03	0.32	0.73 ±.08	0.87 ±.03

* For PLS models, data shown is percent-variance of dependant variables explained by the model.

** No significant model with adjusted-R^2 >0 was found.

Table 3.3: Regression Results of Predicting Rate of Change in Psychological Z-Scores by Initial Logan-DVR values. Data shown are adjusted-R^2 of optimal models for each Z-score.

Z-Score	Control (adjusted-R^2)			MCI (adjusted-R^2)		
	Mean	Distribution (OLS)	Distribution (PLS*)	Mean	Distribution (OLS)	Distribution (PLS*)
Executive Function	0.46	0.86	0.87	**	0.62	0.71
Language	**	0.45	0.77	0.31	0.54	0.69
Visuo-spatial	0.40	0.85	0.86	0.19	0.57	0.72
Psychomotor	0.70	0.78	0.85	0.22	0.22	0.55
Neuropsychological	0.39	0.57	0.81	**	0.59	0.66
Memory	**	0.42	0.53	**	0.48	0.74

* For PLS models, data shown is percent-variance of dependant variables explained by the model.

** No significant model with adjusted-$R^2 > 0$ was found.

Table 3.4: Regression Results of Predicting Rate of Change in Psychological Z-Scores by Initial RE-DVR values. Data shown are adjusted-R^2 of optimal models for each Z-score.

Z-Score	Control (adjusted-R^2)			MCI (adjusted-R^2)		
	Mean	Distribution (OLS)	Distribution (PLS*)	Mean	Distribution (OLS)	Distribution (PLS*)
Executive Function	0.58	0.83	0.90	**	0.80	0.85
Language	0.30	0.64	0.70	0.24	0.60	0.69
Visuo-spatial	0.47	0.68	0.91	0.18	0.75	0.77
Psychomotor	0.62	0.76	0.84	0.22	0.48	0.60
Neuropsychological	0.39	0.69	0.82	**	0.72	0.79
Memory	**	0.44	0.69	**	0.60	0.79

* For PLS models, data shown is percent-variance of dependant variables explained by the model.

** No significant model with adjusted-$R^2 > 0$ was found.

Supplemental Data 1

S1.1 Admixture Distribution Modeling

We let $\vec{x}$ be an $nx1$ vector of the DVR values measured from each voxel within a single VOI. We treat each x_i as independent and identically distributed observation from a mixture of two normal densities, $Mix(\mu_1, \mu_2, \sigma_1^2, \sigma_2^2, p)$.

$$Mix(\mu_1, \mu_2, \sigma_1, \sigma_2, p) = (1 - p) * N_1(\mu_1, \sigma_1^2) + p * N_2(\mu_2, \sigma_2^2) \tag{S1.1}$$

The values for $\mu_1, \mu_2, \sigma_1^2, \sigma_2^2,$ and$p$ can be estimated iteratively through an EM algorithm. At the j^{th} iterative step, we first compute the posterior mixture probability ($M_{i,j}$) that each of the n observations (i.e. voxel measurements) $x_i(i \in [1, n])$ from a single VOI is drawn from the distribution N_2, based on the parameter estimates from the previous iterative step, or the initial parameter estimates (Eq. S1.2). The parameter estimates are then updated according to Eqs. S1.3. This process is repeated until convergence. For the work here, the EM algorithm was allowed to continue until the net-magnitude of parameter estimate change became less than 10^{-4}.

$$M_{i,j+1} = \frac{\frac{p_j}{\sqrt{2\pi\sigma_{2,j}^2}} \exp \frac{-(x_i - \mu_{2,j})^2}{2\sigma_{2,j}^2}}{\frac{1-p_j}{\sqrt{2\pi\sigma_{1,j}^2}} \exp \frac{-(x_i - \mu_{1,j})^2}{2\sigma_{1,j}^2} + \frac{p_j}{\sqrt{2\pi\sigma_{2,j}^2}} \exp \frac{-(x_i - \mu_{2,j})^2}{2\sigma_{2,j}^2}} \tag{S1.2}$$

$$p_{j+1} = \frac{1}{n} \sum_{i=1}^{n} M_{i,j+1} \tag{S1.3a}$$

$$\mu_{1,j+1} = \frac{\sum_{i=1}^{n} (1 - M_{i,j+1}) x_i}{\sum_{i=1}^{n} (1 - M_{i,j+1})} \tag{S1.3b}$$

$$\mu_{2,j+1} = \frac{\sum_{i=1}^{n} M_{i,j+1} x_i}{\sum_{i=1}^{n} M_{i,j+1}} \tag{S1.3c}$$

$$\sigma_{1,j+1}^2 = \frac{1}{\sum_{i=1}^{n} (1 - M_{i,j+1})} \sum_{i=1}^{n} (1 - M_{i,j+1})(x_i - \mu_{1,j+1})^2 \tag{S1.3d}$$

$$\sigma^2_{2,j+1} = \frac{1}{\sum_{i=1}^{n} M_{i,j+1}} \sum_{i=1}^{n} M_{i,j+1}(x_i - \mu_{2,j+1})^2 \tag{S1.3e}$$

Because it is know that the EM algorithm for normal admixtures can result in noisy estimates (especially without constraints on the relationship between σ_1^2 and σ_2^2), bootstrapping was employed to obtain approximations of the variance of each parameter estimate. For each subject and VOI, the EM algorithm employed in Equations (S1.2, S1.3) was applied to 1000 bootstrap samples $\hat{\vec{x}}$ of the originally measured data, $\vec{x}$. The sample relative standard deviation (RSD) of each parameter was computed from the bootstrapping results. These estimated RSDs are shown in Table S1.1. Because the distribution of RSDs was highly non-normal in all cases, data shown in Table S1.1 are the median and median absolute deviation (MAD) of the parameter estimates.

S1.2 Regression Modeling

From each of the nine VOIs in which we measure the voxel distribution $\vec{x_v}$ ($v \in [1, 2, ..., 9]$), we derive four parameters at both the initial (t_1) and follow-up (t_2) scan, to be used in the regression modeling. Along with the means and admixture percentage obtained from the EM algorithm above ($\mu_{1,v}(t), \mu_{2,v}(t), p_v(t)$), we also have the whole-VOI mean, $\bar{x}_v(t)$. We calculate the rate of change (in days^{-1}) in these parameters over time as in Equation (S1.4). We then build regression models of the types described in Equations (S1.5) and (S1.6) for each VOI v. In Equation (S1.5), the rows of the independent data matrix X_v are a combination of up to three of parameters drawn from $\{\bar{x}_v | \forall v\}$. In Equations (S1.6), the rows of the independent data matrix P_v are a combination of up to three parameters drawn from $\{\mu_{1,v}, \mu_{2,v}, p_v | \forall v\}$.

$$\frac{d}{dt}\mu_{1,v} = \frac{\mu_{1,v}(t_2) - \mu_{1,v}(t_1)}{t_2 - t_1} \tag{S1.4}$$

$$\frac{d}{dt}\bar{x}_i = b_0 + X_v\vec{b} + \epsilon \tag{S1.5}$$

$$
\begin{aligned}
\frac{d}{dt}\mu_{1,i} &= b_0 + P_v\vec{b} + \epsilon \\
\frac{d}{dt}\mu_{2,i} &= b_0 + P_v\vec{b} + \epsilon \\
\frac{d}{dt}p_i &= b_0 + P_v\vec{b} + \epsilon
\end{aligned}
\tag{S1.6}
$$

The regressions computed in Eq. (S1.6) are complicated by the addition of measurement error as introduced through EM parameter estimation. With a median RSD of less than 1 percent, the measurement error in the parameters μ_1 and μ_2 are likely smaller than the error introduced by biological noise and PET reconstruction. For these parameters error in measurement is not likely to cause large deleterious effects in the linear regression. The larger relative error in the admixture parameter p will result in regression coefficients biased towards zero (when p is a independent variable) and larger standard errors in the estimated regression coefficients (when p is the dependant variable). However, both of these limitations will yield more conservative regression results than in a situation free of measurement error. The effects of the measurement error in p will be complicated further by the possibility of correlated measurement error in the the dependant in independent variables (e.g. when p_i is one of the predictors of $\frac{d}{dt}p_i$). These complications can all be overcome fairly easily with the use of partial least squares (PLS) regression, however. Because PLS regression models the covariance structure of the independent and dependent variables, and does not assume that they are independent, correlated and uncorrelated errors in measurement are robustly handled.

S1.3 Regression Modeling Results

The results from the regression modeling described above are reported in Tables S1.2-S1.13. Table S1.2 Shows regression results for models of $\frac{d}{dt}\bar{x}_i$ as described in Eq S1.5, using VOI means at the initial scan to predict rates of change in VOI means between scans. These table show results for controls and MCIs, using both Logan and RE-DVR measures. Data shown is adjusted-R^2, R^2, predictor variables (x_1, x_2, x_3), and their associated regression parameters (b_1, b_2, b_3) of the optimal model found. Models with no b_0 reported were built without a y-intercept parameter.

Tables S1.3 - S1.6 show regression results using models of sort in Eqs. S1.6, using estimated admixture parameters from the baseline scan as predictors for the rate of change in admixture parameters for controls and MCIs. Tables S1.3 and S1.4 show results using Logan DVR values, and Tables S1.5 and S1.6 show results using RE-DVR values. Data shown is adjusted-R^2, R^2, predictor variables (x_1, x_2, x_3), and their associated regression parameters (b_1, b_2, b_3) of the optimal model found. Models with no b_0 reported were built without a y-intercept parameter.

Tables S1.7 - S1.10 show PLS regression results using Logan and relative equilibrium DVR values, to predict the rate of change in estimated admixture parameters for controls and MCIs. Data shown is percent variance of the dependant variables explained by the model (R^2), the number of latent variables (LVs), and which predictor variables were used. Data shown as $\text{param}_{\{a,b,c,...\}}$, refers to the admixture parameter "param" as estimated for the VOIs a,b,c,... .

Table S1.11 Shows regression results for models described in Eq S1.5, using VOI means at the initial scan to predict rates of change in psychological Z-scores between examinations. These table show results for controls and MCIs, using both Logan and RE-DVR measures. Data shown is adjusted-R^2, R^2, predictor variables (x_1, x_2, x_3), and their associated regression parameters (b_1, b_2, b_3) of the optimal model found. Models with no b_0 reported were built without a y-intercept parameter.

Table S1.12 shows regression results using models of sort in Eqs. S1.6, using estimated admixture parameters (of Logan and RE-DVR images) from the baseline scan as predictors for the rate of change of psychological z-scores in controls and MCIs. Data shown is adjusted-R^2, R^2, predictor variables (x_1, x_2, x_3), and their associated regression parameters (b_1, b_2, b_3) of the optimal model found. Models with no b_0 reported were built without a y-intercept parameter.

Table S1.13 shows PLS regression results using Logan and relative equilibrium DVR values, to predict the rate of change in psychological z-scores. Data shown is percent variance of the dependant variables explained by the model (R^2), the number of latent variables (LVs), and which predictor variables were used. Data shown as $\text{param}_{\{a,b,c,...\}}$, refers to the admixture parameter "param" as estimated for the VOIs a,b,c,... .

Table S1.1 Median and Median Absolute Deviation of EM Parameter Estimates. (Data shown are percent values)

	Logan DVR				RE DVR			
	Controls		MCIs		Controls		MCIs	
	Median	MAD	Median	MAD	Median	MAD	Median	MAD
RSD(μ)	0.813	0.372	0.888	0.430	0.786	0.395	0.891	0.436
RSD(p)	10.0	4.60	11.1	5.17	10.0	4.55	12.1	5.65
RSD(σ^2)	9.65	3.83	10.6	4.54	9.84	4.14	10.4	4.32

Table S1.2: OLS Regression Model Details: Rates of change in the mean Logan (A) or relative equilibrium (B) DVR measured in nine VOIs in Controls and MCIs. NA values represent VOIs in which no model with regression parameters significantly different from zero could be found.

(A) d/dt Logan-DVR	Controls								
	Adj-R^2	R^2	x_1	x_2	x_3	b_0	b_1	b_2	b_3
(1) Upper Parietal	0.315	0.361	$\bar{x}_3$	-	-	1.0x10^{-3}	-8.6x10^{-4}	-	-
(2) Posterior Frontal	0.294	0.341	$\bar{x}_3$	-	-	1.1x10^{-3}	-9.6x10^{-4}	-	-
(3) Prefrontal	0.228	0.279	$\bar{x}_4$	-	-	1.7x10^{-3}	-1.5x10^{-3}	-	-
(4) Occipital-Parietal	0.203	0.256	$\bar{x}_3$	-	-	8.4x10^{-4}	-6.9x10^{-4}	-	-
(5) Posterior Temporal	0.253	0.303	$\bar{x}_6$	-	-	2.0x10^{-3}	-1.6x10^{-3}	-	-
(6) Lower Temporal	NA	NA	-	-	-	-	-	-	-
(7) Upper Temporal	NA	NA	-	-	-	-	-	-	-
(8) Posterior Cingulate	0.200	0.252	$\bar{x}_8$	-	-	1.5x10^{-3}	-1.2x10^{-3}	-	-
(9) Medial Temporal	NA	NA	-	-	-	-	-	-	-
	MCIs								
	Adj-R^2	R^2	x_1	x_2	x_3	b_0	b_1	b_2	b_3
(1) Upper Parietal	0.336	0.375	$\bar{x}_4$	-	-	1.3x10^{-3}	-1.1x10^{-3}	-	-
(2) Posterior Frontal	0.339	0.455	$\bar{x}_8$	-	-	1.5x10^{-3}	-1.2x10^{-3}	-	-
(3) Prefrontal	0.323	0.363	$\bar{x}_8$	-	-	1.4x10^{-3}	-1.1x10^{-3}	-	-
(4) Occipital-Parietal	0.353	0.391	$\bar{x}_4$	-	-	1.7x10^{-3}	-1.5x10^{-3}	-	-
(5) Posterior Temporal	0.205	0.252	$\bar{x}_4$	-	-	1.7x10^{-3}	-1.4x10^{-3}	-	-
(6) Lower Temporal	0.120	0.247	$\bar{x}_2$	-	-	1.7x10^{-3}	-1.5x10^{-3}	-	-
(7) Upper Temporal	0.223	0.272	$\bar{x}_2$	-	-	1.2x10^{-3}	-1.0x10^{-3}	-	-
(8) Posterior Cingulate	0.413	0.520	$\bar{x}_3$	$\bar{x}_8$	$\bar{x}_9$	1.5x10^{-3}	2.2x10^{-3}	-2.1x10^{-3}	-1.2x10^{-3}
(9) Medial Temporal	0.548	0.628	$\bar{x}_1$	$\bar{x}_3$	$\bar{x}_9$	1.7x10^{-3}	-2.6x10^{-3}	3.0x10^{-3}	-2.0x10^{-3}

(B) d/dt RE-DVR	Controls								
	Adj-R^2	R^2	x_1	x_2	x_3	b_0	b_1	b_2	b_3
(1) Upper Parietal	0.498	0.531	$\bar{x}_1$	-	-	8.9x10^{-4}	-8.7x10^{-3}	-	-
(2) Posterior Frontal	0.707	0.765	$\bar{x}_4$	$\bar{x}_5$	$\bar{x}_8$	1.7x10^{-3}	-2.2x10^{-3}	1.8x10^{-3}	-1.3x10^{-3}
(3) Prefrontal	0.584	0.667	$\bar{x}_4$	$\bar{x}_5$	$\bar{x}_8$	2.5x10^{-3}	-4.4x10^{-3}	3.1x10^{-3}	-1.2x10^{-3}
(4) Occipital-Parietal	0.403	0.522	$\bar{x}_1$	$\bar{x}_2$	$\bar{x}_7$	9.3x10^{-4}	1.4-x10^{-3}	1.8x10^{-3}	-1.3x10^{-3}
(5) Posterior Temporal	0.719	0.775	$\bar{x}_1$	$\bar{x}_2$	$\bar{x}_6$	1.9x10^{-3}	-1.3x10^{-3}	1.7x10^{-3}	-2.1x10^{-3}
(6) Lower Temporal	0.406	0.446	$\bar{x}_6$	-	-	1.6x10^{-3}	-1.5x10^{-3}	-	-
(7) Upper Temporal	0.582	0.666	$\bar{x}_4$	$\bar{x}_5$	$\bar{x}_8$	2.0x10^{-3}	-3.2x10^{-3}	2.4x10^{-3}	-1.2x10^{-3}
(8) Posterior Cingulate	0.426	0.464	$\bar{x}_8$	-	-	1.3x10^{-3}	-1.2x10^{-3}	-	-
(9) Medial Temporal	0.312	0.450	$\bar{x}_4$	$\bar{x}_5$	$\bar{x}_8$	2.6x10^{-3}	-5.1x10^{-3}	4.4x10^{-3}	-1.9x10^{-3}
	MCIs								
	Adj-R^2	R^2	x_1	x_2	x_3	b_0	b_1	b_2	b_3
(1) Upper Parietal	0.688	0.743	$\bar{x}_3$	$\bar{x}_7$	$\bar{x}_8$	1.9x10^{-3}	1.2x10^{-3}	-1.4x10^{-3}	-1.4x10^{-3}
(2) Posterior Frontal	0.637	0.573	$\bar{x}_3$	$\bar{x}_7$	$\bar{x}_8$	1.9x10^{-3}	1.2x10^{-3}	-1.6x10^{-3}	-1.3x10^{-3}
(3) Prefrontal	NA	NA	-	-	-	-	-	-	-
(4) Occipital-Parietal	0.575	0.650	$\bar{x}_3$	$\bar{x}_7$	$\bar{x}_8$	2.1x10^{-3}	1.4x10^{-3}	-2.0x10^{-3}	-1.2x10^{-3}
(5) Posterior Temporal	0.680	0.737	$\bar{x}_3$	$\bar{x}_7$	$\bar{x}_8$	2.0x10^{-3}	1.6x10^{-3}	-1.7x10^{-3}	-1.6x10^{-3}
(6) Lower Temporal	0.550	0.629	$\bar{x}_3$	$\bar{x}_7$	$\bar{x}_8$	2.0x10^{-3}	1.3x10^{-3}	-1.8x10^{-3}	-1.2x10^{-3}
(7) Upper Temporal	0.594	0.666	$\bar{x}_3$	$\bar{x}_7$	$\bar{x}_8$	1.7x10^{-3}	1.1x10^{-3}	-1.6x10^{-3}	-1.1x10^{-3}
(8) Posterior Cingulate	0.518	0.603	$\bar{x}_3$	$\bar{x}_4$	$\bar{x}_8$	1.1x10^{-3}	1.4x10^{-3}	-1.1x10^{-3}	-1.2x10^{-3}
(9) Medial Temporal	0.318	0.358	$\bar{x}_7$	-	-	1.9x10^{-3}	-1.7x10^{-3}	-	-

Table S1.3: Logan-DVR OLS Regression Model Details: Rates of change in the admixture parameters μ_1 (A), μ_2 (B), and p (C), estimated from Logan-DVR images across nine VOIs in Controls.

(A) d/dt μ_1	Controls								
	Adj-R^2	R^2	x_1	x_2	x_3	b_0	b_1	b_2	b_3
(1) Upper Parietal	0.698	0.759	$\mu_{1,3}$	$\mu_{2,7}$	p_9	-2.0x10^{-4}	9.4x10^{-4}	3.3x10^{-4}	-9.7x10^{-4}
(2) Posterior Frontal	0.619	0.695	$\mu_{1,4}$	p_2	p_4	3.1x10^{-4}	-8.9x10^{-4}	6.0x10^{-4}	6.0x10^{-4}
(3) Prefrontal	0.676	0.741	$\mu_{1,3}$	$\mu_{2,3}$	$\mu_{2,8}$	-8.4x10^{-4}	-4.0x10^{-3}	2.9x10^{-3}	1.3x10^{-3}
(4) Occipital-Parietal	0.562	0.649	$\mu_{1,7}$	$\mu_{2,2}$	$\mu_{2,3}$	5.8x10^{-4}	-2.0x10^{-3}	3.1x10^{-3}	-1.6x10^{-3}
(5) Posterior Temporal	0.666	0.733	$\mu_{1,3}$	$\mu_{2,2}$	p_9	1.5x10^{-4}	-1.9x10^{-3}	1.5x10^{-3}	3.5x10^{-4}
(6) Lower Temporal	0.634	0.707	$\mu_{1,3}$	$\mu_{2,1}$	p_2	-5.9x10^{-4}	-3.4x10^{-3}	3.1x10^{-3}	1.1x10^{-3}
(7) Upper Temporal	0.766	0.813	$\mu_{1,3}$	$\mu_{1,9}$	$\mu_{2,5}$	8.6x10^{-4}	-1.4x10^{-3}	-9.6x10^{-4}	1.3x10^{-3}
(8) Posterior Cingulate	0.610	0.688	$\mu_{1,3}$	$\mu_{2,1}$	p_2	-6.0x10^{-4}	-3.1x10^{-3}	2.9x10^{-3}	9.5x10^{-4}
(9) Medial Temporal	0.818	0.842	$\mu_{1,9}$	p_3	-	2.6x10^{-3}	-2.9x10^{-3}	6.5x10^{-4}	-

(B) d/dt μ_2									
	Adj-R^2	R^2	x_1	x_2	x_3	b_0	b_1	b_2	b_3
(1) Upper Parietal	0.659	0.727	p_3	p_9	$\mu_{2,7}$	1.5x10^{-4}	-6.6x10^{-4}	1.8x10^{-3}	-1.4x10^{-3}
(2) Posterior Frontal	0.643	0.715	$\mu_{1,3}$	$\mu_{2,3}$	p_2	3.9x10^{-4}	-2.1x10^{-3}	1.5x10^{-3}	3.2x10^{-4}
(3) Prefrontal	0.591	0.673	$\mu_{1,2}$	$\mu_{2,2}$	$\mu_{2,4}$	2.4x10^{-3}	-3.1x10^{-3}	4.4x10^{-3}	-3.7x10^{-3}
(4) Occipital-Parietal	0.460	0.568	$\mu_{1,2}$	$\mu_{2,2}$	$\mu_{2,4}$	2.2x10^{-3}	-2.9x10^{-3}	3.4x10^{-3}	-2.7x10^{-3}
(5) Posterior Temporal	0.650	0.720	$\mu_{1,2}$	$\mu_{2,2}$	$\mu_{2,4}$	2.9x10^{-3}	-3.3x10^{-3}	4.0x10^{-3}	-3.6x10^{-3}
(6) Lower Temporal	0.525	0.620	$\mu_{1,4}$	p_3	p_5	2.1x10^{-3}	-1.8x10^{-3}	8.0x10^{-3}	-9.5x10^{-4}
(7) Upper Temporal	0.516	0.613	$\mu_{1,1}$	$\mu_{1,3}$	p_5	4.1x10^{-4}	1.8x10^{-3}	-1.8x10^{-3}	-4.7x10^{-4}
(8) Posterior Cingulate	0.622	0.698	$\mu_{1,2}$	$\mu_{1,9}$	$\mu_{2,2}$	1.8x10^{-3}	-3.0x10^{-3}	-1.0x10^{-3}	2.1x10^{-3}
(9) Medial Temporal	0.651	0.721	$\mu_{1,9}$	p_3	p_4	2.3x10^{-3}	-2.0x10^{-3}	5.7x10^{-4}	-9.0x10^{-4}

(C) d/dt p									
	Adj-R^2	R^2	x_1	x_2	x_3	b_0	b_1	b_2	b_3
(1) Upper Parietal	0.584	0.668	$\mu_{2,1}$	$\mu_{2,7}$	p_9	1.2x10^{-3}	2.9x10^{-3}	-3.6x10^{-3}	-7.4x10^{-4}
(2) Posterior Frontal	0.437	0.549	$\mu_{1,7}$	$\mu_{2,6}$	p_7	-2.8x10^{-4}	-3.4x10^{-3}	3.8x10^{-3}	-8.0x10^{-4}
(3) Prefrontal	0.771	0.801	p_3	p_4	-	1.4x10^{-4}	-1.5x10^{-3}	1.2x10^{-3}	-
(4) Occipital-Parietal	0.508	0.606	$\mu_{2,3}$	$\mu_{2,7}$	p_7	-6.2x10^{-4}	-1.5x10^{-3}	2.4x10^{-3}	-7.5x10^{-4}
(5) Posterior Temporal	0.682	0.746	$\mu_{1,3}$	$\mu_{1,7}$	p_8	3.1x10^{-3}	1.9x10^{-3}	-4.1x10^{-3}	-1.0x10^{-3}
(6) Lower Temporal	0.691	0.732	p_5	p_7	-	1.6x10^{-3}	-9.1x10^{-4}	-1.9x10^{-3}	-
(7) Upper Temporal	0.649	0.719	$\mu_{1,7}$	$\mu_{2,7}$	p_9	-6.6x10^{-4}	4.6x10^{-3}	-3.4x10^{-3}	-6.9x10^{-4}
(8) Posterior Cingulate	0.784	0.827	$\mu_{1,1}$	$\mu_{2,5}$	p_8	1.6x10^{-3}	-5.2x10^{-3}	4.0x10^{-3}	-2.1x10^{-3}
(9) Medial Temporal	0.680	0.744	$\mu_{1,9}$	$\mu_{2,2}$	$\mu_{2,7}$	-3.1x10^{-3}	4.1x10^{-3}	4.6x10^{-3}	-5.1x10^{-3}

Table S1.4: Logan-DVR OLS Regression Model Details: Rates of change in the admixture parameters μ_1 (A), μ_2 (B), and p (C), estimated from Logan-DVR images across nine VOIs in MCI subjects.

(A) d/dt μ_1	MCIs								
	Adj-R^2	R^2	x_1	x_2	x_3	b_0	b_1	b_2	b_3
(1) Upper Parietal	0.622	0.689	$\mu_{1,1}$	p_2	p_5	$1.8x10^{-3}$	$-1.2x10^{-3}$	$-4.2x10^{-4}$	$-4.2x10^{-4}$
(2) Posterior Frontal	0.425	0.526	$\mu_{2,9}$	p_3	p_6	$7.4x10^{-4}$	$-4.6x10^{-4}$	$4.3x10^{-4}$	$-4.2x10^{-4}$
(3) Prefrontal	0.648	0.689	$\mu_{1,7}$	$\mu_{2,1}$	p_3	-	$-1.5x10^{-3}$	$1.1x10^{-3}$	$8.4x10^{-4}$
(4) Occipital-Parietal	0.588	0.665	$\mu_{1,1}$	p_3	p_6	$1.4x10^{-3}$	$-1.2x10^{-3}$	$7.5x10^{-4}$	$-6.5x10^{-4}$
(5) Posterior Temporal	0.680	0.737	$\mu_{1,1}$	p_7	p_8	$3.7x10^{-3}$	$-2.6x10^{-3}$	$-9.0x10^{-4}$	$-7.6x10^{-4}$
(6) Lower Temporal	0.541	0.595	$\mu_{2,2}$	$\mu_{2,3}$	p_3	-	$-2.2x10^{-3}$	$1.7x10^{-3}$	$1.0x10^{-3}$
(7) Upper Temporal	0.612	0.680	$\mu_{2,2}$	p_3	p_6	$1.3x10^{-3}$	$-1.0x10^{-3}$	$6.8x10^{-4}$	$-5.9x10^{-4}$
(8) Posterior Cingulate	0.615	0.695	$\mu_{2,2}$	p_3	p_6	$6.9x10^{-4}$	$-5.9x10^{-4}$	$6.7x10^{-4}$	$-3.9x10^{-4}$
(9) Medial Temporal	0.691	0.727	p_3	p_6	-	$1.2x10^{-3}$	$-1.7x10^{-3}$	$1.2x10^{-3}$	-
(B) d/dt μ_2									
	Adj-R^2	R^2	x_1	x_2	x_3	b_0	b_1	b_2	b_3
(1) Upper Parietal	0.632	0.697	$\mu_{2,4}$	$\mu_{2,5}$	p_6	$1.1x10^{-3}$	$-3.5x10^{-3}$	$2.8x10^{-3}$	$-4.8x10^{-4}$
(2) Posterior Frontal	0.647	0.709	$\mu_{2,4}$	$\mu_{2,5}$	p_6	$1.5x10^{-3}$	$-4.5x10^{-3}$	$3.6x10^{-3}$	$-5.9x10^{-4}$
(3) Prefrontal	0.597	0.668	$\mu_{2,4}$	$\mu_{2,5}$	p_6	$1.5x10^{-3}$	$-4.4x10^{-3}$	$3.4x10^{-3}$	$-4.5x10^{-4}$
(4) Occipital-Parietal	0.725	0.774	$\mu_{2,4}$	$\mu_{2,5}$	p_6	$2.1x10^{-3}$	$-5.4x10^{-3}$	$4.1x10^{-3}$	$-8.2x10^{-4}$
(5) Posterior Temporal	0.577	0.652	$\mu_{2,4}$	$\mu_{2,5}$	p_6	$1.6x10^{-3}$	$-2.7x10^{-3}$	$1.7x10^{-3}$	$-6.8x10^{-4}$
(6) Lower Temporal	0.473	0.566	$\mu_{2,4}$	$\mu_{2,5}$	p_6	$9.8x10^{-4}$	$-3.3x10^{-3}$	$2.8x10^{-3}$	$-5.0x10^{-4}$
(7) Upper Temporal	0.376	0.486	$\mu_{2,4}$	$\mu_{2,5}$	p_6	$9.9x10^{-4}$	$-2.5x10^{-3}$	$2.0x10^{-3}$	$-4.5x10^{-4}$
(8) Posterior Cingulate	0.602	0.659	$\mu_{2,6}$	$\mu_{2,8}$	p_3	-	$9.9x10^{-4}$	$-1.2x10^{-3}$	$7.4x10^{-4}$
(9) Medial Temporal	0.785	0.823	$\mu_{1,9}$	p_3	p_5	$1.0x10^{-3}$	$9.7x10^{-4}$	$-5.5x10^{-4}$	$-1.1x10^{-3}$
(C) d/dt p									
	Adj-R^2	R^2	x_1	x_2	x_3	b_0	b_1	b_2	b_3
(1) Upper Parietal	0.670	0.728	$\mu_{1,1}$	$\mu_{2,3}$	$\mu_{2,4}$	$1.1x10^{-3}$	$-3.1x10^{-3}$	$3.8x10^{-3}$	$-2.1x10^{-3}$
(2) Posterior Frontal	0.657	0.697	$\mu_{1,7}$	$\mu_{2,2}$	$\mu_{2,3}$	-	$-1.6x10^{-3}$	$5.3x10^{-3}$	$-3.4x10^{-3}$
(3) Prefrontal	0.708	0.742	p_3	p_7	p_8	-	$-9.8x10^{-4}$	$4.0x10^{-4}$	$6.0x10^{-4}$
(4) Occipital-Parietal	0.674	0.732	$\mu_{2,3}$	p_8	p_9	$-8.9x10^{-4}$	$7.2x10^{-4}$	$4.3x10^{-4}$	$-3.8x10^{-4}$
(5) Posterior Temporal	0.732	0.763	$\mu_{2,3}$	$\mu_{2,3}$	p_5	-	$-2.7x10^{-3}$	$3.5x10^{-3}$	$-1.5x10^{-3}$
(6) Lower Temporal	0.851	0.877	$\mu_{1,4}$	p_6	p_8	$3.6x10^{-3}$	$-2.6x10^{-3}$	$-2.0x10^{-3}$	$5.2x10^{-4}$
(7) Upper Temporal	0.817	0.851	p_3	p_6	p_7	$-9.2x10^{-4}$	$1.5x10^{-3}$	$8.1x10^{-4}$	$-7.9x10^{-4}$
(8) Posterior Cingulate	0.420	0.455	$\mu_{2,1}$	p_8	-	-	$7.8x10^{-4}$	$-1.3x10^{-3}$	-
(9) Medial Temporal	0.585	0.658	$\mu_{1,1}$	$\mu_{2,9}$	p_7	$-3.1x10^{-3}$	$-3.9x10^{-3}$	$5.3x10^{-3}$	$1.1x10^{-3}$

Table S1.5: RE-DVR OLS Regression Model Details: Rates of change in the admixture parameters μ_1 (A), μ_2(B), and p (C), estimated from RE-DVR images across nine VOIs in Controls.

(A) d/dt μ_1	Controls								
	Adj-R^2	R^2	x_1	x_2	x_3	b_0	b_1	b_2	b_3
(1) Upper Parietal	0.769	0.815	$\mu_{1,7}$	$\mu_{2,4}$	$\mu_{2,8}$	$1.5x10^{-3}$	$1.4x10^{-3}$	$-1.8x10^{-3}$	$-8.0x10^{-4}$
(2) Posterior Frontal	0.602	0.655	$\mu_{1,1}$	p_2	p_3	-	$-3.2x10^{-4}$	$3.2x10^{-4}$	$2.1x10^{-4}$
(3) Prefrontal	0.693	0.755	$\mu_{1,4}$	p_6	p_8	$1.8x10^{-3}$	$-1.8x10^{-3}$	$-3.5x10^{-4}$	$2.1x10^{-4}$
(4) Occipital-Parietal	0.656	0.725	$\mu_{1,7}$	$\mu_{2,3}$	p_8	$-4.7x10^{-4}$	$8.5x10^{-4}$	$-5.5x10^{-4}$	$3.1x10^{-4}$
(5) Posterior Temporal	0.728	0.782	$\mu_{1,7}$	$\mu_{1,4}$	p_8	$9.6x10^{-4}$	$1.1x10^{-3}$	$-2.1x10^{-3}$	$4.8x10^{-4}$
(6) Lower Temporal	0.865	0.883	$\mu_{1,2}$	$\mu_{2,7}$	p_8	-	$1.8x10^{-3}$	$-1.7x10^{-3}$	$4.0x10^{-4}$
(7) Upper Temporal	0.762	0.810	$\mu_{2,2}$	$\mu_{2,4}$	p_8	$9.7x10^{-4}$	$1.1x10^{-3}$	$-2.0x10^{-3}$	$2.4x10^{-4}$
(8) Posterior Cingulate	0.778	0.808	$\mu_{1,5}$	$\mu_{2,1}$	p_8	-	$1.0x10^{-3}$	$-1.3x10^{-3}$	$5.5x10^{-4}$
(9) Medial Temporal	0.872	0.889	$\mu_{2,6}$	$\mu_{2,7}$	p_7	-	$5.5x10^{-3}$	$-6.0x10^{-3}$	$7.4x10^{-3}$
(B) d/dt μ_2	Adj-R^2	R^2	x_1	x_2	x_3	b_0	b_1	b_2	b_3
(1) Upper Parietal	0.781	0.824	$\mu_{2,1}$	$\mu_{2,2}$	$\mu_{2,8}$	$1.4x10^{-3}$	$-2.2x10^{-3}$	$1.6x10^{-3}$	$-6.7x10^{-4}$
(2) Posterior Frontal	0.860	0.888	$\mu_{1,1}$	$\mu_{1,9}$	p_9	$1.5x10^{-3}$	$-1.0x10^{-3}$	$-5.0x10^{-4}$	$-1.5x10^{-4}$
(3) Prefrontal	0.805	0.844	$\mu_{2,4}$	$\mu_{2,6}$	p_8	$1.1x10^{-3}$	$-4.1x10^{-3}$	$2.8x10^{-3}$	$3.9x10^{-4}$
(4) Occipital-Parietal	0.817	0.854	$\mu_{1,3}$	$\mu_{2,4}$	p_8	$2.6x10^{-3}$	$1.2x10^{-3}$	$-3.6x10^{-3}$	$2.3x10^{-4}$
(5) Posterior Temporal	0.890	0.912	$\mu_{1,3}$	$\mu_{2,4}$	p_8	$3.1x10^{-3}$	$1.2x10^{-3}$	$-3.9x10^{-3}$	$2.1x10^{-4}$
(6) Lower Temporal	0.856	0.884	$\mu_{2,2}$	$\mu_{2,4}$	p_8	$1.1x10^{-3}$	$1.5x10^{-3}$	$-2.5x10^{-3}$	$2.7x10^{-4}$
(7) Upper Temporal	0.893	0.914	$\mu_{1,3}$	$\mu_{2,4}$	p_7	$2.6x10^{-3}$	$1.0x10^{-3}$	$-3.5x10^{-3}$	$4.8x10^{-4}$
(8) Posterior Cingulate	0.615	0.666	$\mu_{2,6}$	$\mu_{2,7}$	p_8	-	$2.3x10^{-3}$	$-2.4x10^{-3}$	$2.5x10^{-4}$
(9) Medial Temporal	0.793	0.834	$\mu_{2,2}$	$\mu_{2,4}$	$\mu_{2,8}$	$4.8x10^{-3}$	$3.4x10^{-3}$	$-5.4x10^{-3}$	$-2.2x10^{-3}$
(C) d/dt p	Adj-R^2	R^2	x_1	x_2	x_3	b_0	b_1	b_2	b_3
(1) Upper Parietal	0.841	0.872	$\mu_{2,1}$	$\mu_{2,3}$	p_9	$-2.6x10^{-3}$	$9.6x10^{-3}$	$-6.9x10^{-3}$	$-6.0x10^{-4}$
(2) Posterior Frontal	0.692	0.733	$\mu_{2,3}$	$\mu_{2,4}$	p_1	-	$1.2x10^{-3}$	$-7.7x10^{-4}$	$-7.1x10^{-4}$
(3) Prefrontal	0.774	0.820	$\mu_{1,5}$	$\mu_{2,6}$	p_3	$4.0x10^{-3}$	$3.3x10^{-3}$	$-5.8x10^{-3}$	$-1.6x10^{-3}$
(4) Occipital-Parietal	0.594	0.648	$\mu_{2,5}$	$\mu_{2,8}$	p_1	-	$-1.1x10^{-3}$	$1.0x10^{-3}$	$2.5x10^{-4}$
(5) Posterior Temporal	0.304	0.397	$\mu_{1,6}$	$\mu_{2,4}$	p_6	-	$-3.1x10^{-3}$	$3.5x10^{-3}$	$-1.1x10^{-3}$
(6) Lower Temporal	0.449	0.560	$\mu_{2,3}$	$\mu_{2,5}$	p_2	$2.4x10^{-3}$	$4.4x10^{-3}$	$-6.1x10^{-3}$	$-9.4x10^{-4}$
(7) Upper Temporal	0.891	0.906	$\mu_{1,9}$	$\mu_{2,9}$	p_7	-	$-4.6x10^{-3}$	$4.5x10^{-3}$	$-1.3x10^{-3}$
(8) Posterior Cingulate	0.713	0.770	$\mu_{2,8}$	$\mu_{2,9}$	p_3	$-3.6x10^{-3}$	$6.3x10^{-3}$	$-2.4x10^{-3}$	$-1.4x10^{-3}$
(9) Medial Temporal	0.881	0.905	$\mu_{1,1}$	p_7	p_8	$-4.1x10^{-3}$	$4.9x10^{-3}$	$-2.1x10^{-3}$	$1.1x10^{-3}$

Table S1.6: RE-DVR OLS Regression Model Details: Rates of change in the admixture parameters μ_1 (A), μ_2(B), and p (C), estimated from RE-DVR images across nine VOIs in MCI subjects.

(A) d/dt μ_1	MCIs								
	Adj-R^2	R^2	x_1	x_2	x_3	b_0	b_1	b_2	b_3
(1) Upper Parietal	0.769	0.796	$\mu_{1,1}$	$\mu_{1,2}$	p_5	-	-1.8×10^{-3}	2.1×10^{-3}	-3.3×10^{-4}
(2) Posterior Frontal	0.607	0.676	$\mu_{1,4}$	p_3	p_5	1.0×10^{-3}	-4.9×10^{-4}	-4.2×10^{-4}	-3.7×10^{-4}
(3) Prefrontal	0.752	0.795	$\mu_{1,2}$	$\mu_{1,3}$	$\mu_{1,7}$	8.5×10^{-4}	1.4×10^{-3}	-9.6×10^{-4}	-1.2×10^{-3}
(4) Occipital-Parietal	0.820	0.850	$\mu_{1,4}$	$\mu_{2,9}$	$\mu_{1,5}$	7.8×10^{-4}	-1.3×10^{-3}	7.7×10^{-4}	-5.1×10^{-4}
(5) Posterior Temporal	0.685	0.741	$\mu_{2,8}$	p_3	p_9	1.2×10^{-3}	-6.4×10^{-4}	-4.8×10^{-4}	-2.6×10^{-4}
(6) Lower Temporal	0.704	0.756	$\mu_{1,1}$	p_5	p_6	1.0×10^{-3}	-7.3×10^{-4}	-6.0×10^{-4}	3.1×10^{-4}
(7) Upper Temporal	0.744	0.789	$\mu_{1,5}$	$\mu_{2,3}$	p_5	1.6×10^{-3}	-1.9×10^{-3}	8.0×10^{-4}	-7.7×10^{-4}
(8) Posterior Cingulate	0.680	0.718	$\mu_{1,2}$	$\mu_{2,2}$	p_8	-	2.3×10^{-3}	-2.2×10^{-3}	3.0×10^{-4}
(9) Medial Temporal	0.795	0.831	$\mu_{1,9}$	$\mu_{2,3}$	$\mu_{2,9}$	1.1×10^{-3}	-2.2×10^{-3}	-2.4×10^{-3}	3.3×10^{-3}
(B) d/dt μ_2									
	Adj-R^2	R^2	x_1	x_2	x_3	b_0	b_1	b_2	b_3
(1) Upper Parietal	0.677	0.734	$\mu_{1,8}$	$\mu_{2,4}$	$\mu_{2,5}$	8.0×10^{-4}	-8.1×10^{-4}	-2.2×10^{-3}	2.3×10^{-3}
(2) Posterior Frontal	0.859	0.884	$\mu_{2,4}$	$\mu_{2,5}$	p_5	8.2×10^{-4}	-2.7×10^{-3}	2.2×10^{-3}	-3.7×10^{-4}
(3) Prefrontal	0.770	0.811	$\mu_{1,4}$	p_5	p_9	1.4×10^{-3}	-8.1×10^{-4}	-5.2×10^{-4}	-2.8×10^{-4}
(4) Occipital-Parietal	0.811	0.844	$\mu_{1,4}$	$\mu_{1,9}$	p_5	1.6×10^{-3}	-1.6×10^{-3}	4.2×10^{-4}	-5.8×10^{-4}
(5) Posterior Temporal	0.680	0.736	$\mu_{1,4}$	p_5	p_9	1.3×10^{-3}	-8.1×10^{-4}	-4.0×10^{-4}	-2.7×10^{-4}
(6) Lower Temporal	0.610	0.656	$\mu_{1,8}$	p_5	-	1.4×10^{-3}	-9.7×10^{-4}	-5.0×10^{-4}	-
(7) Upper Temporal	0.575	0.650	$\mu_{1,2}$	$\mu_{1,5}$	p_5	1.2×10^{-3}	9.1×10^{-4}	-1.5×10^{-3}	-6.9×10^{-4}
(8) Posterior Cingulate	0.720	0.753	$\mu_{2,4}$	$\mu_{2,5}$	-	5.0×10^{-4}	-3.4×10^{-3}	2.9×10^{-3}	-
(9) Medial Temporal	0.741	0.787	p_3	p_5	p_6	4.9×10^{-4}	5.4×10^{-4}	-8.7×10^{-4}	-2.6×10^{-4}
(C) d/dt p									
	Adj-R^2	R^2	x_1	x_2	x_3	b_0	b_1	b_2	b_3
(1) Upper Parietal	0.618	0.663	$\mu_{1,6}$	$\mu_{1,7}$	p_9	-	3.8×10^{-3}	-3.3×10^{-3}	-6.6×10^{-4}
(2) Posterior Frontal	0.755	0.784	$\mu_{2,2}$	$\mu_{2,3}$	p_9	-	3.2×10^{-3}	-2.8×10^{-3}	-8.2×10^{-4}
(3) Prefrontal	0.677	0.734	$\mu_{1,3}$	$\mu_{2,2}$	$\mu_{2,5}$	1.2×10^{-3}	2.7×10^{-3}	-5.3×10^{-3}	1.7×10^{-3}
(4) Occipital-Parietal	0.806	0.840	$\mu_{1,1}$	$\mu_{1,3}$	p_4	1.1×10^{-3}	-1.1×10^{-3}	7.2×10^{-4}	-1.2×10^{-3}
(5) Posterior Temporal	0.378	0.414	$\mu_{1,2}$	p_5	-	-	8.2×10^{-4}	-1.3×10^{-3}	-
(6) Lower Temporal	0.637	0.659	$\mu_{1,7}$	p_6	-	-	1.1×10^{-3}	-2.0×10^{-3}	-
(7) Upper Temporal	0.730	0.761	$\mu_{1,7}$	$\mu_{2,3}$	p_7	-	4.1×10^{-3}	-3.3×10^{-3}	-1.3×10^{-3}
(8) Posterior Cingulate	0.369	0.406	$\mu_{1,8}$	p_5	-	-	1.5×10^{-3}	-2.2×10^{-3}	-
(9) Medial Temporal	0.644	0.707	$\mu_{1,8}$	$\mu_{2,3}$	$\mu_{2,9}$	5.6×10^{-3}	-7.4×10^{-3}	5.6×10^{-3}	-3.6×10^{-3}

Table S1.7: Logan-DVR PLS Regression Model Details: Rates of change in the admixture parameters μ_1 (A), μ_2 (B), and p (C), estimated from Logan-DVR images across nine VOIs in Controls. Predictors shown, ($x_{\{i,j,k,...\}}$) are the estimated parameter x from VOIs {i,j,k,...}. R^2 value shown is percent-variance of dependant variables explained by the model.

(A) d/dt μ_1	Controls		
	R^2	LVs	Predictors
(1) Upper Parietal	0.801	3	$\mu_{1,\{3,9\}},\ \mu_{2,\{7,8,9\}},\ p_{\{3,6,9\}}$
(2) Posterior Frontal	0.736	3	$\mu_{1,\{3,6\}},\ \mu_{2,\{3\}},\ p_{\{6\}}$
(3) Prefrontal	0.717	3	$\mu_{1,\{3,4,5,7\}},\ \mu_{2,\{2,3,4,5,6\}},\ p_{\{3,4,5,7\}}$
(4)Occipital-Parietal	0.760	3	$\mu_{1,\{2,3,7,8,9\}},\ \mu_{2,\{1,4,5,6,9\}},\ p_{\{2,4,8\}}$
(5) Posterior Temporal	0.714	3	$\mu_{1,\{3,5,9\}},\ \mu_{2,\{1,3,4,5,6\}},\ p_{\{3,8\}}$
(6) Lower Temporal	0.770	3	$\mu_{1,\{2,6,9\}},\ \mu_{2,\{1\}},\ p_{\{3,6,9\}}$
(7) Upper Temporal	0.890	3	$\mu_{1,\{3,7,9\}},\ \mu_{2,\{2,5,6,9\}},\ p_{\{4,9\}}$
(8) Posterior Cingulate	0.737	3	$\mu_{1,\{3,6,8\}},\ \mu_{2,\{6\}},\ p_{\{3,6,8,9\}}$
(9) Medial Temporal	0.837	3	$\mu_{1,\{6,9\}},\ \mu_{2,\{9\}},\ p_{\{6,7,9\}}$
(B) d/dt μ_2			
	R^2	LVs	Predictors
(1) Upper Parietal	0.813	3	$\mu_{1,\{1,3,7,9\}},\ \mu_{2,\{1,2,3,4,6,7,9\}},\ p_{\{3,9\}}$
(2) Posterior Frontal	0.836	2	$\mu_{1,\{1,2,3,4,9\}},\ \mu_{2,\{1,2,3,4,5,6,7\}},\ p_{\{3,4,5\}}$
(3) Prefrontal	0.719	3	$\mu_{1,\{3,4\}},\ \mu_{2,\{2\}},\ p_{\{4\}}$
(4)Occipital-Parietal	0.835	3	$\mu_{1,\{1,2,3,8,9\}},\ \mu_{2,\{1,2,4,5,6\}},\ p_{\{1,3,4,5\}}$
(5) Posterior Temporal	0.891	3	$\mu_{1,\{2,3,5,9\}},\ \mu_{2,\{2,3,4,5,6,7\}},\ p_{\{3,4\}}$
(6) Lower Temporal	0.781	3	$\mu_{1,\{2,3,9\}},\ \mu_{2,\{1,5,6,7\}},\ p_{\{4,5\}}$
(7) Upper Temporal	0.820	3	$\mu_{1,\{1,2,3,9\}},\ \mu_{2,\{2,7\}},\ p_{\{1,4,5\}}$
(8) Posterior Cingulate	0.812	3	$\mu_{1,\{2,3,8,9\}},\ \mu_{2,\{2,7,8\}},\ p_{\{5\}}$
(9) Medial Temporal	0.801	3	$\mu_{1,\{2,3,9\}},\ \mu_{2,\{1,2,5,6,9\}},\ p_{\{4,9\}}$
(C) d/dt p			
	R^2	LVs	Predictors
(1) Upper Parietal	0.701	3	$\mu_{1,\{9\}},\ \mu_{2,\{7,9\}},\ p_{\{1,2,4,6,9\}}$
(2) Posterior Frontal	0.648	3	$\mu_{1,\{7,9\}},\ \mu_{2,\{9\}},\ p_{\{1,2,4,7\}}$
(3) Prefrontal	0.859	3	$\mu_{1,\{9\}},\ p_{\{3,4,5,7\}}$
(4)Occipital-Parietal	0.678	3	$\mu_{1,\{4,9\}},\ p_{\{3,4,5,7\}}$
(5) Posterior Temporal	0.703	3	$\mu_{1,\{3,7\}},\ \mu_{2,\{8\}},\ p_{\{3,5,7,8\}}$
(6) Lower Temporal	0.686	2	$\mu_{1,\{9\}},\ p_{\{4,6,7,9\}}$
(7) Upper Temporal	0.777	2	$\mu_{1,\{7,8,9\}},\ \mu_{2,\{8,9\}},\ p_{\{4,5,6,7,9\}}$
(8) Posterior Cingulate	0.855	3	$\mu_{1,\{1,6\}},\ p_{\{3,5,6,8\}}$
(9) Medial Temporal	0.750	3	$\mu_{1,\{9\}},\ \mu_{2,\{1,9\}},\ p_{\{6,7,9\}}$

Table S1.8: Logan-DVR PLS Regression Model Details: Rates of change in the admixture parameters μ_1 (A), μ_2 (B), and p (C), estimated from Logan-DVR images across nine VOIs in MCI subjects. Predictors shown, ($x_{\{i,j,k,...\}}$) are the estimated parameter x from VOIs {i,j,k,...}. R^2 value shown is percent-variance of dependant variables explained by the model.

(A) d/dt μ_1	MCIs		
	R^2	LVs	Predictors
(1) Upper Parietal	0.839	3	$\mu_{1,\{3,4,5,7,8,9\}}$, $\mu_{2,\{3,4,5,7,8,9\}}$, $p_{\{2,3,5,9\}}$
(2) Posterior Frontal	0.577	3	$\mu_{1,\{1,2,3,5,7\}}$, $\mu_{2,\{1,2,3,8,9\}}$, $p_{\{3,6\}}$
(3) Prefrontal	0.749	3	$\mu_{1,\{1,3,4,7\}}$, $\mu_{2,\{1,3,9\}}$, $p_{\{2,3,5,9\}}$
(4)Occipital-Parietal	0.690	3	$\mu_{1,\{1,2,4,7,8\}}$, $\mu_{2,\{1,2,3,4,8\}}$, $p_{\{1,2\}}$
(5) Posterior Temporal	0.795	3	$\mu_{1,\{1,2,5,7,8\}}$, $\mu_{2,\{1,2,3,4,5,6,7,8,9\}}$, $p_{\{1,2,6,8\}}$
(6) Lower Temporal	0.610	3	$\mu_{1,\{6,7\}}$, $\mu_{2,\{2\}}$, $p_{\{9\}}$
(7) Upper Temporal	0.740	3	$\mu_{1,\{3,7,8\}}$, $\mu_{2,\{1,2,5,6,7\}}$, $p_{\{1\}}$
(8) Posterior Cingulate	0.720	3	$\mu_{1,\{1,2,3,8\}}$, $\mu_{2,\{3,4,8,9\}}$, $p_{\{2,3,5\}}$
(9) Medial Temporal	0.697	3	$\mu_{1,\{1,2,3,4,5,7,9\}}$, $\mu_{2,\{2,3,6,9\}}$, $p_{\{3\}}$
(B) d/dt μ_2			
	R^2	LVs	Predictors
(1) Upper Parietal	0.737	3	$\mu_{1,\{3,7\}}$, $\mu_{2,\{3,4,8\}}$, $p_{\{2,3,5,9\}}$
(2) Posterior Frontal	0.713	3	$\mu_{1,\{1,2,3,4,7\}}$, $\mu_{2,\{1,3,4,5,7,8,9\}}$, $p_{\{1,2,3,5,7,9\}}$
(3) Prefrontal	0.842	3	$\mu_{1,\{1,3,4,7\}}$, $\mu_{2,\{1,3,4,7,8,9\}}$, $p_{\{2,3,5,6,7,9\}}$
(4)Occipital-Parietal	0.760	3	$\mu_{1,\{2,4\}}$, $\mu_{2,\{2,3,4\}}$, $p_{\{2,3,5,7,8\}}$
(5) Posterior Temporal	0.734	3	$\mu_{1,\{1,2,5,6,7\}}$, $\mu_{2,\{1,2,4,5,6,7,8,9\}}$, $p_{\{1,2,6,7,8\}}$
(6) Lower Temporal	0.678	3	$\mu_{1,\{3,7\}}$, $\mu_{2,\{3,8\}}$, $p_{\{2,3,5,9\}}$
(7) Upper Temporal	0.646	3	$\mu_{1,\{1,3,5,7,8\}}$, $\mu_{2,\{2,3,5,7,8\}}$, $p_{\{2,3,5,6\}}$
(8) Posterior Cingulate	0.812	3	$\mu_{1,\{1,3,4,6,7\}}$, $\mu_{2,\{1,3,4,7,8,9\}}$, $p_{\{2,3,5\}}$
(9) Medial Temporal	0.888	3	$\mu_{1,\{1,3,4,5,7,9\}}$, $\mu_{2,\{1,2,3,5,7,8,9\}}$, $p_{\{3,5,6,7,9\}}$
(C) d/dt p			
	R^2	LVs	Predictors
(1) Upper Parietal	0.797	3	$\mu_{1,\{1,2,3,5,6,8,9\}}$, $\mu_{2,\{1,2,3,5,6,7,8\}}$, $p_{\{1,3,6,9\}}$
(2) Posterior Frontal	0.786	2	$\mu_{1,\{2,4\}}$, $\mu_{2,\{3,4\}}$, $p_{\{2,3,8\}}$
(3) Prefrontal	0.865	3	$\mu_{1,\{1,3,8\}}$, $\mu_{2,\{1,2,3,5,7\}}$, $p_{\{2,3,6,8,9\}}$
(4)Occipital-Parietal	0.708	3	$\mu_{1,\{1,2,5\}}$, $\mu_{2,\{1,2,4,5,6,7\}}$, $p_{\{5,8,9\}}$
(5) Posterior Temporal	0.832	3	$\mu_{1,\{5,8\}}$, $\mu_{2,\{1,5,7\}}$, $p_{\{3,5,9\}}$
(6) Lower Temporal	0.877	3	$\mu_{1,\{6,8\}}$, $\mu_{2,\{2,3,5,8,9\}}$, $p_{\{6\}}$
(7) Upper Temporal	0.864	3	$p_{\{2,3,6,7,9\}}$
(8) Posterior Cingulate	0.519	3	$\mu_{1,\{8\}}$, $\mu_{2,\{1,6\}}$, $p_{\{8\}}$
(9) Medial Temporal	0.858	3	$\mu_{1,\{1,6,8,9\}}$, $\mu_{2,\{1,2,3,6,7,9\}}$, $p_{\{5,6,7,9\}}$

Table S1.9: RE-DVR PLS Regression Model Details: Rates of change in the admixture parameters μ_1 (A), μ_2 (B), and p (C), estimated from RE-DVR images across nine VOIs in Controls. Predictors shown, ($x_{\{i,j,k,...\}}$) are the estimated parameter x from VOIs {i,j,k,...}. R^2 value shown is percent-variance of dependant variables explained by the model.

(A) d/dt μ_1	Controls		
	R^2	LVs	Predictors
(1) Upper Parietal	0.869	3	$\mu_{1,\{1,7\}},\ \mu_{2,\{1,7,8\}},\ p_{\{6,9\}}$
(2) Posterior Frontal	0.698	2	$\mu_{1,\{1,3,8\}},\ \mu_{2,\{1,9\}},\ p_{\{1,2\}}$
(3) Prefrontal	0.740	2	$\mu_{1,\{1,4,5\}},\ \mu_{2,\{4\}},\ p_{\{6,9\}}$
(4)Occipital-Parietal	0.675	3	$\mu_{1,\{4,6,7\}},\ \mu_{2,\{2,3,8\}},\ p_{\{8\}}$
(5) Posterior Temporal	0.776	3	$\mu_{1,\{4,7\}},\ \mu_{2,\{3,4,5\}},\ p_{\{5,7,8\}}$
(6) Lower Temporal	0.910	3	$\mu_{1,\{6,9\}},\ \mu_{2,\{2,4\}},\ p_{\{3,8\}}$
(7) Upper Temporal	0.856	3	$\mu_{1,\{1,6\}},\ \mu_{2,\{2,3,4,6\}},\ p_{\{7,8\}}$
(8) Posterior Cingulate	0.816	2	$\mu_{1,\{1,2,8\}},\ \mu_{2,\{8\}},\ p_{\{8\}}$
(9) Medial Temporal	0.916	3	$\mu_{1,\{6,9\}},\ \mu_{2,\{6,7,9\}},\ p_{\{6,7\}}$
(B) d/dt μ_2			
	R^2	LVs	Predictors
(1) Upper Parietal	0.897	3	$\mu_{1,\{6,7\}},\ \mu_{2,\{4,7,8\}},\ p_{\{1,6,7\}}$
(2) Posterior Frontal	0.852	3	$\mu_{1,\{1,8\}},\ \mu_{2,\{1,4,6,8\}}$
(3) Prefrontal	0.875	3	$\mu_{1,\{4,5,7\}},\ \mu_{2,\{2,4,6,9\}},\ p_{\{8\}}$
(4)Occipital-Parietal	0.840	3	$\mu_{1,\{3,4,6\}},\ \mu_{2,\{2,4,6\}},\ p_{\{6,8\}}$
(5) Posterior Temporal	0.891	3	$\mu_{1,\{3,4,7,9\}},\ \mu_{2,\{1,2,3,4,7\}},\ p_{\{7,8\}}$
(6) Lower Temporal	0.856	3	$\mu_{1,\{2,4,7,8\}},\ \mu_{2,\{2,4\}},\ p_{\{2,6,7,8\}}$
(7) Upper Temporal	0.914	3	$\mu_{1,\{3\}},\ \mu_{2,\{1,3,4,7,9\}},\ p_{\{6,7\}}$
(8) Posterior Cingulate	0.718	2	$\mu_{1,\{8,9\}},\ \mu_{2,\{6,8,9\}},\ p_{\{8\}}$
(9) Medial Temporal	0.858	2	$\mu_{1,\{4,6,9\}},\ \mu_{2,\{2,4,8,9\}},\ p_{\{7\}}$
(C) d/dt p			
	R^2	LVs	Predictors
(1) Upper Parietal	0.845	3	$\mu_{1,\{1,7\}},\ \mu_{2,\{1,3,5,7,9\}},\ p_{\{1,4,6,9\}}$
(2) Posterior Frontal	0.737	2	$\mu_{1,\{1,5\}},\ \mu_{2,\{1,5\}},\ p_{\{1,2\}}$
(3) Prefrontal	0.932	3	$\mu_{1,\{1,4,9\}},\ \mu_{2,\{4,5\}},\ p_{\{3\}}$
(4)Occipital-Parietal	0.700	3	$\mu_{1,\{5,6\}},\ \mu_{2,\{1,4,5,8\}},\ p_{\{1,4\}}$
(5) Posterior Temporal	0.420	2	$\mu_{1,\{6,8\}},\ \mu_{2,\{1,3,4\}},\ p_{\{1,2,5,6\}}$
(6) Lower Temporal	0.808	3	$\mu_{1,\{6\}},\ \mu_{2,\{5\}},\ p_{\{2,3,6,8\}}$
(7) Upper Temporal	0.911	3	$\mu_{1,\{9\}},\ \mu_{2,\{8,9\}},\ p_{\{5,6,7\}}$
(8) Posterior Cingulate	0.751	2	$\mu_{1,\{1,2,8,9\}},\ \mu_{2,\{8\}},\ p_{\{8\}}$
(9) Medial Temporal	0.919	3	$\mu_{1,\{7\}},\ \mu_{2,\{1,5,7,9\}},\ p_{\{1,7\}}$

Table S1.10: RE-DVR PLS Regression Model Details: Rates of change in the admixture parameters μ_1 (A), μ_2 (B), and p (C), estimated from RE-DVR images across nine VOIs in MCI Subjects. Predictors shown, ($x_{\{i,j,k,...\}}$) are the estimated parameter x from VOIs {i,j,k,...}. R^2 value shown is percent-variance of dependant variables explained by the model.

(A) d/dt μ_1	MCIs		
	R^2	LVs	Predictors
(1) Upper Parietal	0.893	3	$\mu_{1,\{1,2,4,8\}}$, $\mu_{2,\{2\}}$, $p_{\{5\}}$
(2) Posterior Frontal	0.743	2	$\mu_{1,\{3,7\}}$, $\mu_{2,\{7\}}$, $p_{\{3,5,6\}}$
(3) Prefrontal	0.840	3	$\mu_{1,\{2,3,5,7\}}$, $\mu_{2,\{2,9\}}$, $p_{\{4\}}$
(4)Occipital-Parietal	0.870	3	$\mu_{1,\{3,4\}}$, $\mu_{2,\{4,7,9\}}$, $p_{\{5,7\}}$
(5) Posterior Temporal	0.796	2	$\mu_{1,\{3,5,6,7,8\}}$, $\mu_{2,\{2\}}$, $p_{\{2,3,9\}}$
(6) Lower Temporal	0.847	3	$\mu_{1,\{1,6,8\}}$, $\mu_{2,\{4,5\}}$, $p_{\{5\}}$
(7) Upper Temporal	0.852	3	$\mu_{1,\{1,2,7,8\}}$, $\mu_{2,\{3,7\}}$, $p_{\{2,5\}}$
(8) Posterior Cingulate	0.732	2	$\mu_{1,\{2,8\}}$, $\mu_{2,\{4\}}$, $p_{\{4,8\}}$
(9) Medial Temporal	0.896	3	$\mu_{1,\{9\}}$, $\mu_{2,\{3,5,9\}}$, $p_{\{5\}}$
(B) d/dt μ_2			
	R^2	LVs	Predictors
(1) Upper Parietal	0.890	3	$\mu_{1,\{2,4,5,8\}}$, $\mu_{2,\{2,3,7,8\}}$, $p_{\{5,7\}}$
(2) Posterior Frontal	0.917	3	$\mu_{1,\{2,4\}}$, $\mu_{2,\{4\}}$, $p_{\{5,7,9\}}$
(3) Prefrontal	0.929	3	$\mu_{1,\{1,2,4\}}$, $\mu_{2,\{4,6,8\}}$, $p_{\{5,7,9\}}$
(4)Occipital-Parietal	0.907	2	$\mu_{1,\{2,4\}}$, $\mu_{2,\{4\}}$, $p_{\{5,7,9\}}$
(5) Posterior Temporal	0.737	2	$\mu_{1,\{4,8\}}$, $\mu_{2,\{4\}}$, $p_{\{2,5,9\}}$
(6) Lower Temporal	0.790	3	$\mu_{1,\{2,4,8\}}$, $\mu_{2,\{3,8\}}$, $p_{\{5\}}$
(7) Upper Temporal	0.660	2	$\mu_{1,\{2,4,8\}}$, $\mu_{2,\{2,7\}}$, $p_{\{5\}}$
(8) Posterior Cingulate	0.840	2	$\mu_{1,\{2,4\}}$, $\mu_{2,\{3,4,7,8,9\}}$, $p_{\{5,7\}}$
(9) Medial Temporal	0.854	3	$\mu_{1,\{4,9\}}$, $\mu_{2,\{3,8\}}$, $p_{\{2,3,5,7\}}$
(C) d/dt p			
	R^2	LVs	Predictors
(1) Upper Parietal	0.862	3	$\mu_{1,\{4,6,7,9\}}$, $p_{\{1,6,8,9\}}$
(2) Posterior Frontal	0.861	3	$\mu_{1,\{3,7,9\}}$, $\mu_{2,\{3,5\}}$, $p_{\{2,9\}}$
(3) Prefrontal	0.903	3	$\mu_{1,\{1,2,3,5\}}$, $\mu_{2,\{2,9\}}$, $p_{\{2,3\}}$
(4)Occipital-Parietal	0.861	2	$\mu_{1,\{1,2,3\}}$, $p_{\{4\}}$
(5) Posterior Temporal	0.522	2	$\mu_{1,\{2,6\}}$, $p_{\{2,3,5,8\}}$
(6) Lower Temporal	0.744	2	$\mu_{1,\{2,4,6\}}$, $p_{\{6\}}$
(7) Upper Temporal	0.860	2	$\mu_{1,\{7,9\}}$, $\mu_{2,\{3\}}$, $p_{\{2,7\}}$
(8) Posterior Cingulate	0.709	2	$\mu_{1,\{4\}}$, $\mu_{2,\{3\}}$, $p_{\{3,5,7,8\}}$
(9) Medial Temporal	0.850	3	$\mu_{1,\{6,7,8,9\}}$, $\mu_{2,\{3,9\}}$, $p_{\{3,5,9\}}$

Table S1.11: OLS Regression Model Details: Rates of change in six psychological Z scores in Controls and MCIs, using either Logan (A) or relative-equilibrium (B) DVR mean values as predictors. NA values represent VOIs in which no model with regression parameters significantly different from zero could be found.

(A) d/dt Z-score Logan-DVR	Controls								
	Adj-R^2	R^2	x_1	x_2	x_3	b_0	b_1	b_2	b_3
Executive Function	0.457	0.530	$\bar{x}_7$	$\bar{x}_9$	-	$1.8\text{x}10^{-3}$	$1.4\text{x}10^{-2}$	$-1.5\text{x}10^{-2}$	-
Language	NA	NA	-	-	-	-	-	-	-
Visuo-spatial	0.396	0.436	$\bar{x}_1$	$\bar{x}_2$	-	-	$2.0\text{x}10^{-2}$	$-2.0\text{x}10^{-2}$	-
Psychomotor	0.701	0.761	$\bar{x}_2$	$\bar{x}_3$	$\bar{x}_9$	$1.4\text{x}10^{-2}$	$-1.7\text{x}10^{-2}$	$2.0\text{x}10^{-2}$	$-1.6\text{x}10^{-2}$
Neuropsychological	0.390	0.437	$\bar{x}_4$	$\bar{x}_9$	-	-	$8.9\text{x}10^{-3}$	$-8.6\text{x}10^{-3}$	-
Memory	NA	NA	-	-	-	-	-	-	-
	MCIs								
	Adj-R^2	R^2	x_1	x_2	x_3	b_0	b_1	b_2	b_3
Executive Function	NA	NA	-	-	-	-	-	-	-
Language	0.306	0.388	$\bar{x}_1$	$\bar{x}_4$	-	$-2.5\text{x}10^{-3}$	$-1.3\text{x}10^{-2}$	$1.5\text{x}10^{-2}$	-
Visuo-spatial	0.187	0.235	$\bar{x}_8$	-	-	$-6.9\text{x}10^{-3}$	$5.7\text{x}10^{-3}$	-	-
Psychomotor	0.224	0.315	$\bar{x}_5$	$\bar{x}_7$	-	$-6.2\text{x}10^{-3}$	$-1.4\text{x}10^{-2}$	$1.9\text{x}10^{-3}$	
Neuropsychological	NA	NA	-	-	-	-	-	-	-
Memory	NA	NA	-	-	-	-	-	-	-

(B) d/dt Z-score RE-DVR	Controls								
	Adj-R^2	R^2	x_1	x_2	x_3	b_0	b_1	b_2	b_3
Executive Function	0.576	0.661	$\bar{x}_1$	$\bar{x}_3$	$\bar{x}_9$	$2.1\text{x}10^{-2}$	$-2.3\text{x}10^{-2}$	$2.2\text{x}10^{-2}$	$-2.0\text{x}10^{-2}$
Language	0.302	0.348	$\bar{x}_6$	$\bar{x}_8$	-	-	$8.2\text{x}10^{-3}$	$-8.0\text{x}10^{-3}$	-
Visuo-spatial	0.469	0.501	$\bar{x}_4$	$\bar{x}_7$	-	-	$1.5\text{x}10^{-2}$	$-1.5\text{x}10^{-2}$	-
Psychomotor	0.624	0.700	$\bar{x}_3$	$\bar{x}_8$	$\bar{x}_9$	$1.2\text{x}10^{-2}$	$1.2\text{x}10^{-2}$	$-1.4\text{x}10^{-2}$	$-8.4\text{x}10^{-3}$
Neuropsychological	0.393	0.433	$\bar{x}_8$	-	-	$8.7\text{x}10^{-2}$	$-8.0\text{x}10^{-2}$	-	-
Memory	NA	NA	-	-	-	-	-	-	-
	MCIs								
	Adj-R^2	R^2	x_1	x_2	x_3	b_0	b_1	b_2	b_3
Executive Function	NA	NA	-	-	-	-	-	-	-
Language	0.243	0.287	$\bar{x}_1$	$\bar{x}_4$	-	-	$-1.4\text{x}10^{-2}$	$1.4\text{x}10^{-2}$	-
Visuo-spatial	0.184	0.232	$\bar{x}_3$	$\bar{x}_8$	-	-	$-1.4\text{x}10^{-2}$	$1.4\text{x}10^{-2}$	-
Psychomotor	0.222	0.267	$\bar{x}_5$	$\bar{x}_7$	-	-	$-1.5\text{x}10^{-2}$	$1.5\text{x}10^{-2}$	
Neuropsychological	NA	NA	-	-	-	-	-	-	-
Memory	NA	NA	-	-	-	-	-	-	-

Table S1.12: OLS Regression Model Details: Rates of change in six psychological Z scores in Controls and MCIs, using either Logan (A) or relative-equilibrium (B) DVR admixture parameters as predictors.

(A) d/dt Z-score Logan-DVR	Controls								
	Adj-R^2	R^2	x_1	x_2	x_3	b_0	b_1	b_2	b_3
Executive Function	0.858	0.887	p_1	p_5	p_9	$2.7\text{x}10^{-3}$	$5.9\text{x}10^{-3}$	$-3.3\text{x}10^{-3}$	$3.5\text{x}10^{-3}$
Language	0.449	0.522	$\mu_{1,5}$	$\mu_{1,9}$	p_3	-	$-7.4\text{x}10^{-3}$	$5.4\text{x}10^{-3}$	$4.6\text{x}10^{-3}$
Visuo-spatial	0.850	0.880	$\mu_{1,5}$	$\mu_{2,7}$	p_6	$4.1\text{x}10^{-3}$	$-1.4\text{x}10^{-2}$	$1.1\text{x}10^{-2}$	$-2.5\text{x}10^{-3}$
Psychomotor	0.783	0.826	$\mu_{2,4}$	$\mu_{2,9}$	p_9	$6.2\text{x}10^{-3}$	$7.1\text{x}10^{-3}$	$-1.2\text{x}10^{-2}$	$-2.4\text{x}10^{-3}$
Neuropsychological	0.570	0.623	p_1	p_5	p_9	-	$2.6\text{x}10^{-3}$	$-2.8\text{x}10^{-3}$	$1.3\text{x}10^{-3}$
Memory	0.423	0.461	p_1	p_5	-	-	$5.2\text{x}10^{-3}$	$-3.9\text{x}10^{-3}$	-
	MCIs								
	Adj-R^2	R^2	x_1	x_2	x_3	b_0	b_1	b_2	b_3
Executive Function	0.616	0.684	$\mu_{1,1}$	$\mu_{1,5}$	p_6	$-1.1\text{x}10^{-2}$	$-1.3\text{x}10^{-2}$	$1.7\text{x}10^{-2}$	$9.1\text{x}10^{-3}$
Language	0.544	0.625	$\mu_{1,5}$	$\mu_{2,1}$	p_3	$8.4\text{x}10^{-3}$	$1.3\text{x}10^{-2}$	$-1.7\text{x}10^{-2}$	$-5.5\text{x}10^{-3}$
Visuo-spatial	0.571	0.623	$\mu_{1,2}$	$\mu_{2,8}$	p_1	-	$-1.3\text{x}10^{-2}$	$7.6\text{x}10^{-3}$	$6.6\text{x}10^{-3}$
Psychomotor	0.222	0.36	$\mu_{1,7}$	$\mu_{2,5}$	p_7	$-4.9\text{x}10^{-3}$	$1.2\text{x}10^{-2}$	$-8.4\text{x}10^{-3}$	$3.0\text{x}10^{-3}$
Neuropsychological	0.594	0.667	$\mu_{1,1}$	$\mu_{1,4}$	p_6	$-4.6\text{x}10^{-3}$	$-9.8\text{x}10^{-3}$	$1.1\text{x}10^{-2}$	$4.1\text{x}10^{-3}$
Memory	0.476	0.568	$\mu_{2,2}$	p_1	p_5	$-9.3\text{x}10^{-3}$	$-9.9\text{x}10^{-3}$	$5.8\text{x}10^{-3}$	$-2.3\text{x}10^{-3}$

(B) d/dt Z-score RE-DVR	Controls								
	Adj-R^2	R^2	x_1	x_2	x_3	b_0	b_1	b_2	b_3
Executive Function	0.828	0.863	$\mu_{2,3}$	$\mu_{2,7}$	$\mu_{2,9}$	$9.9\text{x}10^{-3}$	$1.3\text{x}10^{-2}$	$-1.4\text{x}10^{-2}$	$-6.8\text{x}10^{-3}$
Language	0.641	0.713	$\mu_{2,2}$	$\mu_{2,3}$	p_5	$4.1\text{x}10^{-3}$	$-1.5\text{x}10^{-2}$	$9.6\text{x}10^{-3}$	$3.0\text{x}10^{-3}$
Visuo-spatial	0.678	0.742	$\mu_{1,8}$	p_1	p_3	$9.1\text{x}10^{-3}$	$-6.4\text{x}10^{-3}$	$-2.7\text{x}10^{-3}$	$-1.9\text{x}10^{-3}$
Psychomotor	0.756	0.788	$\mu_{1,4}$	$\mu_{1,6}$	$\mu_{1,9}$	-	$1.3\text{x}10^{-2}$	$-8.3\text{x}10^{-3}$	$-4.1\text{x}10^{-3}$
Neuropsychological	0.686	0.728	$\mu_{1,4}$	$\mu_{1,8}$	p_9	-	$4.1\text{x}10^{-3}$	$-4.6\text{x}10^{-3}$	$1.7\text{x}10^{-3}$
Memory	0.435	0.510	$\mu_{2,4}$	$\mu_{2,9}$	p_6	-	$1.4\text{x}10^{-2}$	$-1.1\text{x}10^{-2}$	$-4.6\text{x}10^{-3}$
	MCIs								
	Adj-R^2	R^2	x_1	x_2	x_3	b_0	b_1	b_2	b_3
Executive Function	0.802	0.825	$\mu_{1,1}$	p_1	p_5	-	$-7.0\text{x}10^{-3}$	$8.3\text{x}10^{-3}$	$2.9\text{x}10^{-3}$
Language	0.597	0.645	$\mu_{1,4}$	$\mu_{2,2}$	p_1	-	$1.0\text{x}10^{-2}$	$-1.1\text{x}10^{-2}$	$2.5\text{x}10^{-3}$
Visuo-spatial	0.751	0.795	$\mu_{1,1}$	$\mu_{1,8}$	p_7	$-9.5\text{x}10^{-3}$	$-1.3\text{x}10^{-2}$	$1.9\text{x}10^{-2}$	$3.4\text{x}10^{-3}$
Psychomotor	0.477	0.539	$\mu_{2,4}$	$\mu_{2,5}$	p_3	-	$2.9\text{x}10^{-2}$	$-3.2\text{x}10^{-2}$	$6.2\text{x}10^{-3}$
Neuropsychological	0.721	0.754	$\mu_{1,2}$	p_1	p_7	-	$-3.4\text{x}10^{-2}$	$3.5\text{x}10^{-2}$	$1.9\text{x}10^{-3}$
Memory	0.598	0.669	$\mu_{1,2}$	p_1	p_8	$7.6\text{x}10^{-3}$	$-8.4\text{x}10^{-3}$	$2.7\text{x}10^{-3}$	$-1.9\text{x}10^{-3}$

Table S1.13: PLS Regression Model Details: Rates of change in six psychological Z scores in controls and MCIs, using either Logan (A) or relative-equilibrium (B) DVR admixture parameters as predictors. R^2 value shown is percent-variance of dependant variables explained by the model.

(A) d/dt Z-score Logan-DVR	Controls			MCI		
	R^2	LVs	Predictors	R^2	LVs	Predictors
Executive Function	0.87	3	$\mu_{1,\{9\}}$, $\mu_{2,\{1,7,9\}}$, $p_{\{1,2,4,6,9\}}$	0.71	2	$\mu_{1,\{1,3,4,5\}}$, $\mu_{2,\{8\}}$, $p_{\{5,6,7\}}$
Language	0.77	3	$\mu_{1,\{1,3,8\}}$, $\mu_{2,\{1,3,4,5,8,9\}}$, $p_{\{1,4,6,7\}}$	0.69	3	$\mu_{1,\{5,8\}}$, $\mu_{2,\{2\}}$, $p_{\{2,7,8\}}$
Visuo-spatial	0.86	3	$\mu_{1,\{6,7,8\}}$, $\mu_{2,\{8\}}$, $p_{\{1,3,5,6,7\}}$	0.72	3	$\mu_{1,\{1,2,6,9\}}$, $\mu_{2,\{4,8\}}$, $p_{\{1,2,3,7\}}$
Psychomotor	0.85	3	$\mu_{1,\{2,7,8,9\}}$, $\mu_{2,\{7,8,9\}}$, $p_{\{4,6,7\}}$	0.55	2	$\mu_{2,\{4,5,7\}}$, $p_{\{1,2,7,8\}}$
Neuropsychological	0.81	3	$\mu_{1,\{6,8,9\}}$, $p_{\{1,4,5,6,7,9\}}$	0.66	1	$\mu_{1,\{2,6\}}$, $p_{\{1,2,6,7,8\}}$
Memory	0.53	3	$\mu_{1,\{1,9\}}$, $\mu_{2,\{4,7,9\}}$, $p_{\{1,2,4,6,9\}}$	0.74	3	$\mu_{1,\{1,2,3,6\}}$, $\mu_{2,\{2\}}$, $p_{\{1,4,6,9\}}$

(B) d/dt Z-score RE-DVR	Controls			MCI		
	R^2	LVs	Predictors	R^2	LVs	Predictors
Executive Function	0.90	3	$\mu_{1,\{6,7,9\}}$, $\mu_{2,\{9\}}$, $p_{\{2,6,7,9\}}$	0.85	2	$\mu_{1,\{1\}}$, $\mu_{2,\{8\}}$, $p_{\{1,7\}}$
Language	0.70	2	$\mu_{1,\{1,8\}}$, $\mu_{2,\{8\}}$, $p_{\{2,5,7,8\}}$	0.69	2	$\mu_{1,\{1,2,4\}}$, $p_{\{1,6,7\}}$
Visuo-spatial	0.91	3	$\mu_{1,\{4,8\}}$, $p_{\{1,3,5,6,8,9\}}$	0.77	2	$\mu_{1,\{2,8,9\}}$, $\mu_{2,\{4\}}$, $p_{\{1,3,7\}}$
Psychomotor	0.84	2	$\mu_{1,\{1,4,6,9\}}$, $\mu_{2,\{8\}}$,	0.60	2	$\mu_{1,\{4\}}$, $\mu_{2,\{5,7,9\}}$, $p_{\{1,3,5,7,8\}}$
Neuropsychological	0.82	3	$\mu_{1,\{4,8,9\}}$, $\mu_{2,\{3,7,8,9\}}$, $p_{\{6,9\}}$	0.79	2	$\mu_{1,\{1\}}$, $p_{\{1,4,7,9\}}$
Memory	0.69	3	$\mu_{1,\{1,4,7,8\}}$, $\mu_{2,\{3,7,9\}}$, $p_{\{6,9\}}$	0.79	3	$\mu_{1,\{2,3\}}$, $\mu_{2,\{7,9\}}$, $p_{\{1,8\}}$

CHAPTER 4 - Improved Modeling of *in vivo* Kinetics of Slowly Diffusing Radiotracers for Tumor Imaging

Abstract

Large-molecule tracers, such as labeled antibodies, have shown success in immunoPET for imaging of specific cell-surface biomarkers. However, previous work has shown that localization of such tracers shows high levels of heterogeneity in target tissues, due to both the slow diffusion and high affinity of these compounds. In this work we investigate the effects of sub-voxel spatial heterogeneity on measured time activity curves (TACs) in PET imaging, and the effects of ignoring diffusion-limitation on parameter estimates from kinetic modeling. Partial differential equations (PDE) were built to model a radially symmetric reaction-diffusion equation describing activity of immunoPET tracers. Effects of slower diffusion on measured TACs and parameter estimates were measured *in silico*, and a modified Levenberg-Marquardt algorithm with Bayesian priors was developed to accurately estimate parameters from diffusion-limited data. This algorithm was applied to immunoPET data of mice implanted with prostate stem cell antigen (PSCA) over-expressing tumors and injected with ^{124}I-labeled A11 anti-PSCA minibody.

Slow diffusion of tracers in linear binding models resulted in heterogeneous localization *in silico*, but no measurable differences in TACs. For more realistic saturable binding models, measured TACs were strongly dependent on diffusion rates of the tracers. Fitting diffusion-limited data with regular compartmental models led to parameter estimate bias in excess of 1000% of true values, where the new model and fitting protocol could accurately measure kinetics *in silico*. *In vivo* imaging data was also fit well by the new PDE model, with estimates of Kd and receptor

density close to *in vitro* measurements and with order of magnitude differences from a regular compartmental model ignoring tracer diffusion-limitation.

Heterogeneous localization of large, high-affinity compounds can lead to large differences in measured TACs in immunoPET imaging, and ignoring diffusion-limitations can lead to large errors in kinetic parameter estimates. Modeling of these systems with PDE models with Bayesian priors is necessary for quantitative *in vivo* measurements of kinetics of slow diffusion tracers.

4.1 Introduction

Radiolabeled antibodies have shown great utility in both imaging and therapeutics, but there are obstacles to accurate quantification of these compounds *in vivo* [1-5]. There are many antibodies approved for clinical use, with even more in phase I-III trials, however the full kinetic activity of these compounds has yet to be completely understood quantitatively [1,6]. It has long been known that although monoclonal antibodies show high specificity in target tissues, there is a divergence in spatial localization between *in vivo* and *in vitro* studies [7]. Early *in silico* work showed that slow diffusivity of these molecules in target tissues can lead to steep concentration gradients of tracers in tissue on the sub-voxel level [8]. Intact antibodies (~150 kDa), are orders of magnitude larger than traditional small molecule tracers (usually <1 kDa), and their larger size results in both reduced capillary permeability and slower rates of diffusion in tissues [9].

Another major factor leading to heterogeneous localization of these molecules is their high affinity in target tissues [10-12]. Due to their high affinity, heterogeneous localization is observed even with relatively small (25 kDa) single-chain variable fragments (scFvs) and with small micrometastases, [13-14]. Understanding the simultaneous effects of imaging agent size and affinity has been further complicated by studies showing variable tumor penetration of several trastuzumab (146 kDa) derivatives, and limited tumor penetration of the much smaller (.5 kDa) doxorubicin [15,16].

These complications necessitate a new class of kinetic models which will allow for improved PET quantitation and therapeutic planning. When using these molecules as therapeutics, spatial heterogeneity on length scales less than 100μm leads to large volumes of target tumors being completely devoid of treatment, with almost all localization close to the capillary wall [17]. The ability to robustly plan treatment protocols with these compounds, with appropriate dose at all depths in tissue, is contingent upon knowledge of biological parameters such as receptor density in target tumors and full kinetic knowledge of the probes. Previously, however, in order to accurately measure these necessary parameters, investigators would need to employ some combination of compartmental kinetic modeling or Scatchard analysis, which both assume well-mixed or uniform compartmental activity on the sub-voxel level [18]. As described above, in the case of large high-affinity compounds, such as labeled antibodies, these assumptions are violated. Despite these deviations from standard assumptions, some properties of labeled antibodies confer advantages and simplifications to quantification of immunoPET. With few exceptions (e.g. anti-HER2 antibodies), due to the high specificity of antibody based imaging agents there will be little to no uptake in myocardial tissue, allowing for accurate measurements of image derived input functions from the left ventricle. Additionally, the high specificity of tracers will lead to high signal-to-noise ratios and low background activity. Therefore, in this work we propose, implement, and test a method for accurately measuring the kinetic activity of such compounds *in vivo*, through a set of partial differential equations (PDEs) describing the reaction-diffusion equations governing this system. Although previous work has investigated the effect that this tissue heterogeneity will have on whole-tumor activity over time, until now there has yet to be work published on the accurate extraction of kinetic parameters from PET imaging in such situations, and determining the true dose-at-depth in therapeutics for such systems [11,19].

In addition to simulation studies, we apply the results of the *in silico* work to *in vivo* imaging of the ^{124}I-labeled A11 (^{124}I-A11) minibody in prostate cancer xenografts. The minibody (scFv-CH3, homodimer, 80 kDa) is an antibody fragment that helps to address the long uptake time and slow blood clearance kinetics of intact antibodies (150 kDa, $t_{1/2}$= days to weeks) by deleting the C_H1 and C_H2 domains to created a fragment that retains the binding strength and specificity of whole antibodies but exhibits faster blood clearance ($t_{1/2}$= 6-8 hours), allowing for high-contrast imaging at earlier time-points [20-22]. The reduced size of these compounds likely contributes to increased penetration into tumors, however they are still large enough to show depth-dependant concentration effects [13,16].

The A11 minibody is engineered for imaging prostate stem cell antigen (PSCA)-expressing tumors [23]. The PSCA antigen is cell surface protein with little normal expression throughout the body, limited to low-level expression in normal prostate, bladder, and stomach [24]. However, it is highly expressed in most local and metastatic prostate cancers with expression levels correlating to Gleason score, tumor invasion, and a poor prognosis [24-27]. The ability to obtain accurate measures of anti-PSCA tracer kinetics could thus be an important tool in staging and monitoring treatment response in prostate cancer. PSCA is additionally over-expressed in bladder and pancreatic cancers. Although previous work has shown that ^{124}I-labeled anti-PSCA minibodies exhibit high-contrast images of PSCA-expressing targets at relatively early time points (6-44 hours), no work has yet been done to quantify the kinetics of these systems [28,29].

In this work, we examine theoretical models of both linear and saturable binding kinetics of large-molecule tracers, and the effect of diffusion rates on measured time activity curves (TACs) from target regions. Next, we investigate the effects of naively fitting diffusion-limited data with regular compartmental models assuming infinitely fast diffusion (i.e. well-mixed compartments), and effective methods for accurately measuring kinetics from such systems. Finally, we apply the previously discovered fitting methods to an *in vivo* investigation of ^{124}I-labeled A11 minibody in xenografts overexpressing PSCA in mice.

4.2 Methods:

4.2.1 Kinetic Models

PDE models were built to simulate the kinetics of a slowly diffusing radiotracer. Tissue was modeled as a non-overlapping composite of radially-symmetric cylinders with radius R. At each radius *r,* away from the capillary wall at r_0, tracer kinetics were modeled as a compartmental system specific to that radius, leading to a system of radially symmetric, reaction-diffusion equations. Two sets of models were built: a simpler PDE model of linear binding kinetics, and a more complex non-linear PDE model of saturable binding kinetics (Eqs. 1&2, respectively). Both sets of reaction-diffusion equations modeled concentration of tracer in interstitial space, bound to surface receptors, and internalized into the cell (u,v, and w, respectively). In the case of saturable binding, the concentration of unbound receptor sites at each radius (x(r,t)) was modeled as well. Both linear and nonlinear PDE models were subject to the same Neumann boundary conditions (Eq. 3). These boundary conditions ensure that there is no leak from the system due to diffusion deep in tissue (r>R), as that loss will be reciprocally matched by leaks into the system from adjacent regions. Initial conditions for all models had zero tracer in tissue, and for nonlinear models initial unbound antigen sites were at steady-state values ($dens_0$). A more complete derivation and explanation of these equations can be found in the supplementary materials.

$$\frac{\delta}{\delta t}u(r,t) = D\left[\frac{\delta^2}{\delta r^2}u(r,t) + \frac{1}{r}\frac{\delta}{\delta r}u(r,t)\right] - k_1u(r,t) + k_2v(r,t)$$
$$\frac{\delta}{\delta t}v(r,t) = k_1u(r,t) - (k_2 + k_3)v(r,t)$$
$$\frac{\delta}{\delta t}w(r,t) = k_3v(r,t) - k_4\, w(r,t)$$

Eq. 1

$$\frac{\delta}{\delta t}u(r,t) = D\left[\frac{\delta^2}{\delta r^2}u(r,t) + \frac{1}{r}\frac{\delta}{\delta r}u(r,t)\right] - k_1u(r,t)x(r,t) + k_2v(r,t)$$
$$\frac{\delta}{\delta t}v(r,t) = k_1u(r,t)x(r,t) - (k_2 + k_4)v(r,t)$$
$$\frac{\delta}{\delta t}x(r,t) = -k_1u(r,t)x(r,t) + k_3(dens_0 - x(r,t)) + k_2v(r,t)$$
$$\frac{\delta}{\delta t}w(r,t) = k_4v(r,t) - \ k_5w(r,t)$$

Eq. 2

$$-D\frac{\delta}{\delta r}u(r,t)\bigg|_{r=r_0} = PC_p(t) - Pu(r_0,t)$$
$$\frac{\delta}{\delta r}u(R,t) = 0$$

Eq. 3

The model governing linear binding kinetics was solved analytically in Laplace space, and numerically inverted into the time domain. The non-linear model cannot be solved analytically, and therefore was solved numerically through a combination of 4th-order Runge-Kutta and method of lines algorithms. Solutions were integrated across all radii (including the plasma compartment), to simulate TACs from the modeled tissue. For both the linear- and saturable-binding kinetic models, ordinary differential equation (ODE) models were built for these systems assuming infinitely fast diffusion (i.e. regular compartmental models), which were solved using 4th order Runge-Kutta numerical analysis.

For non-saturable binding kinetics, the effects of slower diffusion were examined by comparing responses of ODE and PDE models (differing only in rates of diffusion) to a unit impulse. Simulated TACs of saturable-binding ODEs and PDEs were similarly compared, however their simulated TACs were in response to a tri-exponential input function as a unit impulse response would not be sufficient to describe these non-linear systems.

In cases where finite diffusion rates led to measurable differences in TACs, simulated diffusion-limited data with Gaussian noise was fit repeatedly with both finite and infinite diffusion models using standard Levenberg-Marquardt optimization. To overcome possible problems of parameter identifiability, this simulated data was also repeatedly fit using a modified Levenberg-Marquardt algorithm, incorporating weak Baysian priors on binding and disassociate rates, k_{on} and k_{off}, assuming *a priori in vitro* measurements. Priors for kinetic parameters were formulated as log-normal with mean of the true parameter value, and standard deviation equal to .5*ln(10). A more complete description of the objection function can be found in the supplemental materials.

4.2.2 Affinity Studies

The apparent affinity of the unmodified A11 minibody was measured by quartz crystal microbalance (QCM) using an Attana Cell A200. Human PSCA-mFc antigen (40μg/mL) was immobilized on a LNB-carboxyl sensor chip by amine coupling. Binding experiments were performed in HBS 0.005% Tween 20 (25μL/min, 22°C). Five serial dilutions (160 -5 nM) of the construct were run in triplicate in random order. The chip was regenerated using 0.1 M Glycine pH 2.5 between each sample. Buffer injections were performed prior to each sample injection to use as a reference in integrated Attester Evaluation software where the binding curves were fit using a mass transport limited binding model.

4.2.3 Small Animal PET/CT

Two mice were implanted with a control 22Rv1 tumor, a prostate epithelial cell line, expressing almost no PSCA (369 ± 486 antigens/cell) and a contralateral 22Rv1 tumor transfected to over-express PSCA (2.2x10^6 antigens/cell), as described previously [24]. Approximately 25 μg (4 MBq) of ^{124}I-A11 with a purity of 98% or more was administered to tumor-bearing mice via tail vein injection. The iodination of the minibody was performed as described previously, with immunoreactivity of ^{124}I-A11 found to be 76% ± 9.7% [24,30]. Before ^{124}I-A11 administration, thyroid and stomach uptake of radioiodine was blocked, respectively, with Lugol's iodine and potassium perchlorate as previously described [23]. Mice were given an initial 2 h dynamic small-animal PET scan at the time of injection. At 20 and 44 h after injection, mice were anesthetized with 1.5% isoflurane anesthesia and imaged with 10-min acquisitions on an Inveon small-animal PET scanner (Siemens Preclinical Solutions), followed by a micro-CT scan (microCAT II; Siemens Preclinical Solutions) [31]. One mouse was also given 10-minute static scans at 4, 6, 8, and 12 h post injection. All animal experiments were conducted in compliance with a protocol approved by the Institutional Animal Care and Use Committee of the University of California, Los Angeles.

Small-animal PET images were reconstructed by non-attenuation or scatter-corrected filtered backprojection and were analyzed and displayed using AMIDE [32]. Plasma activity was described by an image-derived input function, measured using a cylindrical volume-of-interest (~3 mm^3 in size) covering the left ventricle. Tumor activity was measured using elliptical VOIs covering the tumor. Tissue activity was converted from scanner units to Molar concentration using known specific activity of injected doses, and whole-body activity in the first frame of the dynamic scan. Measured activity was modeled using both ODE and PDE models of saturable binding kinetics. For both models, no intracellular compartment was included, as previous work has shown that intracellular metabolism of ^{124}I-A11 results in very fast cleavage of the PET tracer isotope which is subsequently free to diffuse from the tissue and is then rapidly renally excreted [33].

4.3 Results

Solving the PDE system of linear binding kinetics showed only minor differences (<1%) in simulated unit impulse responses over a range of biologically feasible diffusion parameters ($D > 10\mu m^2 s^{-1}$), and less than 4% difference from a regular compartmental model at very slow diffusion rates ($D=1\ \mu m^2 s^{-1}$). In the linear binding model, slower diffusion rates did lead to large concentration gradients in tissue, such that for biologically reasonable diffusion rates the total dose at the deepest points in tissue were 50% of regions closest to the capillary wall (Supplemental Figure S2.1).

Simulated TACs from the non-linear model governing saturable binding kinetics were much more sensitive to changes in diffusion rates (Figure 1A). As can be seen in Table 1 and Figure 1B, although *in silico* diffusion-limited TACs ($D=14\ \mu m^2 s^{-1}$) could be fit well using a regular compartmental model (i.e. $D = \infty\ \mu m^2 s^{-1}$), parameters obtained with this fitting showed large levels of bias, in excess in 1000% of true values for some parameters.

With the inclusion of Bayesian priors on both the binding and unbinding rates (k_1,k_2), bias rates for both compartmental and diffusion models were reduced. However, for compartmental model fits, mean bias for some parameters without priors were increased (Table 1). Therefore, fitting with Bayesian priors, as opposed to a standard least-squares algorithm was used for *in vivo* data. Input functions, as measured by tracer activity in left ventricle, were well fit by a standard tri-exponential decay (Figure 2). Measured TACs from PSCA-overexpressing tumors were fit with compartmental and diffusion-limited models. In both cases Bayesian priors for k_1 and k_2 were incorporated into the fitting, as determined by QCM ($1.21*10^5$ $(M\cdot s)^{-1}$ and $4.95*10^{-4}$ s^{-1}, respectively) (Supplemental Figure S2.2). As in *in silico* studies, priors were formulated as log-normal distributions. Both models successfully reproduced the measured TACs for the mouse with six static scan time points (mouse 1), but with large differences in fitted kinetic and biological parameters between the diffusion-limited and compartmental models (Table 2). For the mouse with two static scan time points (mouse 2), only the diffusion-limited model was able to reproduce the measured TAC. Results of fitting with the diffusion-limited model, and the effects of diffusion rate on the measured TAC can be seen in Figure 3. Fitted TAC from the second mouse can be seen in supplemental data (Supplemental Figure S2.3).

4.4 Discussion

The results of *in silico* studies suggest that, in the case of linear binding kinetics, there will likely not be any measurable difference in TACs of large molecule imaging agents as differences from an infinite diffusion model were less than 5% even at diffusion rates an order of magnitude smaller than those likely for antibodies [11]. Although slow diffusion of molecules does not appear to have an effect on the measured activity of imaging agents, slow diffusion does result in a steep concentration gradient of the compound in tissue, with *in silico* results showing that differences in dosages can be two-fold across tissue depths. This has important ramifications in the planning of treatment protocols, particularly because the majority of tumor volume is located farther away from the capillary wall where dosage will be lower. However, there are many reasons why the kinetics of the compound *in vivo* would deviate from the linear-binding regime, such as the case of targets with low antigen expression, low specific activity imaging agents, blocking or co-injection studies or large-dosage therapeutic treatments where receptor saturation is often the goal [34]. Furthermore, as shown above (Figure 1A), even in cases of relatively low saturation of available receptors, slow diffusion can result in large and measurable differences in TACs. Therefore, it is likely that for most *in vivo* applications the usage of non-linear saturable binding models will be necessary and the non-diffusion-limited linear model will show considerable error for estimates of biological parameters despite good appearing fits of the *in vivo* data.

While diffusion-limited data can be fit well with either a compartmental or diffusion model (Figure 1B), the large differences in fitted parameters reveal the problem of parameter identifiability in this case. The results of the *in silico* fitting results shown in Table 1 also show that naively fitting TACs of slowly diffusing compounds with high target affinity can lead to large errors (>1000%) in important kinetic parameters. These results all suggest that while a non-compartmental model incorporating rates of diffusion is necessary to accurately model *in vivo* kinetics of large-molecule tracers, standard fitting techniques will not be sufficient. Adding Bayesian priors to parameters that can be measured *in vitro* before scanning is shown to be a viable approach in overcoming problems of parameter identifiability. Although there are still large errors in some parameter estimates when using a regular compartmental model with Bayesian priors, some parameters not constrained by *a priori* measurements can have low bias, such as capillary permeability and tumor blood volume.

Results of fitting *in vivo* imaging data of the A11 minibody largely confirm results from the initial *in silico* simulations. It can be seen that while TACs can be fit (in terms of sum of squared errors) with a regular compartmental model, parameter estimates vary greatly from both Bayesian priors and results of diffusion-limited fitting, but with only small differences in fitted values of capillary permeability and blood volume. Most notably is the divergence in predicted receptor density when ignoring diffusion limitations, with more than a 600% difference in model predictions. As receptor density can be an important factor in staging tumor progression and evaluating the response of the tumor to therapeutic interventions, accurate estimates of this parameter is incredibly important for the utility of quantitative immunoPET [25].

Parameters yielded from diffusion-limited models showed strong agreement between both mice scanned, even with one mouse having four fewer static scans. Additionally, parameter estimates for capillary permeability were similar to previously estimated results ($3\text{-}5*10^{-9}$ m/s) [11]. There was likewise excellent agreement between Kd as measured with QCM (4.1 nM) and as measured by kinetic modeling (1.3 nM and 2.4 nM). While there were small differences, these are likely explained by differing microenvironments between *in vivo* studies and the *in vitro* QCM experiment. Although the a priori measurements were performed on unlabeled compounds, previous work has shown that the iodination of the minibody will not result in changes to Kd [24]. With *in vivo* studies, there can be a multitude of binding co-factors that could reduce the dissociation constant that would not be present *in vitro*, leading to larger Kd measures in experiments such as QCM.

The results shown here, from both *in silico* and *in vivo* studies, reveal the importance of considering diffusion in the quantification of high-affinity compounds in both imaging and therapeutic planning. Fitting results demonstrate that biological and kinetic information can be successfully extracted from immunoPET data with the use of physically accurate diffusion-limited models, while data naively fit with regular compartmental models can lead to very large errors. This has important repercussions in both therapeutic planning, where proper dosages need to be delivered to the entire tumor volume, as well as in immunoPET applications for staging disease progression.

There are still some limitations in transitioning quantitative immunoPET modeling into clinical usage. Firstly, in this work we have presented fitting data of a tracer with a radioisotope that is rapidly cleaved and excreted after internalization. This phenomenon alleviates the need for an intra-cellular compartment and reduces the number of parameters needed for fitting. Tracers with radioisotopes that are not rapidly cleared after endocytosis (such as A11 conjugated with ^{89}Zr), will require more complicated models that may be more difficult to fit than those described above [35]. Future work is in progress to model TACs measured from mice implanted with 22rv1xPSCA tumors scanned with ^{89}Zr-A11 to confirm the utility of this model in more complex systems.

An additional barrier to this quantitative analysis in clinical use is the repeated scan times and long biological half-life of these tracers. The minibodies used in this work show a substantial improvement over whole-antibodies in biological half-life and reduce the time over which TACs need to be measured, thus lessening this barrier. However the protocol used in this study, with 7 scans over the period of 44 hours, is still much more than would be viable in clinical usage. Therefore, future work is planned on optimizing dosage and scan protocols to minimize scan numbers and durations, while maintaining parameter identifiability in kinetic analysis.

4.5 Conclusion

This work shows that slow diffusion of high-affinity compounds will have little effect on measured TACs in immunoPET for linear binding kinetics. However, in the likely case of saturable binding (due to low receptor expression, low labeling efficiency, blocking/co-injection studies, or therapeutic antibody doses) slow diffusion will have a strong effect on measured TACs. Using regular compartmental models to estimate biological and kinetic parameters of such diffusion-limited data can lead to large errors, which can be alleviated through the use of non-linear PDE models and the incorporation of Bayesian priors. Future work is planned to validate the use of this fitting technique in intracellularly retained tracers, such as ^{89}Zr-A11, and to optimize imaging protocols for such tracers to minimize scan time and retain parameter identifiability.

Acknowledgments

We thank Dr. David Stout at the Crump Small Animal Imaging Facility, and Dr. Paul Yazaki with their assistance in this work.

Financial Disclosure

Anna M. Wu is a shareholder and consultant to ImaginAb, Inc.

References

[1] Knowles SM, Wu AM. Advances in immuno–positron emission tomography: antibodies for molecular imaging in oncology. *Journal of Clinical Oncology.* 2012;30(31):3884-3892.

[2] Ambrosini V, Fani M, Fanti S, Forrer F, Maecke HR. Radiopeptide imaging and therapy in Europe. *Journal of Nuclear Medicine.* 2011;52(Supplement 2):42S-55S.

[3] Graham MM, Menda Y. Radiopeptide imaging and therapy in the United States. *Journal of Nuclear Medicine.* 2011;52(Supplement 2):56S-63S.

[4] Larson SM, Pentlow KS, Volkow ND, et al. PET scanning of iodine-124-3F9 as an approach to tumor dosimetry during treatment planning for radioimmunotherapy in a child with neuroblastoma. *Journal of nuclear medicine: official publication, Society of Nuclear Medicine.* 1992;33(11):2020-2023.

[5] Mumprecht V, Honer M, Vigl B, et al. In vivo Imaging of inflammation-and tumor-induced lymph node lymphangiogenesis by immuno–positron emission tomography. *Cancer research.* 2010;70(21):8842-8851.

[6] Pillay V, Gan HK, Scott AM. Antibodies in oncology. *New biotechnology.* 2011;28(5):518-529.

[7] Jones PL, Gallagher BM, Sands H. Autoradiographic analysis of monoclonal antibody distribution in human colon and breast tumor xenografts. *Cancer Immunology, Immunotherapy.* 1986;22(2):139-143.

[8] Fujimori K, Covell DG, Fletcher JE, Weinstein JN. Modeling analysis of the global and microscopic distribution of immunoglobulin G, F (ab′) 2, and Fab in tumors. *Cancer research.* 1989;49(20):5656-5663.

[9] Dreher MR, Liu W, Michelich CR, Dewhirst MW, Yuan F, Chilkoti A. Tumor vascular permeability, accumulation, and penetration of macromolecular drug carriers. *Journal of the National Cancer Institute.* 2006;98(5):335-344.

[10] Langmuir VK, Mendonca HL, Woo DV. Comparisons between two monoclonal antibodies that bind to the same antigen but have differing affinities: uptake kinetics and 125I-antibody therapy efficacy in multicell spheroids. *Cancer research.* 1992;52(17):4728-4734.

[11] Thurber GM, Zajic SC, Wittrup KD. Theoretic criteria for antibody penetration into solid tumors and micrometastases. *Journal of Nuclear Medicine.* 2007;48(6):995-999.

[12] Weinstein J, Eger R, Covell D, et al. The Pharmacology of monoclonal antibodies. *Annals of the New York Academy of Sciences.* 1987;507(1):199-210.

[13] Adams GP, Schier R, McCall AM, et al. High affinity restricts the localization and tumor penetration of single-chain fv antibody molecules. *Cancer research.* 2001;61(12):4750-4755.

[14] Saga T, Neumann RD, Heya T, et al. Targeting cancer micrometastases with monoclonal antibodies: a binding-site barrier. *Proceedings of the National Academy of Sciences.* 1995;92(19):8999-9003.

[15] Dennis MS, Jin H, Dugger D, et al. Imaging tumors with an albumin-binding Fab, a novel tumor-targeting agent. *Cancer research.* 2007;67(1):254-261.

[16] Minchinton AI, Tannock IF. Drug penetration in solid tumours. *Nature Reviews Cancer.* 2006;6(8):583-592.

[17] Thurber GM, Schmidt MM, Wittrup KD. Factors determining antibody distribution in tumors. *Trends in pharmacological sciences.* 2008;29(2):57-61.

[18]. Huang S-C, Phelps ME. Principles of Tracer Kinetic Modeling in Positron Emission Tomography and Autoradiography. In: Phelps M, Mazziotta J, Schelbert H, eds. *Positron Emission Tomography and Autoradiography: Principles and Applications for the Brain and Heart*. New York: Raven Press; 1986:287-346.

[19] Graff CP, Wittrup KD. Theoretical analysis of antibody targeting of tumor spheroids importance of Dosage for penetration, and affinity for retention. *Cancer research.* 2003;63(6):1288-1296.

[20] Kenanova V, Olafsen T, Crow DM, et al. Tailoring the pharmacokinetics and positron emission tomography imaging properties of anti–carcinoembryonic antigen single-chain Fv-Fc antibody fragments. *Cancer research.* 2005;65(2):622-631.

[21] Wu AM, Senter PD. Arming antibodies: prospects and challenges for immunoconjugates. *Nature biotechnology.* 2005;23(9):1137-1146.

[22] Wu AM. Antibodies and antimatter: the resurgence of immuno-PET. *Journal of Nuclear Medicine.* 2009;50(1):2-5.

[23] Lepin EJ, Leyton JV, Zhou Y, et al. An affinity matured minibody for PET imaging of prostate stem cell antigen (PSCA)-expressing tumors. *European journal of nuclear medicine and molecular imaging.* 2010;37(8):1529-1538.

[24] Knowles SM, Zettlitz KA, Tavaré R, et al. Quantitative immunoPET of prostate cancer xenografts with 89Zr-and 124I-labeled anti-PSCA A11 minibody. *Journal of Nuclear Medicine.* 2014;55:452-459.

[25] Han K-R, Seligson DB, Liu X, et al. Prostate stem cell antigen expression is associated with gleason score, seminal vesicle invasion and capsular invasion in prostate cancer. *The Journal of urology.* 2004;171(3):1117-1121.

[26] Reiter RE, Gu Z, Watabe T, et al. Prostate stem cell antigen: a cell surface marker overexpressed in prostate cancer. *Proceedings of the National Academy of Sciences.* 1998;95(4):1735-1740.

[27] Zhigang Z, Wenlv S. Prostate stem cell antigen (PSCA) expression in human prostate cancer tissues and its potential role in prostate carcinogenesis and progression of prostate cancer. *World Journal of Surgical Oncology.* 2004;2(1):13. (7 pages).

[28] Leyton JV, Olafsen T, Lepin EJ, et al. Humanized radioiodinated minibody for imaging of prostate stem cell antigen–expressing tumors. *Clinical Cancer Research.* 2008;14(22):7488-7496.

[29] Olafsen T, Gu Z, Sherman MA, et al. Targeting, imaging, and therapy using a humanized antiprostate stem cell antigen (PSCA) antibody. *Journal of Immunotherapy.* 2007;30(4):396-405.

[30]. Olafsen T, Kenanova VE, Wu AM. Tunable pharmacokinetics: modifying the in vivo half-life of antibodies by directed mutagenesis of the Fc fragment. *Nature Protocols.* 2006;1:2048-2060.

[31] Bao Q, Newport D, Chen M, Stout DB, Chatziioannou AF. Performance evaluation of the inveon dedicated PET preclinical tomograph based on the NEMA NU-4 standards. *Journal of Nuclear Medicine.* 2009;50(3):401-408.

[32] Loening AM, Gambhir SS. AMIDE: a free software tool for multimodality medical image analysis. *Molecular imaging.* 2003;2(3):131-137.

[33] van Dongen GA, Visser GW, Lub-de Hooge MN, De Vries EG, Perk LR. Immuno-PET: a navigator in monoclonal antibody development and applications. *The Oncologist.* 2007;12(12):1379-1389.

[34] Goodwin DA. Pharmacokinetics and antibodies. *Journal of Nuclear Medicine.* 1987;28(8):1358-1362.

[35] Deri MA, Zeglis BM, Francesconi LC, Lewis JS. PET imaging with 89Zr: From radiochemistry to the clinic. *Nuclear Medicine and Biology.* 2013;40:3-14.

Figures and Tables

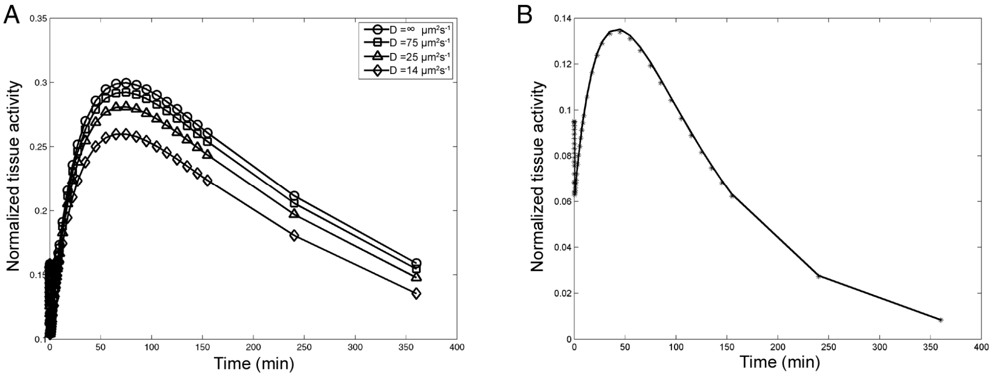

FIGURE 1. Results of Simulated Diffusion-Limited Time Activity Curves (A) Effect of diffusion rates on simulated TAC. (B) Fitting of *in silico* TAC (D=14 $\mu m^2 s^{-1}$) using a compartmental model (D = ∞ $\mu m^2 s^{-1}$). Data is normalized to steady-state receptor concentration in tissue.

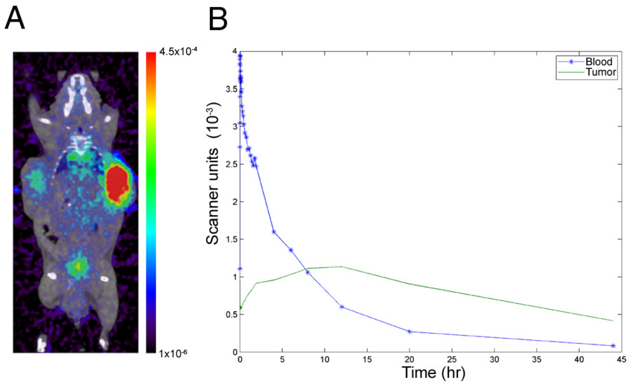

FIGURE 2. Results of *in vivo* Imaging of A11 Minibody. (A) PET-CT of mouse at 20h post injection with 22rv1 tumor on left and 22rv1xPSCA on the right side. Color bar is in scanner units. (B) Measured TAC from PSCA-positive tumor (green), and from left ventricle with fitted curve (blue).

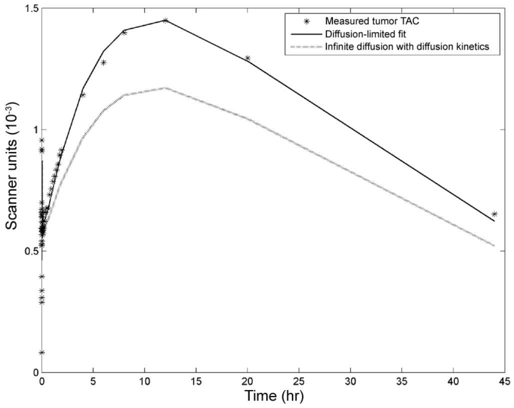

FIGURE 3 Fitting Results of Diffusion-Limited Model. Measured tumor activity fit using the diffusion model is shown as a solid line. A simulated TAC with parameters from the diffusion model fit, but using infinite diffusion, is shown as the dotted line.

TABLE 1 : Mean Bias and Relative Standard Deviation (RSD) of Parameters Fit to Simulated Diffusion-Limited Data.

Fitting Model		k_1 (k_{on})	k_2 (k_{off})	k_3	k_4	P	V_b
Compartmental (No Priors)	μ	3100%	$1*10^6$%	2090%	1660%	63%	13%
	RSD	76%	180%	910%	860%	61%	28%
Compartmental (With Priors)	μ	210%	470%	$1.5*10^4$%	$1.7*10^3$%	-7%	6%
	RSD	100%	200%	340%	500%	16%	42%
Diffusion (No Priors)	μ	31%	-30%	290%	10%	25%	8%
	RSD	150%	140%	180%	16%	110%	25%
Diffusion (With Priors)	μ	1%	-20%	210%	4%	6%	-6%
	RSD	46%	110%	170%	8%	18%	3%

TABLE 2: Parameter Values Estimated from Measured TACs.

Model	k_{on} $(M\cdot s)^{-1}$	k_{off} $(s)^{-1}$	k_3 $(s)^{-1}$	k_4 $(s)^{-1}$	P (m/s)	V_b	[Ag] (nM)	D ($\mu m^2/s$)
Compartmental (Mouse1)	$4.1*10^4$	$5.3*10^{-4}$	$7.7*10^{-6}$	$5.1*10^{-6}$	$4.4 *10^{-9}$	.17	1031	NA
Diffusion (Mouse1)	$1.6*10^5$	$2.1*10^{-4}$	$1.1*10^{-5}$	$6.9*10^{-6}$	$3.7*10^{-9}$	.16	140	9
Diffusion (Mouse2)	$1.8*10^5$	$4.4*10^{-4}$	$2.6*10^{-5}$	$8.1*10^{-6}$	$3.7*10^{-9}$	.10	161	10
% Difference between compartmental and diffusion models	-74%	152%	-30%	-26%	19%	6%	646%	N/A

Supplemental Data 2

Derivation of Kinetic Models

Motivation

In a standard compartmental model, transport of a tracer between well-mixed compartment is modeled as a series of ordinary differential equations (ODEs). However, in the case of heterogeneously localized tracers, these compartments are no longer well-mixed, and the spatial concentration of the tracer must be modeling within each compartment. This effectively leads to a set of linked compartmental models at each location in tissue (Supplemental Figure S2.4). In the case of tracer kinetics within tumors, it is natural to model this heterogeneous localization as diffusion of tracer away from the capillary wall into tissue in a radially symmetric fashion. Therefore, in the case of diffusion-limited tracers, we model tissue as a collection of identical cylinders, each with a central capillary enervating the tissue within that cylinder. The problem can be further simplified, by only examining 2-D slices if tissue (orthogonal to the capillary), as there will be no net diffusion between such slices. By converting equations to a radially symmetric geometry, we can thus reduce the system to a single spatial dimension.

1 - General Model Form - Linear Binding Kinetics

We examine radially symmetric diffusion of our compound. Let $u(r,t)$ = unbound compound, $v(r,t)$ = bound compound, and $w(r,t)$ = compound internalized into the cell. We then assume the following about our system:

(i) Plasma concentration of the compound is $C_p(t)$.

(ii) Compound moves reversibly into/out of the tissue at a rate defined by the capillary permeability, P.

(iii) The compound binds/unbinds to surface receptors at rates k_1, k_2, respectfully.

(iv) The bound compound is reversibly endo/exocytosed at rates k_3, k_4.

(v) The internalized compound is irreversibly metabolized out of the system at rate k_5.

(vi) Lastly, the compound diffuses linearly through tissue at rate D.

In the case of infinitely fast diffusion (i.e. classical compartmental model), we can the describe the system with the following set of ODEs.

$$\begin{aligned} &\frac{d}{dt}u(t) = PCp(t) - (k_1 + P)u(t) + k_2v(t) \\ &\frac{d}{dt}v(t) = k_1u(r,t) + k_4w(t) - (k_2 + k_3)v(t) \\ &\frac{d}{dt}w(t) = k_3v(r,t) - (k_4 + k_5)w(t) \end{aligned} \tag{S2.1}$$

In the case of finite diffusion rates, the following set of PDEs describe the system.

$$\begin{aligned} &\frac{\delta}{\delta t}u(r,t) = D[\frac{\delta^2}{\delta r^2}u(r,t) + \frac{1}{r}\frac{\delta}{\delta r}u(r,t)] - k_1u(r,t) + k_2v(r,t) \\ &\frac{\delta}{\delta t}v(r,t) = k_1u(r,t) + k_4w(r,t) - (k_2 + k_3)v(r,t) \\ &\frac{\delta}{\delta t}w(r,t) = k_3v(r,t) - (k_4 + k_5)w(r,t) \end{aligned} \tag{S2.2}$$

For the PDE system, two Neumann boundary conditions are required:

$$\begin{aligned} &-D\frac{\delta}{\delta r}u(r,t)]\big|_{r=r_0} = PC_p(t) - Pu(r_0,t) \\ &\frac{\delta}{\delta r}u(R,t) = 0 \end{aligned} \tag{S2.3}$$

The first corrects for the rate of influx/eflux of tracer from the capillaries which are centered at $r = 0$ and have radius r_0. The second corrects for diffusion of tracer out of the radius $r = R$ disc. Mathematically this actually manifests as a "reflective boundary" but we can think of it as correcting for influx from adjacent discs. This is not exactly correct as not all points on the discs are radius $r = R$ from two capillaries. However, this should still give the analytically correct result as we integrate over the disc because diffusion and compartmental transport are constant over radii, so in this formulation we are doing the same thing as integrating over all $r > r_0$ with no boundary condition on the outer radius.

2 - Solving the General Form

No analytical solution to the PDEs described above in equation S2.2 exist in the time domain. However, by applying a Laplace transform, an analytical solution is yielded.

Applying the Laplace transform yields the following differential equations.

$$
\begin{aligned}
s\hat{u}(r,s) &= D[\frac{\delta^2}{\delta r^2}\hat{u}(r,s) + \frac{1}{r}\frac{\delta}{\delta r}\hat{u}(r,s)] - k_1\hat{u}(r,s) + k_2\hat{v}(r,s) \\
s\hat{v}(r,s) &= k_1\hat{u}(r,s) + k_4\hat{w}(r,s) - (k_2+k_3)\hat{v}(r,s) \\
s\hat{w}(r,s) &= k_3\hat{v}(r,s) - (k_4+k_5)\hat{w}(r,s)
\end{aligned}
\tag{S2.4}
$$

We begin our solution by simplifying the algebraic relation between $\hat{u}(r,s), \hat{v}(r,s), and \hat{w}(r,s)$

$$\boxed{\hat{w}(r,s) = \frac{k_3}{s+k_4+k_5}\hat{v}(r,s) = C_w\hat{v}(r,s)}$$

$$\rightarrow s\hat{v}(r,s) = k_1\hat{u}(r,s) + k_4C_w\hat{v}(r,s) - (k_2+k_3)\hat{v}(r,s)$$

$$\rightarrow \hat{v}(r,s)[s+k_2+k_3-k_4C_w] = k_1\hat{u}(r,s)$$

$$\rightarrow \boxed{\hat{v}(r,s) = \frac{k_1}{s+k_2+k_3-k_4C_w}\hat{u}(r,s) = C_v\hat{u}(r,s)}$$

$$D[\frac{\delta^2}{\delta r^2}\hat{u}(r,s) + \frac{1}{r}\frac{\delta}{\delta r}\hat{u}(r,s)] - (s+k_1-k_2C_v)\hat{u}(r,s) = 0$$

$$\rightarrow r^2\frac{\delta^2}{\delta r^2}\hat{u}(r,s) + r\frac{\delta}{\delta r}\hat{u}(r,s) - r^2C_s^2\hat{u}(r,s) = 0$$

$$\text{Where } \boxed{C_s^2 = \frac{1}{D}(s+k_1-k_2C_v)} \tag{S2.5}$$

The resulting simplified equation can be solved more easily after applying a change a variables: $\rho = rC_s$

$$\rho^2 \frac{1}{C_s^2} \frac{\delta^2}{\delta r^2} \hat{u}(\rho, s) + \rho \frac{1}{C_s} \frac{\delta}{\delta r} \hat{u}(\rho, s) - \rho^2 \hat{u}(\rho, s) = 0$$

$$\rightarrow \rho^2 (\frac{dr}{d\rho})^2 \frac{\delta^2}{\delta r^2} \hat{u}(\rho, s) + \rho \frac{dr}{d\rho} \frac{\delta}{\delta r} \hat{u}(\rho, s) - \rho^2 \hat{u}(\rho, s) = 0$$

$$\rightarrow \rho^2 \frac{\delta^2}{\delta \rho^2} \hat{u}(\rho, s) + \rho \frac{\delta}{\delta \rho} \hat{u}(\rho, s) - \rho^2 \hat{u}(\rho, s) = 0$$

$$\rightarrow \boxed{\hat{u}(r, s) = \alpha(s) I_0(rC_s) + \beta(s) K_0(rC_s)} \tag{S2.6}$$

As shown in equations S2.6, $\hat{u}(\rho, s)$ is a sum of modified Bessel functions of order zero : $\hat{u}(\rho, s) = \alpha(s) I_0(\rho) + \beta(s) K_0(\rho)$, where $\alpha(s), \beta(s)$ are constant in r and will be defined by our boundary conditions.

3 - Solving the Boundary Conditions

At the $r = R$ boundary, the Laplace transform yields:

$$\frac{\delta}{\delta r} u(R, t) = 0 \rightarrow \alpha(s) C_s I_1(RC_s) - \beta(s) C_s K_1(RC_s) = 0$$

$$\rightarrow \boxed{\beta(s) = \alpha(s) \frac{I_1(RC_s)}{K_1(RC_s)} = \alpha(s) I_K}$$

$$\text{Where} \boxed{I_K = \frac{I_1(RC_s)}{K_1(RC_s)}} \tag{S2.7}$$

Taking the Laplace transform of the $r = r_0$ boundary condition yields the following:

$$-D \frac{\delta}{\delta r} \hat{u}(r, t)\Big|_{r=r_0} = P\hat{C}_p(t) - P\hat{u}(r_0, s)$$

$$\boxed{\frac{d}{dr} I_0(rC_s) = C_s I_1(rC_s) \qquad \frac{d}{dr} K_0(rC_s) = -C_s K_1(rC_s)}$$

$$\rightarrow D\alpha(s) C_s [I_K K_1(r_0 C_s) - I_1(r_0 C_s)] = P\hat{C}_p(s) - P\alpha(s)[I_0(r_0 C_s) + K_0(r_0 C_s)]$$

$$\boxed{\alpha(s) = \frac{P\hat{C}_p(s)}{DC_s[I_K K_1(r_0 C_s) - I_1(r_0 C_s)] + P[I_0(r_0 C_s) + I_K K_0(r_0 C_s)]}} \tag{S2.8}$$

4 - Infinite Diffusion Limit

We want to make sure this correctly model behavior in the infinitely fast diffusion limit (the standard compartmental model). In Laplace space, the solution to the comparable compartmental model is,trivially, as follows:

$$\hat{w}(s) = C_w v(s)$$

$$\hat{v}(s) = C_v u(s)$$

$$\boxed{\hat{u}(s) = \frac{\tilde{P}\hat{C}_p(s)}{s + \tilde{P} + k_1 - C_v k_2}}$$

$$\tilde{P} = (2\pi r_0)\frac{P}{\pi(R^2 - r_0^2)} \tag{S2.9}$$

With C_w, C_v defined as above. Here $\tilde{P}$is modified to correct for the differences between this "compartmental" model and the radially symmetric "Diffusion Model". The $\frac{1}{\pi(R^2-r_0^2)}$ term is to correct for the fact that with infinite diffusion, transport in/out of tissue to/from capillaries is placed evenly across all radii, so influx and efflux are reduced by a factor proportional to the area enervated by the capillary in question. The $(2\pi r_0)$ is to correct for the fact that in the "Diffusion" model, P is a measure of flux across an infinitesimal point on the capillary wall, but in the "Compartmental" model it refers to the net-flux across the entire circumference of the capillary.

In the $D \to \infty, C_s \to 0$ limit, the solution from part 3 (Eqs. S2.6-S2.8) should simplify to the above solution (Eqs. S2.9).

In the large D, small C_s limit, we have the following asymptotic approximations for the modified bessel functions:

$$\boxed{\begin{aligned} \lim_{z\to 0} I_0(z) &\sim 1 \\ \lim_{z\to 0} I_1(x) &\sim \frac{z}{2} \\ \lim_{z\to 0} K_0(z) &\sim -ln(z) \\ \lim_{z\to 0} K_1(z) &\sim \frac{1}{z} \end{aligned}}$$

$$\rightarrow \boxed{\lim_{C_s\to 0} \quad I_K = \lim_{C_s\to 0} \frac{I_1(RC_s)}{K_1(RC_s)} = \frac{RC_s}{2(RC_s)^{-1}} = \frac{(RC_s)^2}{2}}$$

We can then use this information to get an asymptotic estimate of $\alpha(s)$ is in the large D limit:

$$\lim_{C_s\to 0} \quad \alpha(s) = \lim_{C_s\to 0} \frac{P\hat{C}_p(s)}{DC_s[\frac{(RC_s)^2}{2}\frac{1}{r_0 C_s} - \frac{r_0 C_s}{2}] + P[1 - \frac{(RC_s)^2}{2} ln(r_0 C_s)]} = \frac{P\hat{C}_p(s)}{\frac{DC_s^2}{2r_0}[R^2 - r_0^2] + P}$$

$$\rightarrow \lim_{C_s\to 0} \quad \alpha(s) = \frac{\frac{P}{[R^2-r_0^2]}\hat{C}_p(s)}{\frac{1}{2r_0}(s + k_1 - k_2 C_v) + \frac{P}{[R^2-r_0^2]}} = \frac{\tilde{P}\hat{C}_p(s)}{s + \tilde{P} + k_1 - k_2 C_v}$$

$$\rightarrow \lim_{D\to\infty} \hat{u}(r,s) = \lim_{D\to\infty} \alpha(s)[I_0(rC_s) + I_K K_0(rC_s)] = \lim_{D\to\infty} \alpha(s)[1 - \frac{(RC_s)^2}{2} ln(rC_s)] = \lim_{D\to\infty} \alpha(s)$$

$$\lim_{D\to\infty} \alpha(s) = \lim_{C_s\to\infty} \alpha(s) = \boxed{\frac{\tilde{P}\hat{C}_p(s)}{(s + \tilde{P} + k_1 - k_2 C_v)}}$$

Thus, the model specified by Eqs. S2.2-S2.3 converges to the standard compartmental model (Eqs. S2.1) in the infinite diffusion limit, as specified by Eqs. S2.9.

5 - General Model Form - Nonlinear Binding Kinetics

As mentioned in the main body, linear binding kinetics will not always be sufficient for describing the system *in vivo*. To describe such a system, we build equations with assumptions similar to those specified in section 1. However, in addition to modeling the concentrations of tracer in extracellular space ($u(r,t)$), bound to the surface ($v(r,t)$), and internalized within the cell ($w(r,t)$), we now also track the concentration of open binding sites on the cell surface ($x(r,t)$). In this system we make the following assumptions, which result in Eqs. S2.10 & S2.11.

(i) Plasma concentration of the compound is $C_p(t)$.

(ii) Compound moves reversibly into/out of the tissue at a rate defined by the capillary permeability, P.

(iii) The compound binds/unbinds nonlinearly to surface receptors at rates k_1, k_2, respectfully.

(iv) Surface receptors have a steady state concentration of $dens_0$.

(v) The concentration of open receptors returns asymptotically to steady state at maximum rate of k_{regen} (at complete saturation), such that the steady state regeneration (in absence of ligands) will be: $\frac{\delta}{\delta t}x(r,t) = k_{regen}(dens_0 - x(r,t))$.

(vi) The bound compound/receptor complex is reversibly endo/exocytosed at rates k_3, k_4.

(vi) The internalized compound is irreversibly metabolized out of the system at rate k_5.

(vii) Lastly, the compound diffuses linearly through tissue at rate D.

In the case of infinitely fast diffusion (i.e. classical compartmental model), we can the describe the system with the following set of non-linear ODEs.

$$\begin{aligned}
\frac{d}{dt}u(t) &= PCp(t) - Pu(t) - k_1u(t)x(t) + k_2v(t) \\
\frac{d}{dt}v(t) &= k_1u(t)x(t) + k_4w(t) - (k_2 + k_3)v(t) \\
\frac{d}{dt}x(t) &= -k_1u(t)x(t) + k_2v(t) + k_{regen}(dens_0 - x(t)) \\
\frac{d}{dt}w(t) &= k_3v(t) - (k_4 + k_5)w(t)
\end{aligned} \tag{S2.10}$$

In the case of finite diffusion rates, the following set of non-linear PDEs describe the system.

$$\begin{aligned}
\frac{\delta}{\delta t}u(r,t) &= D[\frac{\delta^2}{\delta r^2}u(r,t) + \frac{1}{r}\frac{\delta}{\delta r}u(r,t)] - k_1u(r,t)x(r,t) + k_2v(r,t) \\
\frac{\delta}{\delta t}v(r,t) &= k_1u(r,t)x(r,t) - (k_2 + k_3)v(r,t) \\
\frac{\delta}{\delta t}x(r,t) &= -k_1u(r,t)x(r,t) + k_{regen}(dens_0 - x(r,t)) + k_2v(r,t) \\
\frac{\delta}{\delta t}w(r,t) &= k_3v(r,t) - (k_4 + k_5)w(r,t)
\end{aligned} \tag{S2.11}$$

The model described in Eqs. S2.11 is subject to the same Neumann boundary constraints described in Eq. S2.3 for the linear binding-kinetic model. Unlike the linear-binding scenario, the inclusion of nonlinear binding kinetics precludes analytical solutions in both the time and Laplace domain. Therefore, all solutions to these equations must be computed numerically.

6 - Computing Numerical Solutions

As analytical solutions to the linear binding model are readily available in the Laplace domain, solutions to these equations were computed using a numerical Laplace inversion. The solutions described in section 3 were inverted using De Hoog's numerical Laplace inversion [1], as implemented for MATLAB by Hollenbeck [2]. Time activity curves were simulated by numerically inverting solutions to the Eqs. S2.2, and integrating the activities across radii. Solutions to Eqs. S2.11 were computed by applying the method of lines to discretize the spatial dimension, and numerically solving the resulting system with Runge-Kutta methods as implemented in MATLAB.

7 - Optimization Algorithm

In kinetic modeling, the goal is often to obtain a non-linear regression fit $f(t|\theta)$ of the measured time activity curve $y(t)$. This is usually computed by minimizing a weighted sum of squares, as defined in (S2.12), where the weightings w_i^2 are proportional to the variance (σ_i^2) of each measurement $y(t_i)$. If these $y(t_i)$'s are distributed as members of exponential families (under mild assumptions), then this minimized sum of squared errors is directly equivalent to a maximum likelihood fit, with the weights w_i described by the standard deviation of those distributions [3].

$$\min_{\theta} \sum_{i=1}^{n} \frac{[y(t_i) - f(t_i|\theta)]^2}{w_i^2} \tag{S2.12}$$

In the optimization used in this work, we also add two new terms to the sum in (S2.12) to account for prior information measured *in vitro* ($\bar{k}_{on}$ and $\bar{k}_{off}$), as shown in (S2.13). In the optimization performed in this work, both w_{on} and w_{off} are set to $\frac{ln(10)}{2}$, such that $log(k_{on/off})$ are normally distributed with 95 percent of the probability density function contained within 1 order of magnitude above and below the mean. Although we are able to obtain far greater confidence in *a priori* measurements of these parameters, weak priors were used to avoid over-constraining the model fit.

$$\min_{\theta} \left(\sum_{i=1}^{n} \frac{[y(t_i) - f(t_i|\theta)]^2}{w_i^2}\right) + \frac{[ln(\bar{k}_{on}) - ln(\theta_{k_{on}})]^2}{w_{on}^2} + \frac{[ln(\bar{k}_{off}) - ln(\theta_{k_{off}})]^2}{w_{off}^2} \tag{S2.13}$$

This penalized weighted sum of squares (equivalent to a maximum likelihood estimate with Bayesian priors) was solved using the Levenberg-Marquardt optimization method. The weightings for PET measurements w_i were defined as in (S2.14), with the standard deviation of the measurements at time t_i proportional to the inverse of the duration of the relevant PET frame. The parameter α (identical for all w_i) was chosen experimentally to reproduce the level of noise seen in the data. In many PET applications, this weighting parameter is also defined to be proportional to the true data at time t_i. However, that correction is more applicable in cases where images have been reconstructed iteratively, as opposed to the filtered back projection used in this case.

$$w_i^2 = \frac{\alpha}{\text{duration}_i^2} \tag{S2.14}$$

8 - Confidence Intervals of Parameter Estimates

In optimization methods such as Levenberg-Marquardt, confidence intervals for parameter estimates can be obtained from the parameter covariance matrix V_θ, which is a function of the Jacobian (J) of the regression function ($f(t, |\theta)$), and the diagonal weighting matrix (W) (Eq. S2.15).

$$V_\theta = [J^T W J]^{-1} \tag{S2.15}$$

These estimates will be highly dependant on the weighting matrix W, and although we can make robust estimates on the variance of measured time activity curve, the true variance of the *a priori* measurements are more difficult to define. Without the priors ($w_{on/off} = 0$), the confidence intervals of the fitted parameters will clearly be quite large (in line with the lack of parameter identifiability without priors in fitting). Therefor we report the CIs of the fitted parameters at several levels of theoretical variance for the *in vitro* measurements.

In all cases we assume that distribution of the *a priori* parameter measurements are log-Normal, varying only in standard deviation. While a weighting of $\frac{ln(10)}{2}$ was used in fitting to avoid over-constraining the fitting algorithm, clearly there is stronger confidence in the *in vitro* measurements. Therefor, we report RSD estimates using standard deviations down to $\frac{ln(2)}{4}$, relating to a prior probability density function with ~95% if its mass between 70% and 140% of the mean. In Table S2.1 the relative standard deviation of the parameter fits from "mouse 1" in the work above are shown as functions of the confidence placed in the *a priori* measurements.

While the confidence of most parameter estimates can be greatly increased through more realistic bounds on the accuracy of *a priori in vitro* measurements, we see little improvement in confidence of the fitted values for k_{regen}, P or R. In the case of capillary permeability,P, and blood volume, $\frac{1}{\mathrm{R}^2}$, this small change in improvement is likely due to the small covariance between these parameters and the binding/unbinding rates of the minibody. This is in alignment with *in silico* and *in vivo* fitting results showing relatively small differences in those estimates when fitting data with compartmental vs. diffusion-limited models. In the case of k_{regen}, it is possible that this confidence could be increased through experiments specifically designed to reach higher levels of receptor saturations, where the net regeneration rate is farther away from its asymptotic value as described by Eq. S2.11.

Table S2.1 Relative Standard Deviation of Parameter Estimates with Varying Levels of *in vitro* Noise. (Data shown is in percent values).

$\sqrt{\text{Prior weights}}$	k_{on}	k_{off}	k_{regen}	k_{endo}	P	D	$dens_0$	R
$\frac{1}{\infty}$	7980	6370	3720	2410	35.6	6.125	618	2.82
$\frac{ln(10)}{2}$	115	115	2220	206	12.5	2.82	26.3	2.39
$\frac{ln(10)}{4}$	57.6	57.6	2220	205	12.5	2.81	25.5	2.39
$\frac{ln(2)}{2}$	34.7	34.7	2220	205	12.5	2.81	25.3	2.39
$\frac{ln(2)}{4}$	17.3	17.3	2220	204	12.5	2.81	25.2	2.39

References

1. De Hoog FR, Knight J, Stokes A. An improved method for numerical inversion of Laplace transforms. *SIAM Journal* on Scientific and Statistical Computing. 1982;3(3):357-366.

2. Hollenbeck, K. J. (1998) INVLAP.M: A matlab function for numerical inversion of Laplace transforms by the de Hoog algorithm, http://www.isva.dtu.dk/staff/karl/invlap.htm

3. Charnes A, Frome E, Yu P-L. The equivalence of generalized least squares and maximum likelihood estimates in the exponential family. Journal of the American Statistical Association. 1976;71(353):169-171.

Supplemental Figures

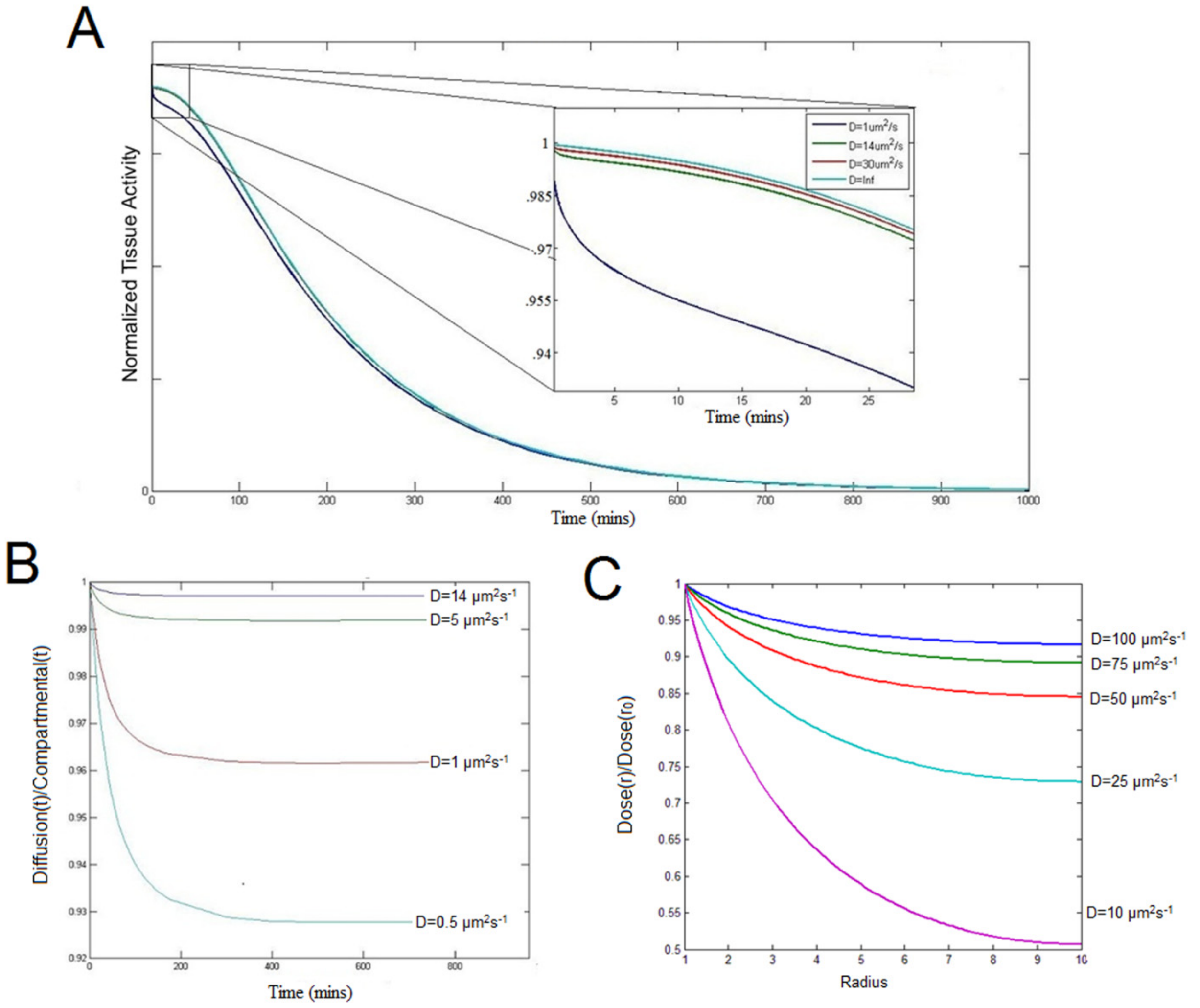

SUPPLEMENTAL FIGURE S2.1. Effects of Diffusion on TACs and Dose-at-Depth in Linear Binding Models. (A) Simulated TAC in response to unit impulse at different rates of diffusion. Curves are normalized by the maximum simulated value from the infinite diffusion curve. (B) Ratio of simulated TACs at different diffusion rates to an infinite diffusion model. Even at biologically unreasonable rates ($D=1\mu m^2 s^{-1}$), differences are less than 5%. (C) Total dose at depth relative to dose at capillary wall as a funciton of diffusion rates.

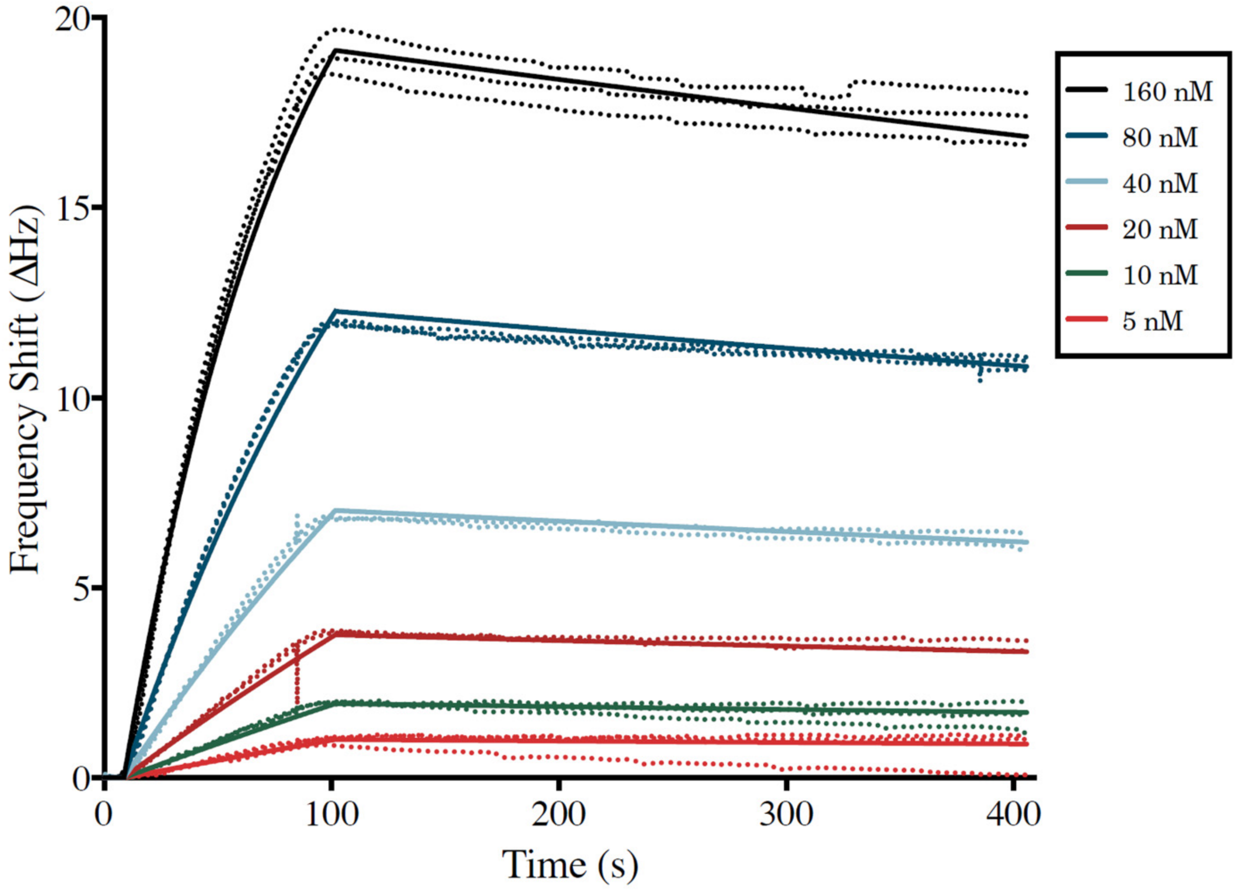

	k_{on} ($M^{-1}s^{-1}$)	k_{off} (s^{-1})	B_{Max}	K_D (nM)
A11 Minibody	1.21×10^{5}	4.95×10^{-4}	25.27	4.14

SUPPLEMENTAL FIGURE S2.2. Affinity Measurements of A11 minibody: Immobilized PSCA antigen as measured by quartz crystal microbalance. Bold line is the mass transport limited binding model fit from n = 3 measurements at each concentration (160-5 nM), shown as dotted lines).

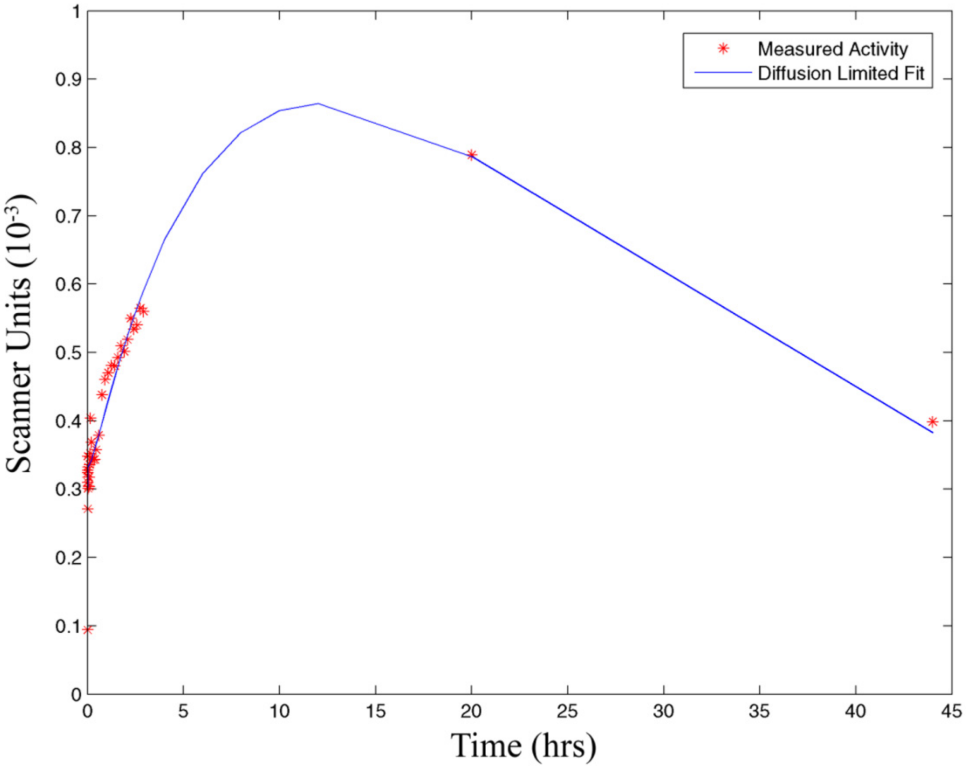

SUPPLEMENTAL FIGURE S2.3. Fitting of TAC Measured from 22Rv1xPSCA Tumor in Second Mouse Using Diffusion-Limited Model with Bayesian Priors.

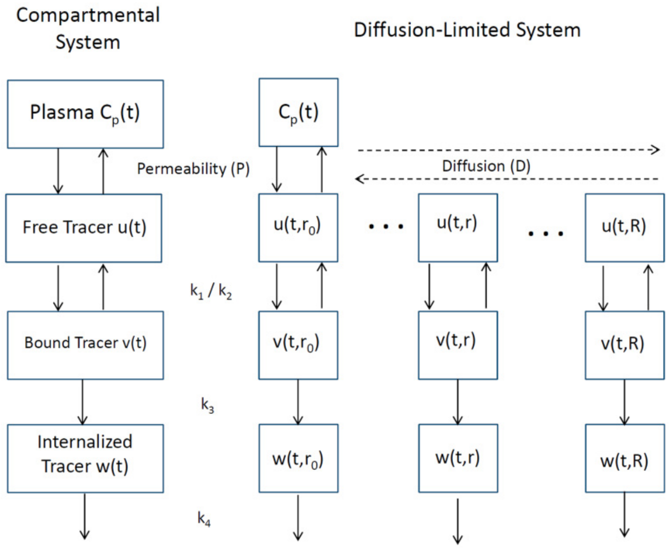

SUPPLEMENTAL FIGURE S2.4. Illustration of Difference Between a Standard Compartmental Model and the Diffusion-Limited Case.

CHAPTER 5 - Summary and Future Work

Abstract

The work presented in this dissertation represents solutions to overcoming barriers to quantification in positron emission tomography. This work in Chapters 2&3 has shown that automated image measurement and analysis can greatly increase the quantitative utility of neurologic PET data in Alzheimer's disease (AD) for both diagnostic and prognostic purposes. Future work should be performed to further validate these methods with respect to a larger and more diverse subject population. These methods can also be extended upon in further improvements to Alzheimer's imaging for both FDDNP and other β-amyloid and NFT tracers. Lastly, there are a multitude of non-Alzheimer dementias and other neurological conditions which could be investigated with improved quantitatively with the methods presented here. In Chapter 4, we have shown that more rigorous mathematical techniques are needed for accurate quantification of the pharmacokinetics of large-molecule PET tracers such as labeled-antibodies. Many future studies can be performed to extend this work, namely in developing shorter scan protocols that can be more easily adapted to clinical investigations. In a similar vein, *in silico* simulation studies can be performed to rigorously play drug treatment protocols to assure needed dosages at all depths within target tissues.

5.1 Neurologic PET

5.1.1 Summary of Results

In Chapter 2 of this dissertation, we showed that through automated VOI generation, the diagnostic utility of PET in AD can be greatly improved. Additionally, the regional data used for classification was highly conserved and related to early stages of pathological progression AD (the medial temporal lobe, posterior cingulate gyrus, and the occipital lobe) [1]. This provides initial evidence that quantitative PET can be used for non-invasive staging of AD *in vivo*. Extensions of this work are presented in Chapter 3, where we show that this automated data measurement can be improved in several ways. First, we can automatically perform parametric graphical methods, such as Logan or relative equilibrium analysis, removing more sources of possible inter- and intra-investigator variability and avoiding errors due to under sampling of reference regions [2-3]. We also show that quantification of AD-PET can be increased through more rigorous analysis of extracted data. Through automated VOI generation, we are able to robustly measure much larger regions than would be feasible through manual VOI definition. With larger VOIs, we are able to model extracted data more carefully and are not limited to assumptions of normally distributed tracer activity within a given region. In fact, modeling each region as an admixture distribution of healthy and diseased tissue greatly improves the predictive utility of the data, allowing for accurate models to be built for predicting the rate of pathological progression and cognitive decline over a two year period. The relatively poor performance seen by using mean-value measures to predict longitudinal changes perhaps explains the difficulty in creating predictive models, as previously described by other investigators in follow-up studies of FDDNP and ^{11}C-PIB [4]. Another advantage the analysis reported in Chapter 3 may have over previous AD-PET studies is the use of subcortical white matter as a reference [5]. We found evidence of increased binding of FDDNP in cerebellar cortex over the two year follow-up period, with some AD and MCI subjects showing large reductions in regional DVR values between initial and follow-up scans, which disappeared when using white-matter as a reference region instead, as described by Wong *et al.* [5]. This growth of amyloid deposition in the cerebellar gray matter has been previously found in *post* mortem examinations as well [6-7]. It is possible that a similar longitudinal increase in amyloid load in the cerebellar cortex explains the longitudinal decline in parametric image intensity seen in some subjects by Ossenkoppele *et al.* and Jack *et al*., as well as lack of strong correlation between regional image intensity and psychological scores such as the mini-mental-state examination (MMSE) [4,8].

5.1.2 Future Expansions

As discussed above, significant improvements can be made to AD-PET through more rigorous and quantitative analysis of data. However, there are still limitations of the techniques as presented in Chapters 2&3, and many possible extensions in imaging both AD, and non-Alzheimer dementias and disorders. Perhaps the largest current limitation to the methodology presented thus far, is that partial volume correction (PVC) was not performed. In our image analysis presented in Chapter 3, very conservative grey-matter masks were applied to our automatically generated VOIs, such that partial-volume effects should be minimized. However, in neurdegenerative diseases like AD, we will be measuring ever thinner anatomical regions, especially as disease progresses to late stages, increasing the likelihood of spill-over induced partial-volume errors and significant underestimation of amyloid and NFT load.

The importance of PVC in AD-PET has been previously described, and initial work has been published to perform PVC in FDDNP [9,10]. It is possible that any partial-volume effects are being absorbed by the admixture modeling described in Chapter 3, with spillover into white-matter being accounted for in the "healthy" tissue distribution. This possibility would explain the consistently higher variance seen in "healthy" vs. "diseased" tissue distributions found in the admixture modeling. If this is the case, PVC would likely improve discrimination between the distributions modeling the admixture analysis and perhaps further improve the longitudinal predictive utility of FDDNP PET in AD. To test for this possibility, future work will be performed to examine the sensitivity of the admixture modeling to cortical thickness in digital phantoms. If significant changes are measured across biologically reasonable levels of cortical degeneration, the current set of longitudinal data will be reanalyzed using PVC to account for these spill-over events. Because the automated protocol described in Chapters 2&3 requires a structural image of each subject, creating smoothed partial-volume effect masks should prove to be a very simple extension of the automation procedure.

Another area where this methodology can be expanded is with increased population sizes across a wider spectrum of disease states. As previously discussed, AD is a slowly progressing disease with pathological symptoms initiating long before clinically detectable symptoms present [1,11,12]. While we showed preliminarily promising results in longitudinal prediction and disease staging, a more complete model of disease progression could be built with long term data across more disease states than MCIs and age-matched controls. Therefore, an expanded study group and imaging protocol is proposed here. A population of clinically diagnosed AD, MCI, and age-matched controls would undergo annual examinations of mental state, as described by Small *et al.*, over a period of 2-4 years [13]. Further, at each of these examinations, subjects would undergo dynamic-FDDNP scanning, as described previously, as well as a T1-weighted (MPRage) MRI scan, so that cortical loss could be accounted for in VOI generation [10]. For all subjects, parametric FDDNP-DVR images would be automatically generated through relative equilibrium analysis, subjected to PVC [3]. These parametric images would then be measured and analyzed as described in Chapter 3 of this work, allowing for a more complete view of disease progression to be examined. This study could be further improved with the inclusion of young healthy controls (around 40 years old), with and without familial histories of dementia, in an attempt to view the progression on β-amyloid and NFTs in early disease state as well as in normal aging.

5.1.3 Future Extensions

As mentioned previously, there are currently various AD-PET tracers (for both amyloid and NFT imaging) being investigated, and it is possible that by extending the methods discussed here they would also show improved diagnostic and prognostic capabilities. An initial test of this hypothesis would be direct comparisons of ^{18}FDDNP scans with ^{11}C-PIB scans of the same subject population, to see if PIB shows the same admixture distribution of tracer activity seen in FDDNP. A significant complication to this study stems from the appearance in amyloid in the cerebellar cortex, as discussed above, making it an inappropriate reference region for generating parametric images such as DVR or SUVr [6,7]. While we have shown that using subcortical white matter is a solution to this problem, it has been noted that PIB, as well as other amyloid-only binding tracers such as AV-45 and BAY-94, exhibit increased localization in white matter as well[11,14,15]. This phenomenom limits the quantifiability of these tracers until a more robust reference region is found.

The methods described here can also be extended to non-Alzheimer's dementias and diseases, that are currently being investigated with FDDNP. In addition to AD, there are other dementias with characteristic amyloid accumulation, such as frontotemporal dementia (FTD), that could also be visualized with FDDNP [16]. Because clinical misdiagnosis of dementias is relatively common, *in vivo* assays of amyloid distributions *via* PET could allow for a significant improvement to clincial discrimination [17]. Additionally, the methods described here can be extended to visualization of amyloid or NFT in other degenerative diseases such as progressive supranuclear palsy, genetic conditions such as Down syndrome, or environmental conditions such as chronic traumatic brain injury [18-21].

5.2 Oncologic PET

5.2.1 Summary of Results

In Chapter 4, we presented work examining the limitations of using traditional ODE compartmental models to extract kinetic information about large, slowly diffusing radiotracers such as labeled antibodies. We showed that in a linear binding regime, measured TACs will not be significantly affected by biologically reasonable diffusion rates. However, even in the case of linear binding kinetics, non-infinite diffusion rates will lead to high levels of tissue heterogeneity, which will cause significant complications to immunotherapy protocols, with large volumes of target tissue being devoid of therapeutic effects [22]. Practical situations will likely diverge from the linear binding regime, due either to blocking or co-injection studies, low labeling efficiencies, or planned receptor saturation in the case of immunotherapy [23]. When binding deviates from linear to Michaelis-Menten kinetic regimes, we find that simulated TACs will be far more sensitive to slower diffusion rates of tracer compounds. Furthermore, we find that there are cases when these simulated TACs can be reasonably reproduced with infinite-diffusion (i.e. classic compartmental) models, leading to large parameter estimate bias. We also show that the resulting problem of parameter identifiability can be overcome by the inclusion of Bayesian priors on parameters that can be accurately measured *in vitro* before scanning.

Extending this *in silico* work to *in vivo* scanning of mice, we show that a diffusion-limited non-linear PDE model of tracer kinetics can accurately reproduce measured TACs of the ^{124}I-A11 minibody in tumors over-expressing the PSCA antigen [24]. Further mirroring the preliminary *in silico* simulations, we find that fitting these TACs with regular compartmental models can result in order-of-magnitude differences in parameter estimates from the diffusion limited model. In these cases, the diffusion-limited PDE models much more closely resembles the *a priori* parameter measurements performed *in vitro*.

5.2.2 Future Expansions

Although promising, the work presented in Chapter 4 is preliminary and requires to be expanded in several ways. First, the radiotracer discussed in Chapter 4, ^{124}I-A11, shows faster *in vivo* clearance times from target tissues. This is thought to be caused by the rapid cleavage and excretion of the ^{124}I tracer molecule once the bound minibody-receptor complex is internalized to the cell [25]. As a result, we presented a simplified model of A11 kinetics in which there is no intracellular compartment, and internalization is modeled as a leak from the system. While this has proven accurate thus far, there are other immunotracers and even forms of A11, such as ^{89}Zr-A11 for which the assumption of infinitely fast metabolism will not hold [26]. Therefore, the identifiability of diffusion limited models with intracellular compartments must be verified.

We have performed initial tests of this expanded model for *in vivo* imaging of the ^{89}Zr-A11 minibody. One mouse was implanted with a 22rv1 control tumor, and contralaterally with a 22rv1 tumor transfected to over-express PSCA, as described previously and in Chapter 4[27]. The mouse underwent a similar scanning protocol of an initiation 2h dynamic scan, followed by 10 minute static scans taken at 4, 6, 8, 12, 21, and 45 hours post injection. Using the same priors as the fittings in Chapter 4, the diffusion-limited PDE model was used to fit the extracted TAC from the transfected tumor (Figure 5.1). Parameter estimates from this model, as compared to the mice scanned in Chapter 4 are shown in Table 5.1. As can be seen in Figure 5.1 and Table 5.1, the diffusion limited model appears to be robust in its ability to reproduce more complicated kinetic models including intracellular compartments, with most of the parameter estimates being in close alignment with those found *in vitro* and *vivo*.

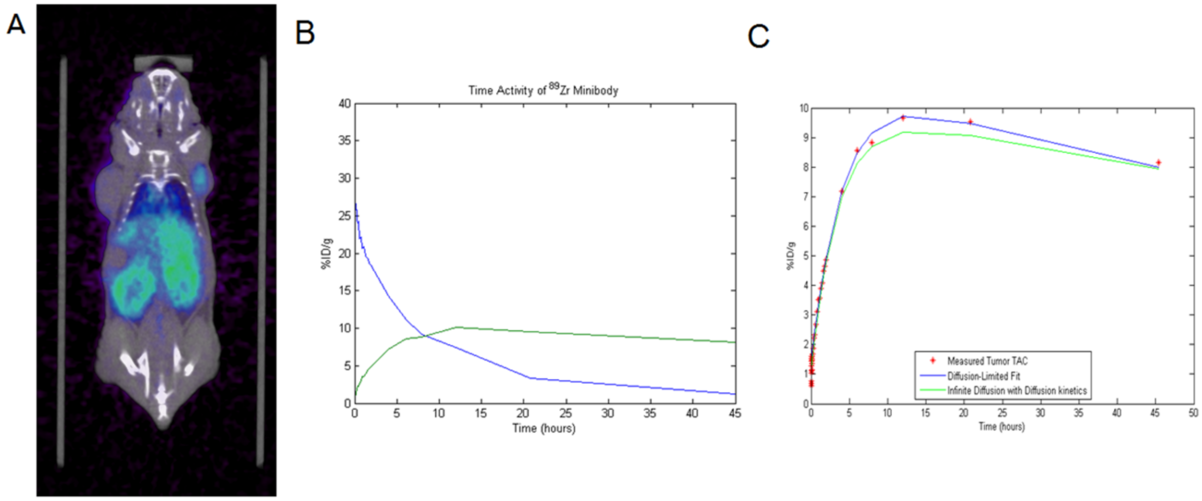

FIGURE 5.1: *In vivo* Scanning of ^{89}Zr-A11 Minibody in PSCA Expressing Tumors. (A) Fused PET-CT of mouse implanted with 22rv1 (left) and 22rv1xPSCA (right) tumors 8 hours post injection. (B) Measured TACs of blood (blue), and transfected tumor (green) activity. (C) Measured TAC(red) fit with the diffusion limited PDE model with intracellular compartments (Blue), and an infinite diffusion compartmental model with identical kinetic parameters (green).

TABLE 5.1 Parameter Estimates from Diffusion-Limited PDE Kinetic Models as Measured *in vivo* with ^{124}I and ^{89}Zr-A11 Minibodies. Parameter estimates for ^{89}Zr-A11 data are from a model including an intracellular compartment.

Model	Kd (nM)	k_{on} $(M\ s)^{-1}$	k_{off} (s^{-1})	K_{regen} (s^{-1})	K_{endo} (s^{-1})	K_{metab} (s^{-1})	P (m/s)	Vb	[Ag] nM	D $(\mu m^2/s)$
Prior	4.14	$1.2*10^{5}$	$4.95*10^{-4}$	-	-	-	-	-	-	-
^{124}I – Mouse 1	1.3	$1.6*10^{5}$	$2.1*10^{-4}$	$1.1*10^{-5}$	$6.9*10^{-6}$	-	$3.7*10^{-9}$	0.16	140	9
^{124}I – Mouse 2	2.4	$1.8*10^{5}$	$4.4*10^{-4}$	$2.6*10^{-5}$	$8.1*10^{-6}$	-	$3.7*10^{-9}$	0.10	161	10
^{89}Zr – Mouse 1	8.7	$9.3*10^{4}$	$8.1*10^{-4}$	$3.2*10^{-5}$	$3.1*10^{-5}$	$1.6*10^{-6}$	$2.5*10^{-8}$	0.04	95	7

While this data shows strong preliminary agreement between models and imaging agents, this methodology still requires further testing. Specifically, repeated study with largely expanded data sets can help to verify these initial results. In these expanded studies, it is proposed to repeat the scanning protocol using ^{124}I-A11 described in Chapter 4, but repeated with subcutaneous xenografts of cancer lines which express PSCA at differing concentrations, such as Capan1 (30K PSCA/cell), LAPC-9 (72K PSCA/cell), and the 22rv1xPSCA line used above and in Chapter 4 ($3*10^6$ PSCA/cell). This expansion will help verify the parameter estimates acquired using the diffusion limited model. This methodology can expanded for more robust quantification in a larger study in several ways. First, the imaging data shown above and in Chapter 4 was performed without attenuation correction. This was done primarily to keep in line with a proposed longitudinal treatment study, where repeated CT imaging would confound treatment effects. Additionally, in larger scale studies PVC should be performed to assure clean measurement of the input function. In this specific case, partial-volume effects are likely to be minimal due to the lack of PSCA expressed in cardiac tissue, but developing these methods for other tracers which do not share that property is an important extension of this methodology. Lastly, this model can be verified through comparisons to α-camera imaging of *ex vivo* cryosections of tissues labeled with an α-emitting minibodies. These α-camera images can have spatial resolution up to 35 μm, and initial studies have been performed with an α-emitting ^{211}At-A11 minibody showing heterogeneous localization[28,29]. These α-camera images can be used to verify the spatial heterogeneity predicted by the diffusion-limited kinetic model.

5.2.3 Future Extensions

One of the largest limitations of translating the small animal PET work shown here to clinical usage is the number and duration of PET scans currently required. However, in Chapter 4 we show that we can obtain similar parameter estimates using four fewer followup time points, suggesting that it is possible to extract the desired biological parameters using limited scan protocols. Once the optimization model is verified as discussed above, we plan to evaluate the identifiability of biological parameters under various study protocols. Time activity curves will be simulated (with noise added) using kinetic parameters acquired from *in vivo* imaging, for a variety of study protocols, varying in scan number and duration. Performance of these protocols will be evaluated on the basis of estimated parameter bias and variance. Initially, only protocols with a single dynamic scan taken immediately after injection will be analyzed. Afterward, we will progressively add simulated static followup scans, to determine performance gains. These simulated studies could also be used to help in the development of new custom engineered immunoPET probes. It is possible that under different combinations of kinetic parameters (such as binding affinity capillary permeability, etc.), more reliable parameter estimates could be extracted from dynamic PET imaging.

It is possible that no practical clinical protocol for kinetic PET imaging could be established for these tracers. However, this diffusion-limited model will still have utility in designing dosage protocols for immunotherapy. In future studies, we plan to simulate the kinetic activity of immunotherapeutics in tissue under a variety of dosage protocols. Similar to the *in silico* experiments discussed above, these simulations will be performed with kinetic parameters measured *a priori* using the diffusion limited kinetic model. These protocols will then be optimized such that they can deliver effective dosages to all depths within tumors, as well as minimizing dosages to background non-target tissues such as the liver and kidney.

References

[1] Braak H, Braak E. Neuropathological stageing of Alzheimer-related changes. *Acta Neuropathologica.* 1991;82(4):239-259.

[2] Logan J, Fowler JS, Volkow ND, Wang G-J, Ding Y-S, Alexoff DL. Distribution volume ratios without blood sampling from graphical analysis of PET data. *Journal of Cerebral Blood Flow & Metabolism.* 1996;16(5):834-840.

[3] Zhou Y, Ye W, Brašić JR, Crabb AH, Hilton J, Wong DF. A consistent and efficient graphical analysis method to improve the quantification of reversible tracer binding in radioligand receptor dynamic PET studies. *NeuroImage.* 2009;44(3):661-670.

[4] Ossenkoppele R, Tolboom N, Foster-Dingley JC, *et al*. Longitudinal imaging of Alzheimer pathology using [11C] PIB,[18F] FDDNP and [18F] FDG PET. *Eur J Nucl Med Mol Imaging.* 2012;39(6):990-1000.

[5] Wong K-P, Wardak M, Shao W, *et al*. Quantitative analysis of [18F]FDDNP PET using subcortical white matter as reference region. *Eur J Nucl Med Mol Imaging.* 2010/03/01 2010;37(3):575-588.

[6] Joachim C, Morris J, Selkoe D. Diffuse senile plaques occur commonly in the cerebellum in Alzheimer's disease. *The American journal of pathology.* 1989;135(2):309.

[7] Yamaguchi H, Hirai S, Morimatsu M, Shoji M, Nakazato Y. Diffuse type of senile plaques in the cerebellum of Alzheimer-type dementia demonstrated byβ protein immunostain. *Acta Neuropathologica.* 1989;77(3):314-319.

[8] Jack CR, Lowe VJ, Weigand SD, *et al*. Serial PIB and MRI in normal, mild cognitive impairment and Alzheimer's disease: implications for sequence of pathological events in Alzheimer's disease. *Brain.* 2009;132(5):1355-1365.

[9] Thomas BA, Erlandsson K, Modat M, *et al*. The importance of appropriate partial volume correction for PET quantification in Alzheimer's disease. *Eur J Nucl Med Mol Imaging.* 2011;38(6):1104-1119.

[10] Protas HD, Huang S-C, Kepe V, *et al*. FDDNP binding using MR derived cortical surface maps *NeuroImage.* 2010;49(1):240-248.

[11] Kepe V, Huang S-C, Small GW, Satyamurthy N, Barrio JR. Microstructural Imaging of Neurodegenerative Changes. In: Silverman D, ed. *PET in the Evaluation of Alzheimer's Disease and Related Disorders*. New York: Springer; 2009.

[12] Petersen RC, Parisi JE, Dickson DW, *et al*. Neuropathologic features of amnestic mild cognitive impairment. *Archives of Neurology.* 2006;63(5):665-672.

[13] Small GW, Siddarth P, Burggren AC, *et al*. Influence of cognitive status, age, and APOE-4 genetic risk on brain FDDNP positron-emission tomography imaging in persons without dementia. *Archives of general psychiatry.* 2009;66(1):81.

[14] Rowe CC, Ackerman U, Browne W, *et al*. Imaging of amyloid β in Alzheimer's disease with ^{18}F-BAY94-9172, a novel PET tracer: proof of mechanism. *The Lancet Neurology.* 2008;7(2):129-135.

[15] Choi SR, Golding G, Zhuang Z, *et al*. Preclinical properties of 18F-AV-45: a PET agent for Aβ plaques in the brain. *Journal of Nuclear Medicine.* 2009;50(11):1887-1894.

[16] Engler H, Santillo AF, Wang SX, *et al*. In vivo amyloid imaging with PET in frontotemporal dementia. *Eur J Nucl Med Mol Imaging.* 2008;35(1):100-106.

[17] Varma AR, Snowden JS, Lloyd JJ, Talbot PR, Mann DMA, Neary D. Evaluation of the NINCDS-ADRDA criteria in the differentiation of Alzheimer's disease and frontotemporal dementia. *Journal of Neurology, Neurosurgery & Psychiatry.* 1999;66(2):184-188

[18] Kepe V, Bordelon Y, Boxer A, *et al*. PET Imaging of Neuropathology in Tauopathies: Progressive Supranuclear Palsy. *Journal of Alzheimer's Disease.* 2013;36(1):145-153.

[19] Nelson LD, Siddarth P, Kepe V, *et al*. Positron Emission Tomography of Brain {beta}-Amyloid and Tau Levels in Adults With Down Syndrome. *Archives of Neurology.* 2011;68(6):768.

[20] McKee AC, Cantu RC, Nowinski CJ, *et al*. Chronic traumatic encephalopathy in athletes: progressive tauopathy following repetitive head injury. *Journal of neuropathology and experimental neurology.* 2009;68(7):709.

[21] Small GW, Kepe V, Siddarth P, *et al*. PET scanning of brain tau in retired National Football League players: preliminary findings. *The American Journal of Geriatric Psychiatry.* 2013;21(2):138-144.

[22] Thurber GM, Schmidt MM, Wittrup KD. Factors determining antibody distribution in tumors. *Trends in pharmacological sciences.* 2008;29(2):57-61.

[23] Goodwin DA. Pharmacokinetics and antibodies. *Journal of Nuclear Medicine.* 1987;28(8):1358-1362.

[24] Lepin EJ, Leyton JV, Zhou Y, *et al*. An affinity matured minibody for PET imaging of prostate stem cell antigen (PSCA)-expressing tumors. *Eur J Nucl Med Mol Imaging.* 2010;37(8):1529-1538.

[25] van Dongen GA, Visser GW, Lub-de Hooge MN, De Vries EG, Perk LR. Immuno-PET: a navigator in monoclonal antibody development and applications. *The oncologist.* 2007;12(12):1379-1389.

[26] Deri MA, Zeglis BM, Francesconi LC, Lewis JS. PET imaging with ^{89}Zr: From radiochemistry to the clinic. *Nuclear Medicine and Biology.* 2012.

[27] Knowles SM, Zettlitz KA, Tavaré R, *et al*. Quantitative immunoPET of prostate cancer xenografts with 89Zr-and 124I-labeled anti-PSCA A11 minibody. *Journal of Nuclear Medicine.* 2014;55:452-459.

[28] Bäck T, Jacobsson L. The α-Camera: A Quantitative Digital Autoradiography Technique Using a Charge-Coupled Device for Ex Vivo High-Resolution Bioimaging of α-Particles. *Journal of Nuclear Medicine.* 2010;51(10):1616-1623.

[29] Back, T, Jennbacken, K, Welén, K, *et al*. Experimental evaluation of targeted alpha therapy for treatment of metastatic prostate cancer using A11.1 anti-prostate stem cell antigen minibody labeled with Astatine-211. *Journal of Nuclear Medicine*. 2013; 54 (Supplement 2):117.